

ANALYSIS AND MODELING OF PLASTIC WRINKLING  
IN DEEP DRAWING

A THESIS SUBMITTED TO  
THE GRADUATE SCHOOL OF NATURAL AND APPLIED SCIENCES  
OF  
MIDDLE EAST TECHNICAL UNIVERSITY

BY

SERHAT YALÇIN

IN PARTIAL FULLFILLMENT OF THE REQUIREMENTS  
FOR  
THE DEGREE OF MASTER OF SCIENCE  
IN  
MECHANICAL ENGINEERING

SEPTEMBER 2010

Approval of the thesis:

**ANALYSIS AND MODELING OF PLASTIC WRINKLING  
IN DEEP DRAWING**

submitted by **SERHAT YALÇIN** in partial fulfillment of the requirements for the degree of **Master of Science in Mechanical Engineering Department, Middle East Technical University** by,

Prof. Dr. Canan Özgen  
Dean, Graduate School of **Natural and Applied Sciences**

\_\_\_\_\_

Prof. Dr. Süha Oral  
Head of the Department, **Mechanical Engineering**

\_\_\_\_\_

Prof. Dr. Süha Oral  
Supervisor, **Mechanical Engineering, METU**

\_\_\_\_\_

Prof. Dr. Bilgin Kaftanoğlu  
Co-supervisor, **Mechanical Engineering, METU**

\_\_\_\_\_

**Examining Committee Members:**

Prof. Dr. Haluk Darendeliler  
Mechanical Engineering, METU

\_\_\_\_\_

Prof. Dr. Suha Oral  
Mechanical Engineering, METU

\_\_\_\_\_

Prof. Dr. Bilgin Kaftanoğlu  
Mechanical Engineering, METU

\_\_\_\_\_

Assoc. Prof. Dr. Serkan Dağ  
Mechanical Engineering, METU

\_\_\_\_\_

Prof. Dr. Ali Kalkanlı  
Metallurgical and Materials Engineering, METU

\_\_\_\_\_

**Date:** 16.09.2010

**I hereby declare that all information in this document has been obtained and presented in accordance with academic rules and ethical conduct. I also declare that, as required by these rules and conduct, I have fully cited and referenced all material and results that are not original to this work.**

Name, Last name: Serhat YALÇIN

Signature:

## **ABSTRACT**

### **ANALYSIS AND MODELLING OF PLASTIC WRINKLING IN DEEP DRAWING**

Yalçın, Serhat

M.Sc., Department of Mechanical Engineering

Supervisor: Prof. Dr. Suha Oral

Co-Supervisor: Prof. Dr. Bilgin Kaftanoğlu

September 2010, 116 pages

Deep drawing operations are crucial for metal forming operations and manufacturing. Obtaining a defect free final product with the desired mechanical properties is very important for fulfilling the customer expectations and market competitions. Wrinkling is one of the fatal and most frequent defects that must be prevented. This study focuses on understanding the phenomenon of wrinkling and probable precautions that can be applied. In this study, dynamic – explicit commercial finite element code is used to simulate deep drawing process. The numerical experiments are compared with NUMISHEET benchmarks in order to verify the reliability of the finite element code and analysis parameters.

In order to understand plastic wrinkling, the effect of blank holder force is investigated. Axisymmetrical numerical models of a cup are investigated with different blank holder forces. Wrinkling instability is illustrated in energy diagrams of the process. Effect of anisotropy on wrinkling is also discussed by comparing

isotropic and anisotropic numerical experiments with the material as steel. Different drawbead models, both equivalent and physical, are implied to the problem and results are discussed.

Besides numerical analysis, experimental verification is also conducted as conventional deep drawing operation by a hydraulic press. This yields to the ability to understand the effect of blank thickness on wrinkling formation through numerical and experimental analyses. The wave formations of different sized blanks with four different thicknesses are illustrated.

**Keywords:** Wrinkling, Deep Drawing, Finite Element Method, Sheet Metal Forming, Blank Holder Force, Drawbead, Anisotropy

## ÖZ

### DERİN ÇEKME İŞLEMLERİNDE PLASTİK BURUŞMA ANALİZİ VE MODELLEMESİ

Yalçın, Serhat

Yüksek Lisans, Makina Mühendisliği Bölümü

Tez Yöneticisi: Prof. Dr. Suha Oral

Ortak Tez Yöneticisi: Prof. Dr. Bilgin Kaftanoğlu

Eylül 2010, 116 sayfa

Derin çekme işlemleri metal şekillendirme ve üretimde çok önemlidir. Müşteri Memnuniyeti ve Pazar rekabetini karşılamak amacıyla istenilen mekanik özelliklerde olan kusursuz son ürün elde çok önemlidir. Tehlikeli ve sık görülen kusurlardan biri olan buruşma engellenmelidir. Bu çalışma buruşma fenomenini ve uygulanabilir önlemleri anlamaya odaklanmıştır. Bu çalışmada derin çekme işlemlerini simule edebilmek için dinamik-açık ticari sonlu elemanlar kodu kullanılmıştır. Sayısal deneyler NUMISHEET referansları ile kıyaslanarak sonlu elemanlar kodunun hassasiyeti doğrulanmıştır.

Plastik buruşmayı anlamak için baskı plakası kuvvetinin buruşmaya olan etkisi araştırılmıştır. Değişik baskı plakası kuvvetleri için eksenel simetrik kap

modellemesi incelenmiştir. Buruşma kararsızlığı işlemin enerji grafiklerinde gösterilmiştir. Buruşmadaki anizotropi etkisi çelik malzemelerde, izotropik ve izotropik olmayan nümerik deneyler karşılaştırılarak tartışılmıştır. Pot çemberi modellemesi, eş ve fiziksel olarak, probleme eklenmiş ve sonuçları tartışılmıştır.

Sayısal analizlere ilaveten, hidrolik pres kullanılarak klasik derin çekme işleminin deneysel doğrulama çalışması yapılmıştır. Bu çalışma sayesinde, sayısal ve deneysel analizler ile parça kalınlığının buruşmaya etkisi anlaşılmıştır. Farklı ölçülerdeki parçalarda, dalga oluşumu 4 ayrı kalınlık değeri için gösterilmiştir.

**Anahtar Kelimeler:** Buruşma, Derin Çekme, Sonlu Elemanlar Analizi, Saç Metal Şekillendirme, Baskı Plakası Kuvveti, Pot Çemberi, Anizotropi

*To My Family & Darling*

## ACKNOWLEDGEMENTS

I would like to express my gratefulness and appreciation to my supervisor Prof. Dr. Suha Oral and my co-supervisor Prof. Dr. Bilgin Kaftanođlu for their guidance, encouragement, advice and insight throughout the study.

I wish to thank again Prof. Dr. Bilgin Kaftanođlu for providing me the facilities for my study. I also would like to thank to all employees of the Metal Forming Centre of Excellence in Atılım University and the Metal Forming Lab in METU for their help in performing experiments.

I also want to express my gratitude to Mr. Ahmet Kurt from ASELSAN for his comments and suggestions throughout the study.

I thank to Mr. İ. Erkan Önder for supplying experimental data of NUMISHEET benchmark and his support in the early stages of my work.

I thank to Mr. Servet Gündüz from Yıldırım Alüminyum for his support to my work.

Thanks to my friends Berkay Şanay, Celalettin Yumuş and Cankat Saçlı for their support and friendship. I also wish to thank my colleagues Türker Gürer, Bengi Demirçivi and Yavuz Selim Kayseriliođlu from ASELSAN.

I specially thank to Duygu Şen whose friendship, support, motivation and never ending patience made great contributions to this work.

Finally, I also want to thank my beloved family, my mother Serap Yalçın, my father Nihat Yalçın, my brother Serkan Yalçın for their encouragement and faith in me.

# TABLE OF CONTENTS

ABSTRACT .....	iv
ÖZ .....	vi
ACKNOWLEDGEMENTS .....	ix
TABLE OF CONTENTS .....	x
LIST OF FIGURES .....	xii
LIST OF TABLES .....	xvi
CHAPTERS	
1. INTRODUCTION .....	1
2. SURVEY OF LITERATURE .....	6
2.1 Introduction .....	6
2.2 Deep Drawing Process .....	6
2.2.1 Stress Zones during Deep Drawing .....	8
2.3 Other Deep Drawing Technologies .....	11
2.4 Anisotropy .....	14
2.5 The Limiting Drawing Ratio .....	15
2.6 Formability of Sheet Metals .....	18
2.6.1 Forming Limit Diagrams .....	21
2.7 Previous Studies .....	23
3. OBJECT OF THE PRESENT STUDY .....	28
4. THEORY OF FINITE ELEMENT METHOD .....	30
4.1 Introduction .....	30
4.2 History of Finite Element Method .....	30
4.3 Basics of Finite Element Method .....	31
4.3.1 Finite Element Procedures .....	33
4.3.2 Element Stiffness Matrix .....	34
4.3.3 Shape Function .....	35

4.3.4 Transformation Matrix .....	36
4.4 Algorithms of Numerical Simulation Solvers.....	38
4.4.1 Differences between Implicit and Explicit Approaches.....	38
4.4.2 Dynamic- Explicit Finite Element Method.....	40
4.4.3 Plastic Work.....	46
4.5 Features of PAM-STAMP 2G.....	47
5. NUMERICAL AND EXPERIMENTAL RESULTS .....	50
5.1 Introduction.....	50
5.2 Benchmark Problem.....	51
5.2.1 Process Parameters.....	53
5.2.2 Punch Velocity.....	54
5.2.3 Element Size and Refinement.....	59
5.2.4 Mesh Topology.....	64
5.2.5 Comparison with NUMISHEET 2002 Benchmarks.....	67
5.3 Wrinkling Simulations .....	70
5.3.1 Blank Holder Simulations.....	70
5.3.2 Drawbead Simulations.....	79
5.4 Experimental Study.....	94
5.4.1 Tension Test.....	94
5.4.2 Conventional Deep Drawing Experiment.....	96
6. DISCUSSION .....	102
7. CONCLUSION.....	107
REFERENCES.....	107
APPENDICES	
A. NUMISHEET 2002 BENCHMARK PARTICIPANTS.....	107
B. TINIUS OLSEN TESTING MACHINE.....	112

# LIST OF FIGURES

## FIGURES

Figure 1.1 Automobile parts produced by deep drawing.....	2
Figure 1.2 Conventional Deep Drawing Process .....	2
Figure 1.3 Basic Tools in Deep Drawing.....	3
Figure 1.4 Deep Drawn Parts .....	3
Figure 1.5 Various failure modes in Deep Drawing: 1-Flange wrinkling; 2-Wall wrinkling; 3-Part wrinkling; 4-Ring prints; 5-Traces; 6-Orange skin; 7-Lüder's strips; 8-Bottom fracture; 9-Corner fracture; 10,11,12-Folding; 13,14-Corner folding .....	4
Figure 2.1 Geometry parameters for deep drawing tools.....	7
Figure 2.2 Four different zones in deep drawing .....	9
Figure 2.3 Pressing forces in deep drawing of a round cup with a blank holder .....	9
Figure 2.4 Principle of High Pressure Sheet Forming: .....	
a) Beginning of process, b) end of free bulging, c) end of cavity filling.....	13
Figure 2.5 Principle of hydromechanical deep drawing .....	14
Figure 2.6 Effect of average strain ratio on LDR for different materials .....	17
Figure 2.7 Effect of relative punch diameter on the limiting drawing ratio .....	17
Figure 2.8 Bursting, wrinkling and tearing observed in analysis.....	18
Figure 2.9 Formability of sheet metals .....	19
Figure 2.10 Working window in deep drawing .....	20
Figure 2.11 Methods used for evaluating the sheet metal formability.....	21
Figure 2.12 Grid of small circles are printed or etched on sheet metal .....	22
Figure 2.13 FLD Experiment .....	23
Figure 4.1 Finite Element Mesh structure.....	31
Figure 4.2 Input parameters of Finite Element Method.....	33
Figure 4.3 Elasto-Plastic and Rigid-Plastic material behaviors .....	34
Figure 4.4 General Element .....	34

Figure 4.5 Simple two node element .....	35
Figure 4.6 Local and Global Coordinate system of an element.....	36
Figure 4.7 Simple one dimensional mass-spring-damper system.....	40
Figure 4.8 PAM-STAMP 2G Modules .....	48
Figure 5.1 Tool geometry of Benchmark problem .....	51
Figure 5.2 True Stress vs. True Strain curve of DDQ mild steel.....	52
Figure 5.3 Mesh structures of Half and Full model .....	54
Figure 5.4 Punch speed effect on thickness distribution of a 5mm Element Size .....	55
Figure 5.5 Punch speed effect on thickness distribution of a 3mm Element Size .....	56
Figure 5.6 Punch Force vs. Punch Progression curves for different Punch Velocities .....	57
Figure 5.7 Punch Force vs. Punch Progression curves for unacceptable Punch Velocities.....	57
Figure 5.8 Punch Speed effect on Computational Time for 5mm mesh size.....	58
Figure 5.9 Fillet mesh detail of the Die .....	59
Figure 5.10 Refinement procedures .....	60
Figure 5.11 Angle Criteria .....	61
Figure 5.12 Geometrical Criterion.....	61
Figure 5.13 Thickness variations of 3mm, 5mm, 5mm/2Ref, 5mm/3Ref for Punch Speed 500mm/s. ....	62
Figure 5.14 Punch Force vs. Punch Progression curves for different element sizes .	63
Figure 5.15 Punch Speed and Element size effect on Computational Time.....	63
Figure 5.16 Uniform and Radial Mesh of the blank .....	64
Figure 5.17 Equivalent plastic strain contours of radial and uniform mesh structures .....	65
Figure 5.18 Punch Force vs. Punch Progression curves for Radial and Uniform mesh structures .....	66
Figure 5.19 Wrinkled blank with uniform and radial mesh structures .....	66
Figure 5.20 Comparison of Punch Force – Punch Stroke curve of steel HBHF simulation with Benchmark Experiments .....	68
Figure 5.21 Comparison of outer circumference of steel flanges of simulation.....	69

Figure 5.22 Comparison of outer circumference of steel flanges of simulation.....	69
Figure 5.23 Deep drawn blank without Blank holder .....	71
Figure 5.24 Deep drawn parts with different blank holder forces and corresponding wave formations .....	71
Figure 5.25 Wave Formations for 1 mm, 5 mm, 10 mm, 15 mm and 20 mm Punch Depths with simulations of 1 N , 1000 N and 3000N Blank Holder Forces.....	73
Figure 5.26 Further analysis images for finding required blankholder force. ....	75
Figure 5.27 Energy Graphs for 5000 N Blank Holder Force.....	76
Figure 5.28 External Energy Graphs versus Punch Progression for 1000 N, 5000 N and 10000 N Blank Holder Forces.....	77
Figure 5.29 Anisotropic and Isotropic Material wave formations .....	78
Figure 5.30 Drawbead models of Pam Stamp.....	80
Figure 5.31 Restraining and Opening Force of the Equivalent Drawbead model ....	81
Figure 5.32 Drawbead model in reality and in simulation.....	81
Figure 5.33 Thickness distributions for different groove depths at 20 mm punch depth.....	82
Figure 5.34 Drawbead models for 70 mm, 80 mm and 90 mm .....	83
Figure 5.35 Thickness contours for 70 mm, 80 mm and 90 mm radii drawbeads.....	83
Figure 5.36 Fully drawn part with 90 mm drawbead.....	84
Figure 5.37 Wrinkled blank due to insufficient blank holder force.....	85
Figure 5.39 Drawbead added simulation models.....	86
Figure 5.40 Small drawbead analyses for 10 kN BHF.....	87
Figure 5.41 Large drawbead analyses for 10 kN BHF.....	88
Figure 5.42 Small drawbead analyses for 100 kN BHF.....	89
Figure 5.43 Large drawbead analyses for 100 kN BHF.....	90
Figure 5.44 Inclined drawbead dimensions .....	91
Figure 5.45 Thickness contours for inclined drawbead model with 100 kN BHF ....	92
Figure 5.46 Mesh structure before and after the simulation .....	93
Figure 5.47 External energy diagrams for different drawbead models.....	94
Figure 5.48 Universal Tensile Testing Machine with 30 ton force capacity (Zwick)	95
Figure 5.49 Tension Test specimens, 2 mm thickness, before and after the test.....	96

Figure 5.50 Tinius Olsen Tesing Machine .....	97
Figure 5.51 Deep Drawn parts with different thickness and different diameters .....	98
Figure 5.52 Wrinkling formations for 80 mm blanks .....	98
Figure 5.53 Wrinkling formations for 100 mm blanks .....	99
Figure 5.54 Finite Element Model of the experiment tools .....	100
Figure 5.55 Experimented and Simulated deep drawn part .....	100
Figure 5.56 Wrinkling formations for 80 mm diameter blanks .....	100
Figure 5.57 Wrinkling formations for 90 mm diameter blanks .....	101
Figure 5.58 Wrinkling formations for 100 mm diameter blanks .....	101

## LIST OF TABLES

### TABLES

Table 4.1 Main Differences in Explicit and Implicit Approaches .....	39
Table 5.1 Material properties of DDQ mild steel .....	52
Table 5.2 Number and Amplitude of Waves for increasing Blank Holder Forces for 20 mm Draw Depth .....	72
Table 5.3 Number and Amplitude of Waves for increasing Blank Holder Forces for 40 mm Draw Depth .....	74
Table 5.4 Number and Amplitude of Waves for finding the required Blank Holder Force for 40 mm Draw Depth .....	74
Table 5.5 Number of Waves for Anisotropic and Isotropic Materials.....	79
Table 5.6 Drawbead geometry parameters.....	81
Table 5.7 Drawbead Dimensions in millimeters.....	86
Table 5.8 Material Properties of AL 1050 Material for four thickness values .....	96
Table 5.9 Experiment and Simulation results for specified blank diameters for different thicknesses.....	101
Table A.1 Participant information of AE-01.....	113
Table A.2 Participant information of AE-02.....	113
Table A.3 Participant information of AE-03.....	113
Table A.4 Participant information of AE-04.....	114
Table A.5 Participant information of AE-05.....	114
Table A.6 Participant information of AE-06.....	114
Table A.7 Participant information of AE-07.....	115
Table B.1 Specifications of Tinius Olsen A-40 Testing Machine .....	116

# CHAPTER 1

## INTRODUCTION

Casting, machining, welding and metal forming are the main methods of manufacturing [1]. The other methods of manufacturing are powder metallurgy, heat treatment and finishing. In casting a liquid material is poured into a mold and then allowed to solidify in order to take the desired shape. By casting, big and complex parts can be manufactured. The second manufacturing process is machining. This process can be defined as removing material (chips) from the workpiece. Machining is one of the most used processes in manufacturing. Cutting tool is used for removing material from the piece while cooling fluid dissipates the heat generated from the process. Another method is welding. In this method, two or more metal pieces are joined together by melting or fusing them with the help of heat. Welding is generally used in ship building, automotive manufacturing and aerospace applications. The last method is metal forming. In this process the material shape is formed by applying force to the piece. Metal forming is used for achieving complex shape products and improving the strength of the material. During forming, little material is wasted compare to other manufacturing processes. Bulk forming and sheet metal working are the two main groups of forming processes based on raw material used in the process. Rolling, forging and extrusion in bulk forming can be done cold, warm and hot. The other forming process is sheet metal forming. In this method, thin sheets of metal are shaped by applying pressure through dies. Sheet metal forming is very important for metals because nearly %50 of metals is produced in sheet metals. [2]

Sheet metal forming is done by many ways such as shearing and blanking, bending stretching, spinning and deep drawing. Those methods are widely used for producing various products in different places of industry. The parts manufactured by sheet metal forming are widely used in automotive and aircraft industries.

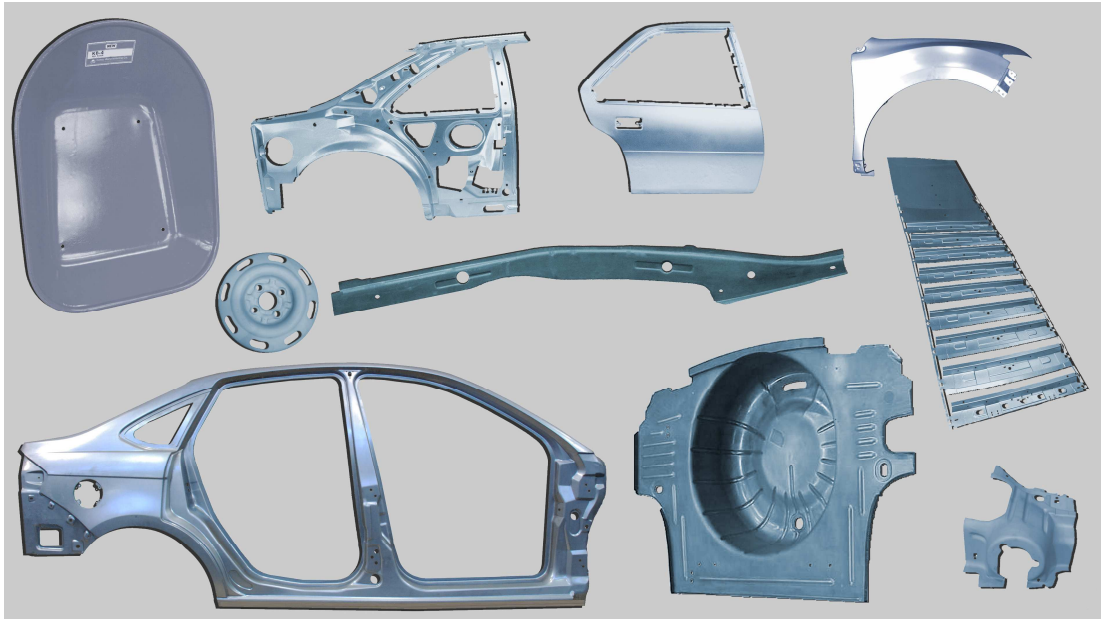


**Figure 1.1 Automobile parts produced by deep drawing**

Deep drawing is one of the most important sheet metal forming processes. A 2-d part is shaped into a 3-d part by deep drawing. According to the definition in DIN 8584, “deep drawing is the tensile-compressive forming of a sheet blank to a hollow body open on one side or the forming of a pre-drawn hollow shape into another with a smaller cross-section without an intentional change in the sheet thickness.”

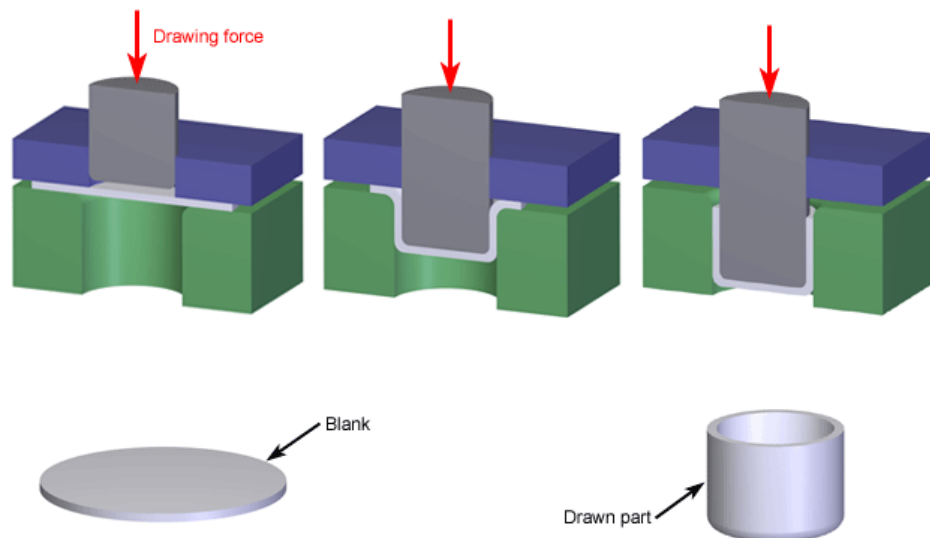


**Figure 1.2 Conventional Deep Drawing Process [3]**

In the deep drawing process, flat sheet of metal (called blank) is placed over the die, and with the help of the punch, blank is pressed into the die cavity. Blankholder applies pressure to the blank in the flange region during the deep drawing process. The basic tools of the process are shown in Figure 1.3.

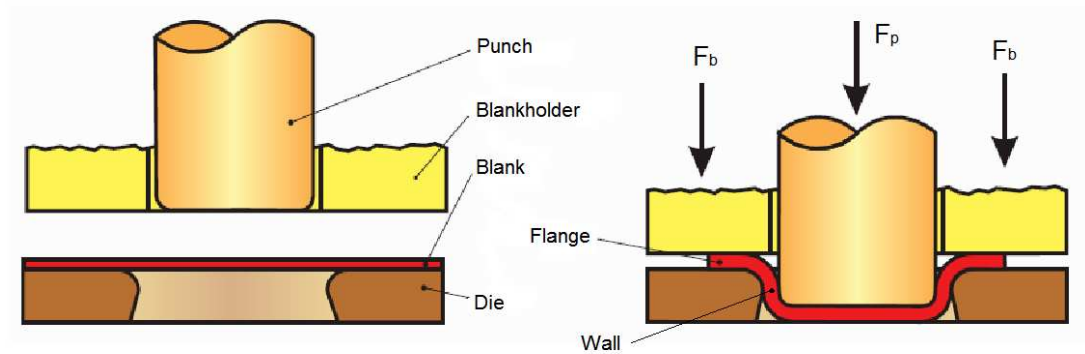


**Figure 1.3 Basic Tools in Deep Drawing [4]**

Deep Drawing is widely used in industry for producing automobile and aircraft body parts, household applications and auxiliary parts in construction field [5]. The method is very suitable for producing large amount of simple shaped parts, like cups, cans, vessels, etc... Deep drawn parts are shown in the Figure 1.4.



**Figure 1.4 Deep Drawn Parts**

Deep drawing is affected by many factors, like material properties, tool selection, lubrication etc... Because of these factors, some failures may occur during the process.

Tearing, necking, wrinkling, earing and poor surface appearance are the main failure types that can be seen in deep drawing, see the Figure 1.5. Tearing and necking are tensile instability caused by strain localization. The strength of the part is reduced and the appearance worsened because of tearing and necking. Another failure is wrinkling, caused by compressive stresses unlike to tearing and necking. Plastic buckling occurs because of the high compressive stress and waves formed on the part. The other one is earing. On the walls of the totally drawn part earing can be seen. The main reason for earing is planar plastic anisotropy. Also the last defect types which poorly affect the appearance of the sheet metal part are ring prints, traces, orange skin (or orange peel structure), and Lüders strips.

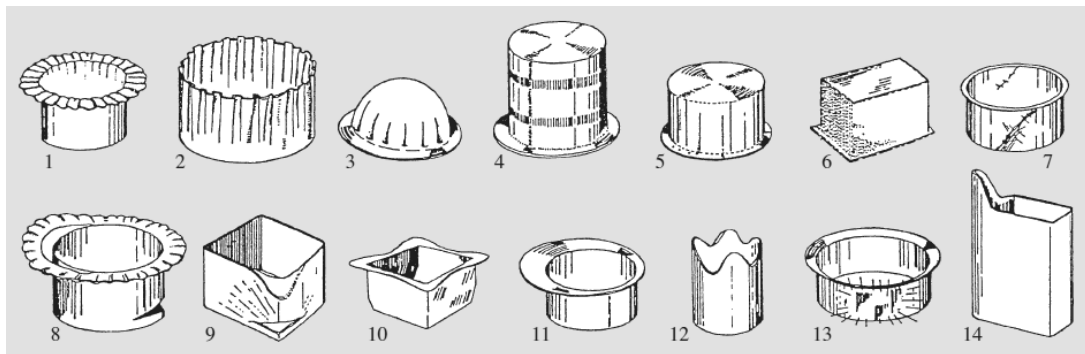


**Figure 1.5 Various failure modes in Deep Drawing: 1-Flange wrinkling; 2-Wall wrinkling; 3-Part wrinkling; 4-Ring prints; 5-Traces; 6-Orange skin; 7-Lüder's strips; 8-Bottom fracture; 9-Corner fracture; 10,11,12-Folding; 13,14-Corner folding. [2]**

A part wrinkled during the deep drawing process, will not be accepted and most likely become a scrap, a total waste of both money and time. Because of these reasons, wrinkling must be prevented. There are two main methods used in order to prevent wrinkling. The former is using a blankholder. Blankholder is a tool used for preventing the edge of a sheet metal part from wrinkling. There are two main blankholder types available namely, clearance and pressure type blankholder. In the former, the sheet metal kept at a constant thickness by adjusting fixed distance between blankholder and die, during the process and wrinkling is prevented. In the latter, force is applied to the blank from the blankholder, called blank holder force (BHF), in order to prevent wrinkling. Adjusting the BHF is very important, because

high BHF leads to fracture at the cup wall and low BHF leads to wrinkling in the flange of the cup.

The other method is using drawbead in the flange region. Drawbeads are placed to the die (small protrusions on the die surface) in order to control the flow of the material during the forming operations. The material fills the groove, this results in a change in the strain distribution in the flange region. Thinning of the blank is achieved and compressive stresses are decreased so wrinkling is avoided.

In manufacturing processes the main goal is to obtain defect free end product. The first step of manufacturing is the designing process, which enormously affects the whole manufacturing process. The designer must have knowledge about possible problems and their solutions during production. Many researches have been completed in various manufacturing processes because of the knowledge needed to achieve better quality product. This thesis will discuss about flange wrinkling problem and its prevention in the deep drawing process.

The whole thesis composed of seven chapters. The first chapter is about the general information about the study. In the next chapter, the literature survey about deep drawing process, wrinkling problem and previous work on deep drawing will be discussed. Third chapter defines the object of the study. The fourth chapter is dedicated to the Finite Element Method and PAM-STAMP, commercial Finite Element program. In the next chapter, numerical and experimental data obtained throughout the study will be given. The discussion of these results will be discussed in chapter six. Finally, conclusions of this study will be presented in the last chapter.

## **CHAPTER 2**

### **SURVEY OF LITERATURE**

#### **2.1 Introduction**

This chapter presents the literature search related to the current study. First, conventional deep drawing process will be discussed. Secondly, sheet metal formability concept is mentioned and possible failure modes are discussed. Then, wrinkling and its prevention are stated. At the end of the chapter, previous researches related to the mentioned concepts are presented.

#### **2.2 Deep Drawing Process**

As mentioned in the introduction chapter, flat sheet of metal is formed into a 3-d product by deep drawing process. The main tools of the process are blank, punch, die and blankholder. In the simple circular cup drawing process with blankholder, the tools and tool geometries are shown in the Figure 2.1.

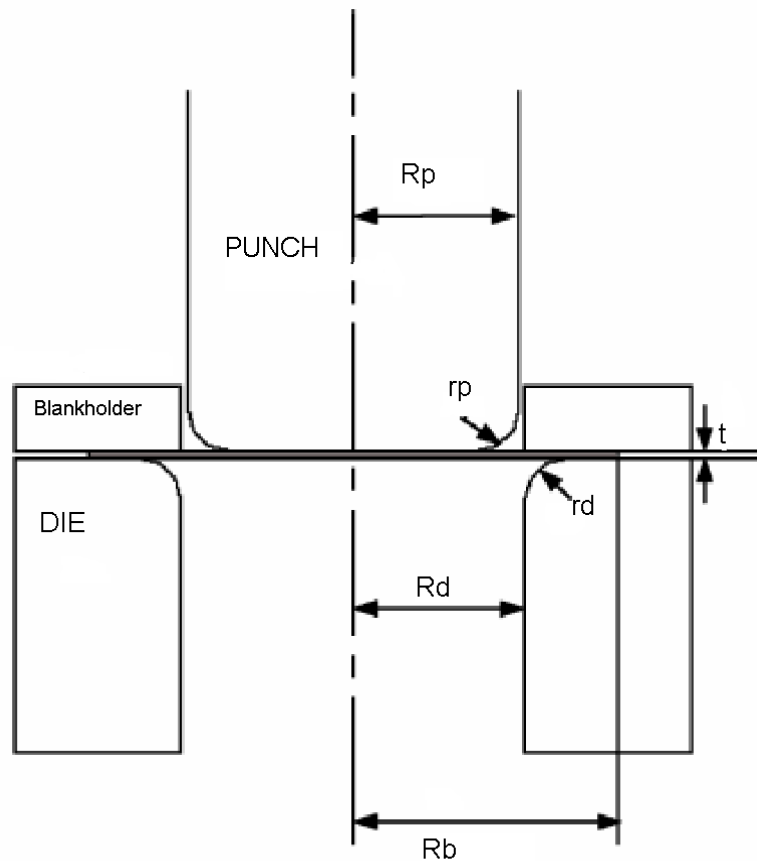


**Figure 2.1 Geometry parameters for deep drawing tools**

The tool geometry parameters are stated as;

- Punch Radius  $R_p$
- Punch Edge Radius  $r_p$
- Blank Thickness  $t$
- Blank Radius  $R_b$
- Die Radius  $R_d$
- Die Edge Radius  $r_d$

These parameters must be selected very carefully because the final product highly depends on these geometries. Shape of the fully drawn cup is obtained by selecting die and punch respectively. Clearance is also an important parameter, formulated as the difference between die radius and punch radius ( $c = R_d - R_p$ ). If the clearance is not large enough, ironing will occur. Ironing is defined as thinning

of the blank at the die cavity. In order to eliminate this problem, clearance should be %25 larger than the initial blank thickness. Also the punch edge radius and die edge radius effects the process. Larger corner radius lowers the punch load whereas smaller radius increases the needed punch load.

In addition to the tool geometry parameters, there are also physical parameters in drawing operations. Some of these are classified as;

- Blank material properties
- Blank holder force
- Punch speed
- Lubrication
- Draw depth

### ***2.2.1 Stress Zones during Deep Drawing***

Deep drawing process is defined as a tensile-compressive forming of the sheet metal in the literature. During the deep drawing process, due to punch force and blankholder force, different stress zones are formed. Four different states can be defined as Force application zone, Force transmission zone, Bending zone and Forming zone, that can be seen from the Figure 2.2.

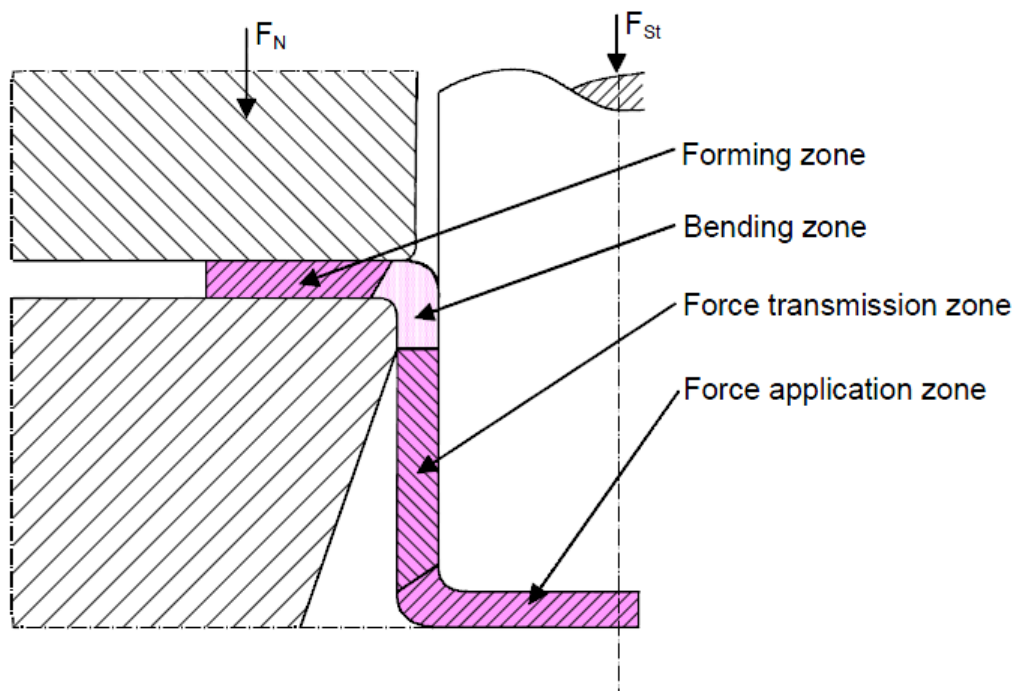


**Figure 2.2 Four different zones in deep drawing [6]**

The punch force is applied onto the bottom of the drawn part, which is called the force application zone. Then it is transferred to the flange region. The force is transmitted along the wall of the cup. Bending happens over the die edge radius and forming takes place in the flange region.

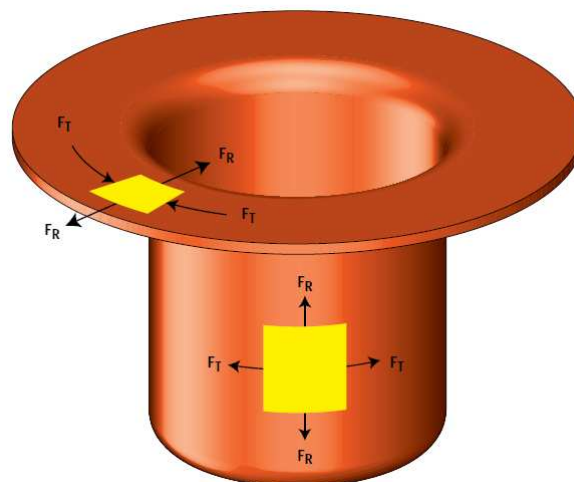


**Figure 2.3 Pressing forces in deep drawing of a round cup with a blank holder**

[4]

The workpiece is subjected to radial tension forces  $F_R$  and tangential compression forces  $F_T$  during the process (Figure 2.3). The material is compressed in the tangential direction and stretched in the radial direction. As it can be seen from the figure above, there are compressive forces in the flange region and tensile forces elsewhere in the workpiece. [4]

Over the punch head, force application zone, sliding and stretching of the material occurs. In this region, material gets thinner because of stretching. The limiting drawing ratio (LDR), will be discussed later, depends on the load carrying capacity of this zone. The maximum load carrying capacity is determined by the plastic instability taking place in this region. However, plastic instability depends on the friction properties between the punch and blank. Equ-biaxial tensile stresses act in this region.

In the region between die and punch, force transmission zone, generally there is no contact of the material with either of punch and die. This is a transition region between die and punch. In this region radial tensile stresses act on the material. Material gets thinner and tearing or necking can take place in this region.

Over the die edge radius, sliding and bending of the material occurs. In this region, in the radial direction tensile stresses occurs, whereas compressive stress is observed in the circumferential direction. As mentioned before, radius of the curvature of die profile has effect on the punch load. For a sharper radius, more plastic bending work is done, therefore the punch load increases. In the bending region, material gets thinner due to bending under tensile stresses in the radial direction.

In the flange region pure radial drawing occurs. There is a circumferential compressive stress and a radial tensile stress state in this region. This is the only region that the material gets thicker because of the compressive stress. There is a possibility of bulging in the flange region due to compressive forces. When the compressive forces at the flange region exceed a certain limit, wrinkling occurs.

Therefore, the blank holding forces, and sometimes the drawbeads, are utilized to control the flowing of the material into the die cavity to overcome compressive forces' effects.

As the draw depth is increased, the amount of deformation and the deformation resistance are also increased. The sheet metal is most severely stretched in the corner of the draw punch, corresponding to the tip of the drawn cup. Failure normally occurs at this region of the blank.

Since there is a strongly non-homogeneous deformation throughout the part, residual stresses arise. Residual tension is observed on the outside whereas residual compression occurs in the inside of the part over the die lip in axial direction. These residual stresses are caused by bending and unbending action happened over the die. Through the wall of the drawn part, residual stresses takes its largest value near the top of the wall, near the intersection area of wall and die lip, due to bending. The wall of the part is subjected to bending moment because of residual stresses. This moment is leveled by the hoop tension, occurring at the top of the cup. Hoop tension can cause stress corrosion cracking at the transmission zone (wall) in some metal materials.

Owing to the presence of residual stresses, deep drawn parts are sensitive to successive operations. A workpiece may distort or fracture upon machining operations and heat treatments may cause the part to change shape.

### **2.3 Other Deep Drawing Technologies**

There are alternative deep drawing methods which make use of active media and active energy. Active media include formless solid substances such as sand or steel balls, fluids (oil, water) and gases, whereby the forming work is performed by a press using a method similar to that employed with the rigid tools. Hydroforming is the general name for this soft-tool forming technology. Rubber pad forming and fluid

tool forming are types of soft tool forming technologies. For instance, in Geurin and Marform processes the die is replaced with a rubber path and the punch is solid.

In hydroforming, die or punch is replaced by oil, water or other fluid media. In other words the rigid tool force is replaced by the fluid pressure. The main groups of hydroforming are Tube hydroforming and Sheet hydroforming. Tube hydroforming is a cold forming process. During the process, a tube is subjected to pressure from the inside and at the same time it is compressed in axial or radial direction. Just like deep drawing processes, during tube drawing process some instability phenomena may occur. Bursting, buckling and wrinkling can be observed throughout the tube hydroforming. [2]

Sheet hydroforming is divided into two types; called high-pressure sheet forming and hydromechanical deep drawing. In high pressure sheet forming, pressurized fluid is used for the replacement of the punch. The process is composed of two stages, called free bulging and cavity filling stage, shown in the Figure 2.4. Lower springback and lower residual stress values are the main advantages of the process.

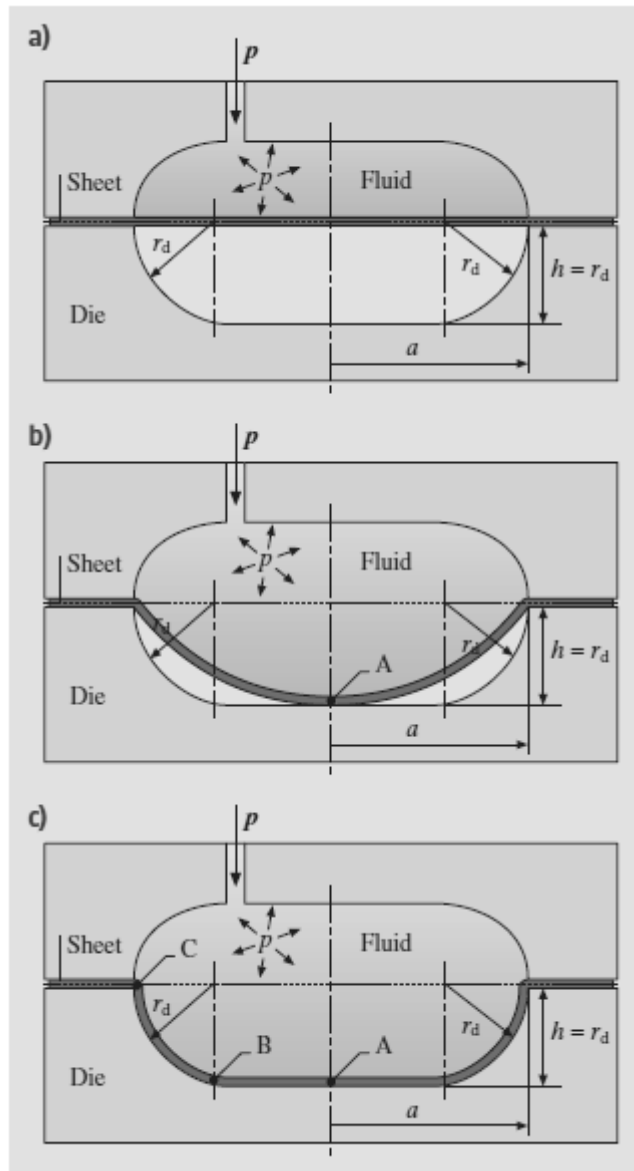


**Figure 2.4 Principle of High Pressure Sheet Forming:**  
**a) Beginning of process, b) end of free bulging, c) end of cavity filling**

However, in hydromechanical deep drawing, die is replaced by a pressurized fluid. The main stages of the process are shown in the Figure 2.5. The main advantages of the process are obtaining higher drawing ratio, better surface quality and lower springback of the product.

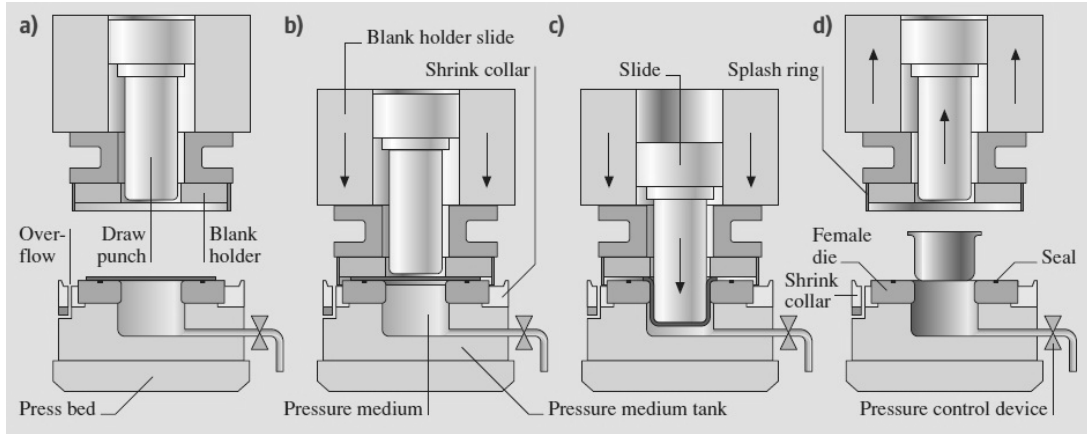


**Figure 2.5 Principle of hydromechanical deep drawing**

Hydroforming is a commonly used technique in the industry. Over recent years, the process gained popularity on three main groups: The automotive industry (cross members, side members, manifolds, roof rails, spoilers, gear shafts, seat frame components...), domestic appliance industry (tube bends, T-fittings...) and pipe component manufacturers (intake pipes...).

## 2.4 Anisotropy

Due to their crystallographic structure and the characteristic of the rolling process, sheet metals generally exhibit a significant anisotropy of mechanical properties. The variation of their plastic behavior with direction is assessed by a quantity called Lankford parameter or anisotropy coefficient. This coefficient is usually obtained by uniaxial tensile tests on strip shaped sheet specimens. The anisotropy coefficient ( $r$ ) is defined by

$$r = \frac{\varepsilon_2}{\varepsilon_3} \quad (2.1)$$

Where  $\varepsilon_2$  is the strain in the width direction and  $\varepsilon_3$  is in the thickness direction.

Experiments show that “ $r$ ” depends on the in-plane direction. If the tensile specimen is cut having its longitudinal axis parallel to the rolling direction, the coefficient  $r_{90}$  is obtained. The average of the  $r$ -values obtained for different

directions in the plane of the sheet metal represents the coefficient of normal anisotropy  $r_n$ . The coefficient of normal anisotropy is obtained from equation

$$r_n = \frac{r_0 + 2 \cdot r_{45} + r_{90}}{4} \quad (2.2)$$

where

$r_0$  is anisotropy factor in rolling direction

$r_{45}$  is anisotropy factor in  $45^\circ$  direction relative to rolling direction

$r_{90}$  is anisotropy factor in  $90^\circ$  direction relative to rolling direction

A material with a high  $r_n$  value will experience less thinning during a deep drawing operation than a material having a smaller  $r_n$  value, provided that their flow characteristics are identical. For instance, aluminum usually has an  $r$  value smaller than 1 (about 0.6), whereas steel has an  $r_n$  value larger than 1 (about 1.5).

A measure of the variation of normal anisotropy with the angle to the rolling direction is known as planar anisotropy. The equation for planar anisotropy is given as;

$$\Delta r = \frac{r_0 - 2 \cdot r_{45} + r_{90}}{4} \quad (2.3)$$

This value can be negative or positive. For instance, steels usually have positive  $\Delta r$ . As stated before, planar anisotropy is directly related to earing. As the magnitude of the  $\Delta r$  value increases, the ear heights increase. Therefore for deep drawing operations, suitable materials must have smaller planar anisotropy values in magnitude.

## 2.5 The Limiting Drawing Ratio

The limiting draw ratio is the ratio of the diameter of the initial blank form to the diameter of the drawn part. LDR is an important numerical value for cylindrical draw parts in determining the required number of drawing steps. For cylindrical cup

drawing process with circular cross-section, drawing ratio can be defined by the following equation:

$$LDR = \frac{d_{0,MAX}}{d_p} \quad (2.4)$$

Here,  $d_{0, MAX}$  is the maximum blank diameter that can be fully drawn to a cup without any failure and  $d_p$  is the punch diameter.

The drawing ratio is dependent on many factors like the tool geometry, lubrication conditions, and the amount of blank holding forces, sheet thickness, and material properties (especially the  $r$  and  $n$  value). The limiting drawing ratio (LDR), which can be reached in a single drawing step, is theoretically calculated by membrane analysis. The ideal limiting drawing ratio found from the membrane theory is

$$LDR_{MAX} \leq e \approx 2.72 \quad (2.5)$$

In reality the LDR for aluminum sheets are 1.8 to 2.0. This value is around 1.9 to 2.2 for steel sheets. The reason for this is various process parameters are not considered in the simplifying membrane theory.

For any material in a deep drawing operation, a higher LDR means that ‘deeper’ drawings are possible, whereas a lower LDR restricts the deep drawability. The LDR is strongly material dependent and for several materials the effect of average strain ratio on LDR can be seen from the Figure 2.6

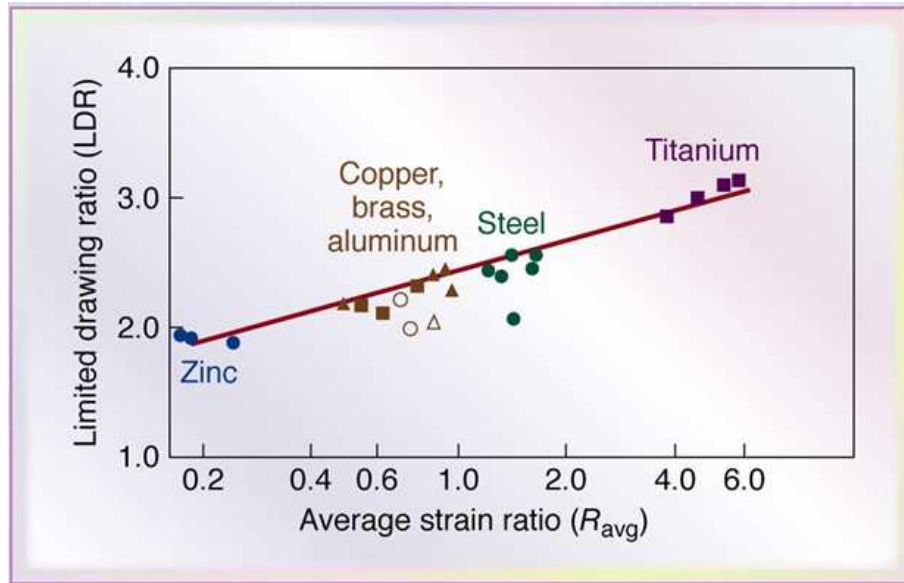


Figure 2.6 Effect of average strain ratio on LDR for different materials [7]

Also the blank thickness and the punch diameter affect the LDR. Limiting drawing ratio decreases as the relative punch diameter increases, see the Figure 2.7

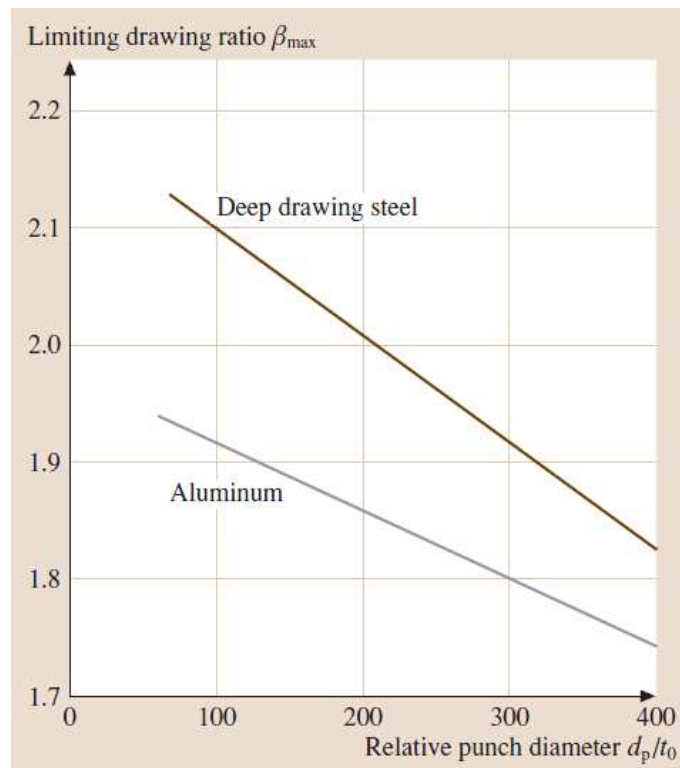
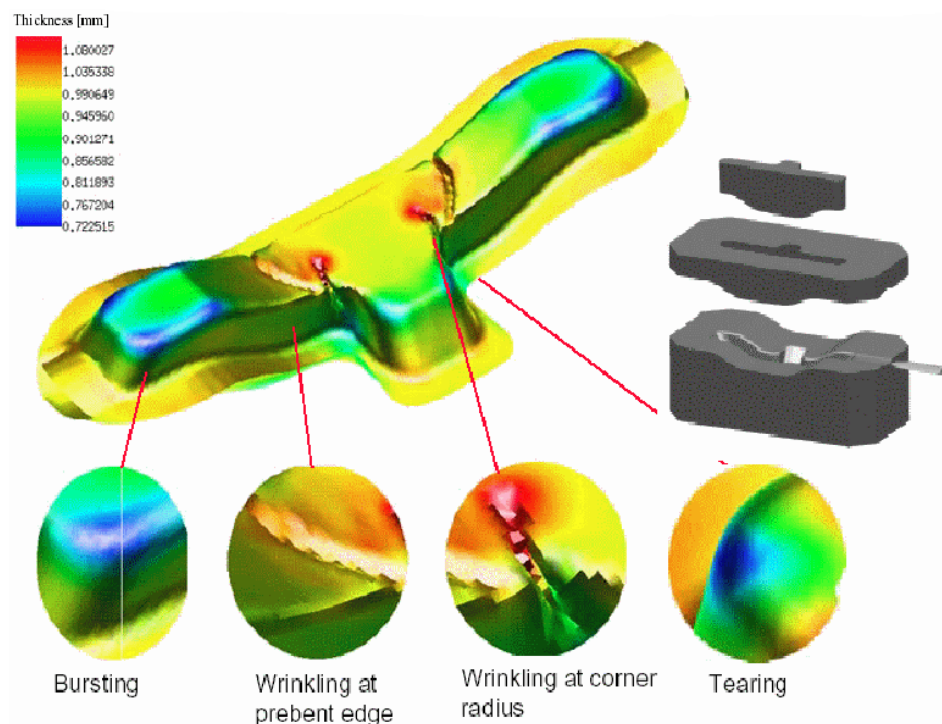


Figure 2.7 Effect of relative punch diameter on the limiting drawing ratio [2]

When the friction between the blank and the punch is low, then failures will occur in the base of the part. If the friction between the part and the punch is high, the base of the drawn part will be increasingly stressed with increasing friction in the can body so that the failure zone will be moved to the body of the drawn can. In order to ensure a safe production process, it is preferable to select a draw ratio that is rather modest and less than the maximum possible value.

## 2.6 Formability of Sheet Metals

At the end of the nineteenth century, due to the development of the sheet forming technology, sheet metal formability became a research topic. Some of the first researchers interested in this field were Bessemer and Parkers, Adamson, Considere and Erichsen [8]. Necking, tearing, wrinkling, bursting, or poor qualities in appearance are the factors that generally define a limit to the deformation in sheet metal forming (Figure 2.8).



**Figure 2.8 Bursting, wrinkling and tearing observed in analysis**

The formability of sheet metals is affected by many parameters, like material parameters, process parameters and strain bounding criteria. Figure 2.9 summarizes the parameters that have an effect on the formability of sheet metals.

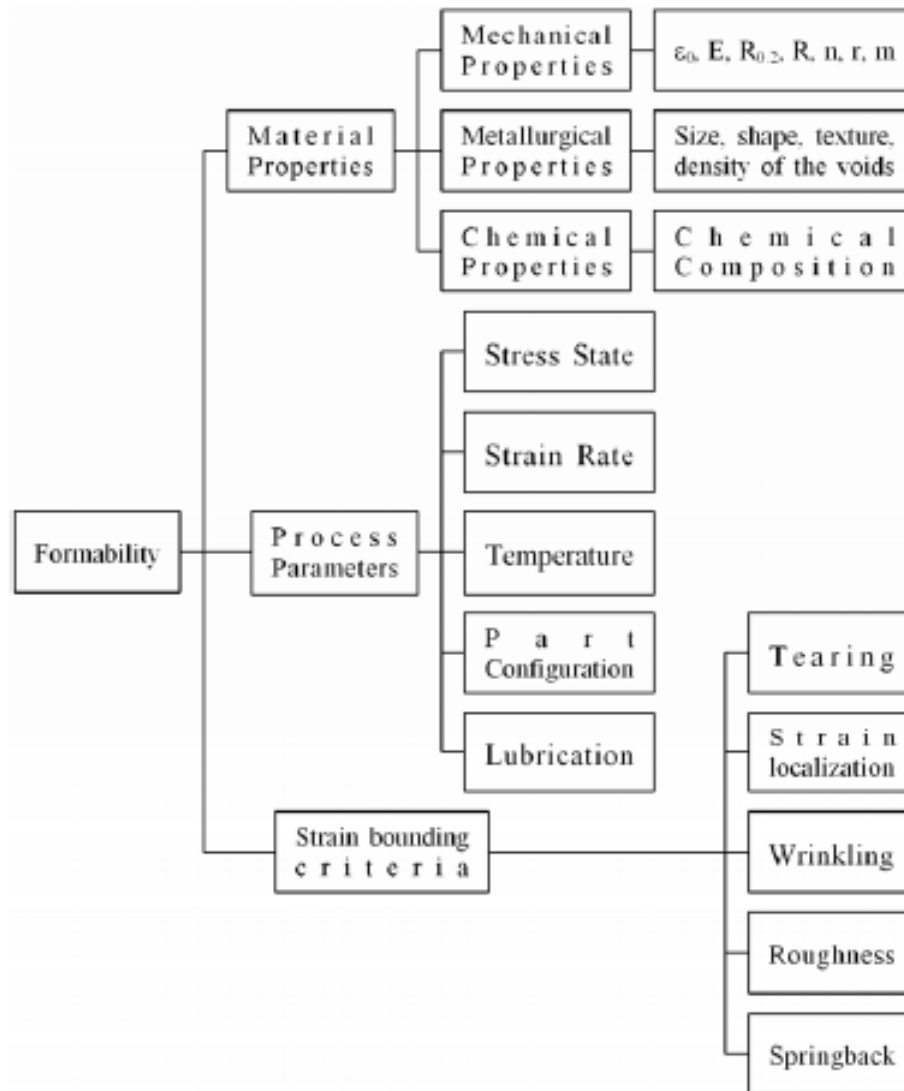


**Figure 2.9 Formability of sheet metals [8]**

The affect of blank holder force and drawing ratio on formability in deep drawing is presented in Figure 2.10.

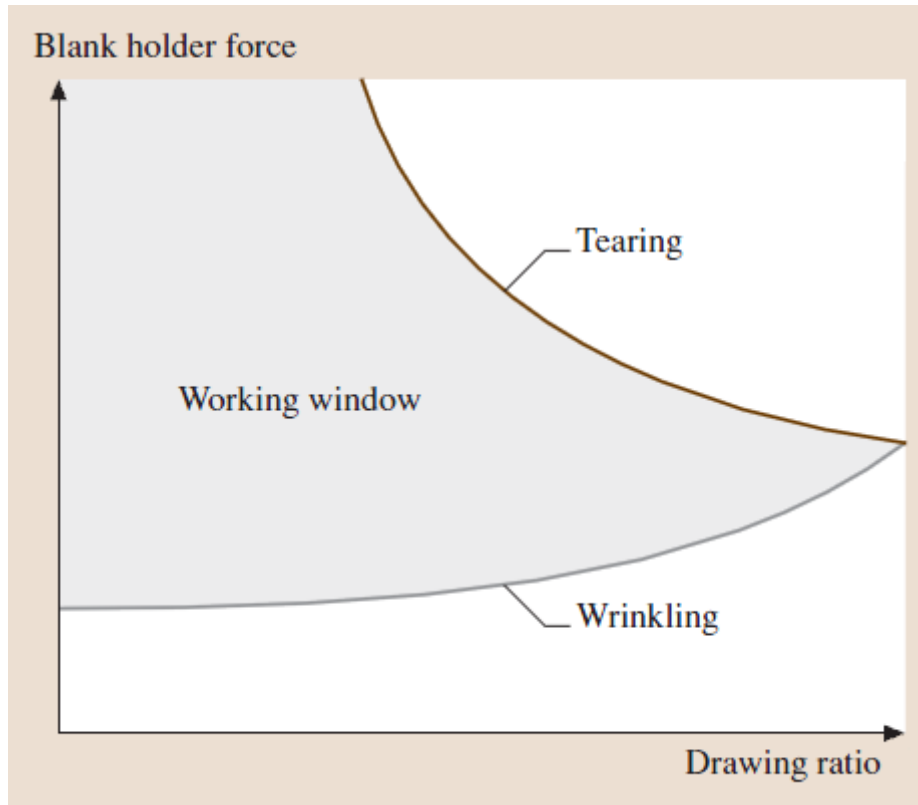


**Figure 2.10 Working window in deep drawing [2]**

As can be derived from Figure 2.10, the value of blank holder force is very important as with the fixed drawing ratio value, low BHF results in wrinkling and high BHF results in tearing. Also another important point is: working window is narrowed as drawing ratio increases.

There are methods developed for evaluating the formability of sheet metals. Sheet metal formability is measured by simulating tests, mechanical tests, finding limiting dome height and drawing forming limit diagrams. These methods can be seen from Figure 2.11.

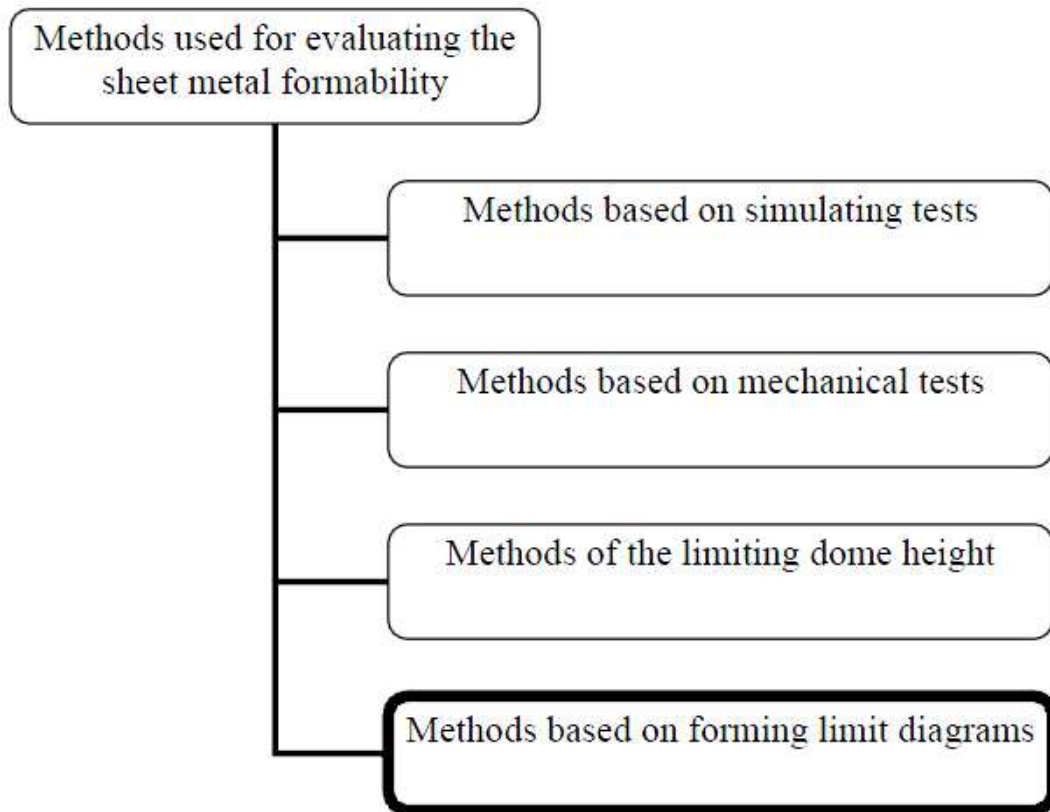


**Figure 2.11 Methods used for evaluating the sheet metal formability**

### ***2.6.1 Forming Limit Diagrams***

The most common used formability evaluating method is forming limit diagrams. This technique involves printing or etching a grid of small with constant diameter on the metal sheet (refer to Figure 2.12) before forming. During forming the initial circles of the grid distort and become ellipses. From the minor and minor axes of these ellipses, the principal strains on sheet specimens can be determined.

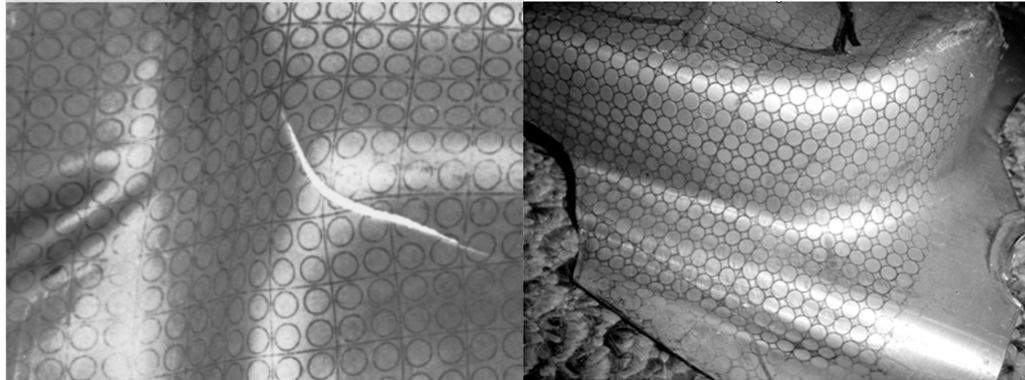


**Figure 2.12 Grid of small circles are printed or etched on sheet metal**

The research in this field was pioneered by Keeler. Keeler plotted the maximum principal strain against the minimum principal strain obtained from such ellipses at fracture of parts after biaxial stretching. This way, a curve limiting the tolerable range is obtained. Later Goodwin plotted the curve of tension/compression domain by using different mechanical tests. In this case, transverse compression allows obtaining high values of tensile strains like in rolling or wire drawing. The diagrams of Keeler and Goodwin together give the values of  $\epsilon_1$  and  $\epsilon_2$  at fracture. Those strain values can be used to determine forming limit diagram (FLD).

There are various tests to determine the FLD experimentally like the uniaxial tensile test, hydraulic bulge test, punch stretching test, Keeler test, Hecker test, Marciniak test, Nakazima test and Hasek test. From these, Marciniak test or hydraulic bulge test is utilized for eliminating friction effects; uniaxial test is preferred for its simplicity and Nakazima test is suitable since it is capable of covering a great variety of strain paths. Hasek test is used in order to prevent wrinkling of the specimens. [8]

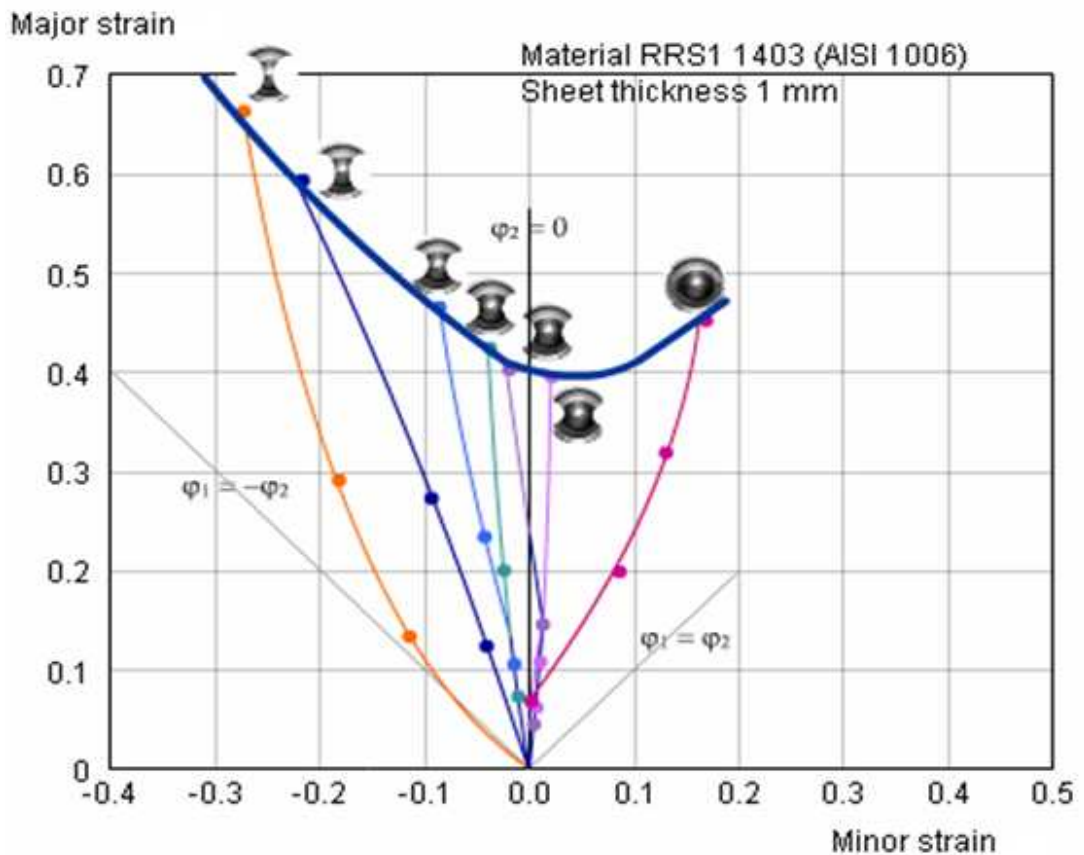


**Figure 2.13 FLD Experiment**

## 2.7 Previous Studies

In this part of the thesis, the previous researches on wrinkling phenomenon in deep drawing will be revised. Finite element method usage in understanding the wrinkling concept in deep drawing process is a common method for these researches. Researches related to the sheet metal forming processes started very early in history, but studies on wrinkling problem are conducted in recent years because of the improvements in automotive industry. The recent demand in automotive industry is obtaining low weight and high strength end products, so sheet metals thicknesses are decreased. As the blank thickness decreases, wrinkling become the most important problem in manufacturing.

Kaftanoğlu [9] developed a method to model flange wrinkling in axisymmetrical deep drawing using the energy method. In this approach, wrinkling occurs if the

plastic work done for deep drawing is higher than the plastic work done for wrinkling. For this purpose, using von Mises yield criteria, a plastic analysis is done for the flange part of the blank, assuming plane stress conditions. For the calculation of work done for wrinkling, wrinkles are assumed to be a sine curve in shape. So the amplitude of the wrinkles are calculated, then using the plastic bending moment, work done for wrinkling is obtained. Using these procedures, plastic work versus reduction strain curves are obtained for both deep drawing and wrinkling. When the slope of the wrinkling curve is greater than deep drawing curve, wrinkling does not occur, since the energy required is greater than deep drawing. Considering the peaks of the wrinkles as plastic hinges, the blank-holder force needed to suppress wrinkling is found in terms of wave number. Experiments are conducted to verify the numerical results with several materials and for several initial blank diameters. Experimental results are in very good agreement with numerical results.

Ramaekers et al. [10], made a research on the deep drawability of a round cylindrical cup. The limiting drawing ratio is tried to be related with some process parameters like anisotropy factor, strain hardening exponent, etc... Upper and lower bound methods are used to obtain theoretical models. Using the theoretical model proposed for deep drawing, estimation for the limiting drawing ratio is tried to be achieved. Some experiments are conducted to verify the model developed. Comparing the results, it is seen that an agreement between the model for deep drawing and experiments. However, a precise prediction of the limiting drawing ratio could not be achieved. The friction coefficient is seen to be an important factor for the drawability of large size products. The study showed that decreasing friction coefficient, increases limiting drawing ratio.

Cao and Boyce [11] examined wrinkling and tearing type of failures in sheet metal forming. For prediction of wrinkling, they used a method proposed by Cao and Boyce. The criterion is based on the energy conservation and minimum work to suppress the wrinkling. Total strain energy values for a perfect plate and for buckling plate are recorded. Then the force/pressure needed to suppress the wrinkling is calculated using the energy difference and wrinkling amplitude. In prediction of

tearing, existing forming limit diagrams are used in correspondence with the local strain histories near possible tearing regions. They also developed a technique named variable binder force in which blank-holding load varies in controlled manner, not a constant blank-holding load was used. A control algorithm is proposed for variable binder force technology. Two examples are used: conical cup drawing and square cup drawing. Finite element models of both cases are analyzed by commercial program ABACUS. Comparison with the experimental results shows that the method is capable of predicting wrinkling and tearing. The control algorithm for variable binder force is tried in both cases, and 16% extra cup forming height is provided for conical cup drawing.

Cao [12], in 1999, developed a method for the prediction of wrinkling using the energy method. In this method, wrinkling criterion proposed by Cao and Boyle [11] is used. This criterion assumes that the initiation of wrinkling is a local phenomenon and depends on the material properties, stress state and sheet thickness. Therefore, the flange wrinkling problem in deep drawing is reduced to the wrinkling problem in a rectangular plate. Then, as stated above, using the energy difference, the binder pressure is determined. Cao, proposed an analytical model for flange wrinkling to calculate the energy values, instead of calculating them by experimental means (using strain histories) or finite element analyses. The material is modeled as planar isotropic. Calculating the energy values with the help of this analytical model, binder pressure is given by previously developed wrinkling criterion. Then analytical model for side wall wrinkling is also developed. Results obtained using analytical model for flange wrinkling are compared with the numerical results of the previous work, which were validated by experiments. There is a good agreement between analytical and numerical results, especially in the prediction of critical buckling stress. Experiments held for side wall wrinkling show that cup forming height prediction of the analytical solution is excellent.

Alves et al. [13] studied the effect of mesh refinement on the prediction of wrinkling and earing. In the simulations, circular blanks of 1 mm thickness and 90 mm radius for aluminum alloy and 105 mm radius for mild steel are drawn. In this

study 8 node elements are used. Four different in-plane mesh refinements are applied. These refinements are based on the die profile radius, element size to die radius ratios of 1.00, 0.75, 0.50, 0.25 are chosen. Also, all refinement schemes are carried out with 1, 2 and 3 layers of finite elements. For the earing profile, number of layers has negligible effects. However, the earing profile highly depends on the refinement. The radius of the outer profile decreases about 10% when finite element ratio decreases from 1.00 to 0.25. In wrinkling prediction, authors concluded that mesh refinement must be better than the earing profile simulation.

Nakamura et al. [14] studied the optimum design of drawbead in sheet metal forming using finite element method and optimization methods. Response surface method is used to increase optimizing efficiency. Parameters for this design procedure are chosen as bead length and bead position. A dynamic explicit finite element code using an updated Lagrangian formulation is used. Blank is modeled using shell elements. For material modeling, elasto-plastic behavior is chosen, where strain hardening is taken into account according to Swift's law. Experiments are conducted for the verification of the results of numerical analysis. A rectangular and stepped cup production is simulated and experimentally carried out. It is concluded that as the bead length increases, the material becomes more resistive, and wrinkling tendency decreases. With the increasing bead length, however, the strains become larger and thickness decreases. Comparing with experimental results, it is seen that the developed system can determine the suitable bead design.

Zeng and Mahdavian [15] investigated the wrinkling behavior in deep drawing at elevated temperatures and compared with cold forming operation. Wrinkling criteria was developed using the equality of moments: When buckling moment becomes equal to total of the restraint moments (restraint moments due to blank-holder force and at die radius, and moment due to resistance of the metal to bending, induced in the metal itself) wrinkling occurs. The analysis was made for two cases – with and without using blank-holder. Experiments were conducted at both ambient temperature and elevated temperature for the verification of the theoretical results. Considering the case without blank-holder, number of wrinkles depends only on the

drawing geometry, with increasing temperature number of wrinkles remain same. The results of experiments are in agreement with theoretical results. When blank-holder is used, however, number of wrinkles is no more independent from temperature. Increasing temperature, increases number of wrinkles formed. The agreement between theoretical and experimental results is satisfactory.

## **CHAPTER 3**

### **OBJECT OF THE PRESENT STUDY**

Sheet metal forming has become one of the most important metal forming processes as sheet metal parts used in automotive and aircraft applications increases. In order to satisfy the demand by the industry, sheet metal forming processes must be investigated very carefully.

The main aim of this study is to investigate the deep drawing process systematically. Deep drawing is one of the most important sheet metal forming process. The process includes many aspects that affect the final product. In order to understand Deep Drawing one must investigate all these variables and their effect on the process. Without extensive knowledge of all these variables, achieving a defect free deep drawn product is hardly possible.

There are some possible failures likely occur during the process, like wrinkling, necking, scratching and surface defects. As thinner materials are tend to be used in automotive industry, wrinkling has become the most important problem among the other defects. The study also aims to investigate wrinkling and its prevention. For this purpose the commercial finite element analysis code PAM-STAMP will be used. PAM-STAMP deep drawing module uses a dynamic-explicit approach in analysis. The elasto-plastic material model is utilized in the program in order to achieve accurate deformation behavior of the material.

To increase the reliability of the study, a previously solved problem from NUMISHEET 2002 Benchmark will be discussed. The results to the problem include both experiment data and simulation data from many attendants. The NUMISHEET 2002 Benchmark findings will be compared to simulation results found from the

commercial Finite Element code PAM-STAMP. The parameters used in the Finite Element code will be optimized to achieve accurate results in reasonable computational time.

After achieving promising results from the benchmark problem, flange wrinkling concept and its prevention will be discussed for deep drawing quality mild steel used in the benchmark. The blankholder force will be studied in order to analyze the flange wrinkling concept. The blankholder force effect on wrinkling formation over the flange region will be studied by applying different blankholder forces. Analyses will start without blankholder force and then blankholder force is added up to the value where there is no flange wrinkling occur in the part. These analyses will be performed for isotropic and anisotropic material models and the results will be discussed. The energy graphs of these analyses will be inspected carefully. Drawing energy and wrinkling energy will be compared in order to understand wrinkling phenomena. Moreover, drawbead will be implemented to the system. Firstly, the drawbead models available in the program will be used in the study in order to realize the effectiveness of drawbeads in preventing flange wrinkling. Drawbeads will be placed at various diameters and their effect on the drawn part will be discussed. Secondly, a user defined drawbead model will be implemented physically to the Finite Element code by designing a new blankholder and die set. The effect of physically added drawbead will be compared with the Finite Element code generated drawbead model. In addition to these studies, finally an experiment will be conducted and it will be numerically simulated. In these experiments, aluminum material (AL1050) with different thickness values will be used. The material properties will be found by performing tension tests. Then, the effect of thickness on the wrinkling formation will be discussed by performing deep drawing test and the experiments will be simulated numerically. The experiment data and data obtained from the Finite Element code will be compared.

In conclusion, this study aims to understand flange wrinkling concept and its prevention by inspecting all possible parameters that effect deep drawing process with the help of experiments and simulations performed.

## **CHAPTER 4**

### **THEORY OF FINITE ELEMENT METHOD**

#### **4.1 Introduction**

In this chapter, the fundamental basics of the Finite Element Method will be introduced, and then the dynamic-explicit Finite Element-procedure will be discussed. In the last section, the Finite Element-code that was utilized in this thesis work PAM-STAMP will be discussed.

#### **4.2 History of Finite Element Method**

The finite element method originated from the need for solving complex problems in civil and aeronautical engineering. The pioneers of the method are known as Alexander Hrennikoff (1941) and Richard Courant (1942). Although the approaches used in their work are different, they have both perform mesh discretization of a continuous domain into a set of sub-domains. These sub domains are called elements. The discretization of continuous problems has been approached differently by mathematicians and engineers. The term finite element was born from the engineering direct analogy view and Clough is the first user of the term. Stiffness matrix and element assembly are introduced by the late 1950's. In 1965, NASA played an important role in developing the Finite Element software NASTRAN. Since then numerous studies have been reported on the theory and applications of finite element method. Today FEM is used for modeling of physical systems of engineering areas.

### 4.3 Basics of Finite Element Method

FEM is used for approximating the behavior of a continuum. This idealization is nearly impossible by using analytical methods. In order to idealize, the whole system is divided into finite number of ideal elements. The behavior of these ideal elements can be estimated. The connection through out these elements is achieved by finite number of points. These points are called nodal points. The function and its derivatives are defined in nodal points. The domain of the function is represented approximately by a finite collection of sub-domains, called finite elements. A mesh is composed of finite elements and nodes. Figure 4.1 illustrates the Finite Element mesh, element and nodes. Elements are connected to other elements through the node points.

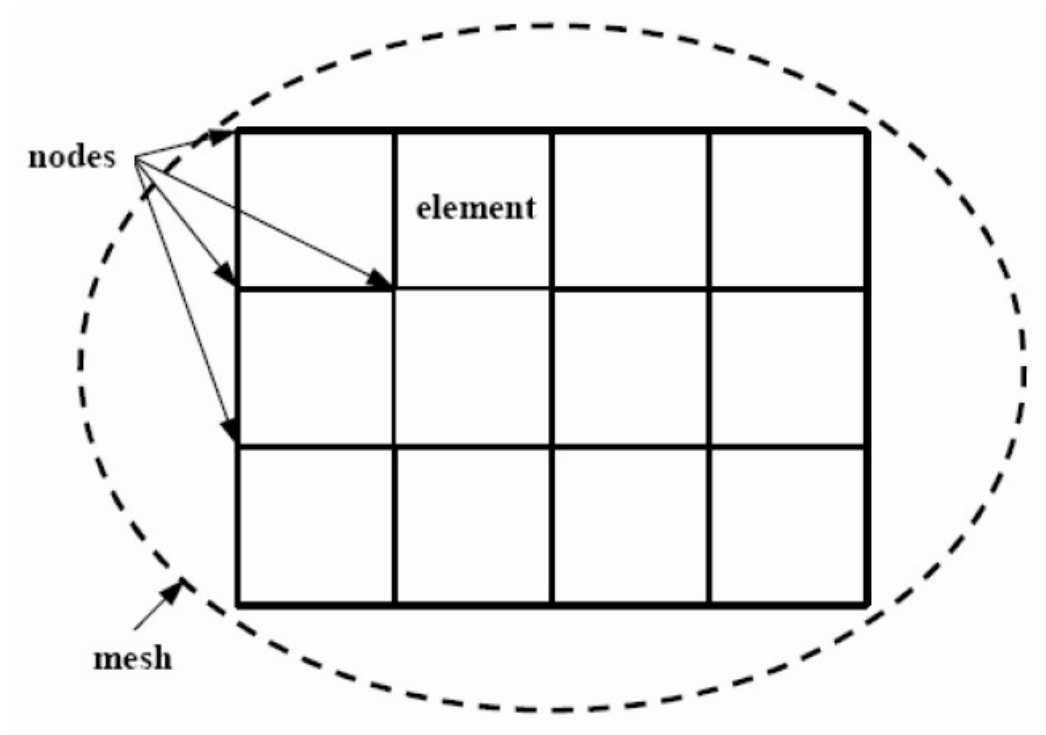


**Figure 4.1 Finite Element Mesh structure**

There are two types of tools, non-deformable (rigid) and deformable tools. For the former one, the mesh is used for representation of the geometry. The finite element and nodes are only visual. On the other hand, the finite elements of a deformable tool are different. The mesh in deformable tool has the characteristic of

the tool material. As the number of these finite element increases, the behavior of the whole system is represented more accurately. In other words, the quality of the results is increased, as the mesh gets finer, smaller. In order to get better results, more elements are used and this yields in dramatic increase of computation time. Computation time increases as finite element of the system increases. In order to achieve good results with acceptable computation time, a compromise has to be made.

The applied forces and displacements to the whole system have affected the elements of the deformable tool. The variance of forces and displacements on the elements are governed by shape functions  $N$ , which relate nodal responses to total element responses. Displacements, velocities and accelerations are calculated at each node. Strains and stresses are calculated at the element level from the node positions.

Afterwards, the relationship between the unknown displacements and known forces at the nodes are determined with a formulation. This formulation can be either linear or non-linear. In the linear formulation (Eq. 4.1) structural stiffness is independent of displacement. However, in non-linear formulation (Eq. 4.2) structural stiffness is dependent on displacement.

$$(F) = [k].(u) \quad (4.1)$$

$$(F) = [k(u)].(u) \quad (4.2)$$

Where

F is force vector

k is stiffness matrix

u is displacement vector.

Non-linearity in finite element analysis is caused by; Geometric nonlinearity, Material nonlinearity and Contact nonlinearity. Metal forming simulations are non-linear problems, so non-linear formulation is required in solving of these problems.

The input parameters of Finite Element Method is illustrated in Figure 4.2

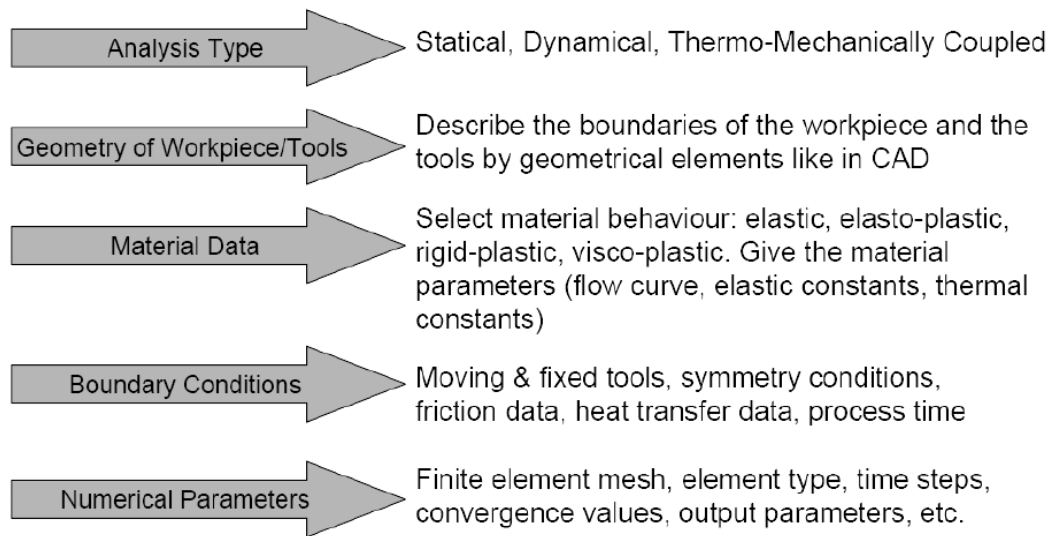


**Figure 4.2 Input parameters of Finite Element Method [16]**

As the Figure 4.2 implies, first parameter is determining the analysis type, then the boundaries of the tools are described by geometrical elements. The other step is using material properties from material data. Then boundary conditions are applied, symmetry, friction data and process time are some examples. The last step is determining the numerical parameters. Mesh, element type and convergence values are set in this step.

#### ***4.3.1 Finite Element Procedures***

There are two procedures available modeling of plastic material behaviors in FEM, namely Rigid-Plastic method and Elastic-Plastic method. In rigid-plastic method, linear kinematics of the finite deformation is not taken into consideration. The formulation takes less time and they are numerically more reliable and robust. However there are some disadvantages in rigid-plastic method. Residual stresses and spring-back cannot be analyzed as they are elastic property. The rigid-plastic material law does not include elastic strains. Another disadvantage is, stress peaks at the transition between elastic and elasto-plastic material zone cannot be detected. The other method is Elastic-plastic method. This model includes the elastic region so it is used for residual stress and spring back analyses. The elastic behavior is taken as

linear function in this model. The plastic region is modeled by using Levy-Mises yield criterion. (Figure 4.3)

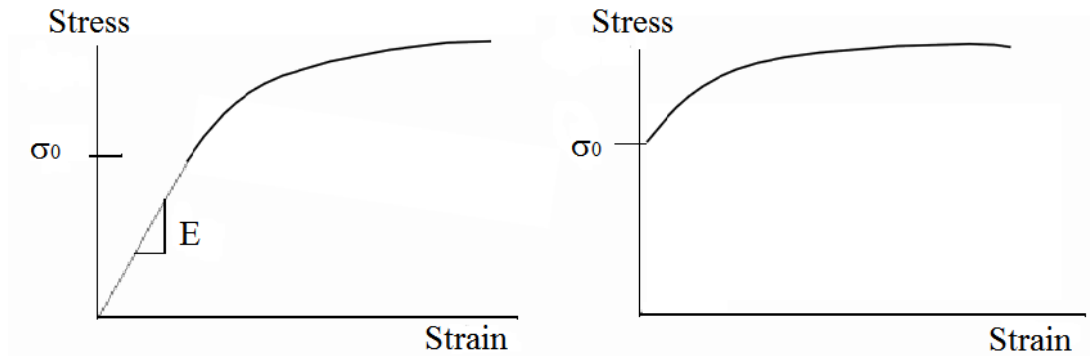


**Figure 4.3 Elasto-Plastic and Rigid-Plastic material behaviors**

#### 4.3.2 Element Stiffness Matrix

Consider a general element as in Figure 4.4, where  $U$  is displacement of the node,  $k$  is the spring stiffness constant and  $f$  is the force acting on the node.

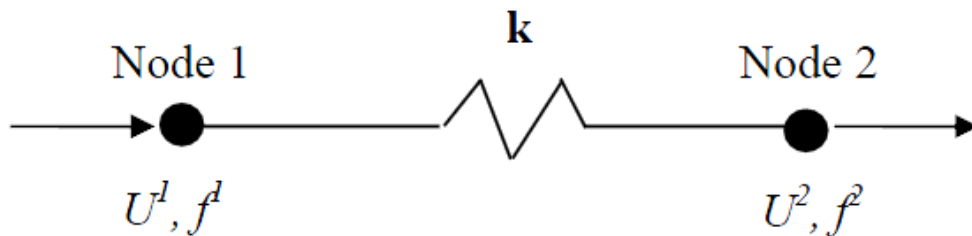


**Figure 4.4 General Element [17]**

From the static law and spring force equation;

$$f^1 = f^2 \quad (4.3)$$

$$f^1 = k.(U^1 - U^2) \quad (4.4)$$

$$f^2 = -k.(U^1 - U^2) \quad (4.5)$$

The matrix form of these equations can be written as such;

$$\{f\} = [k] \cdot \{U\} \quad (4.6)$$

$$\begin{Bmatrix} f^1 \\ f^2 \end{Bmatrix} = \begin{bmatrix} k & -k \\ -k & k \end{bmatrix} \cdot \begin{Bmatrix} U^1 \\ U^2 \end{Bmatrix} \quad (4.7)$$

So the stiffness matrix of the general element is formed.

### 4.3.3 Shape Function

Consider the 2 node element with local coordinate shown in the Figure 4.5.

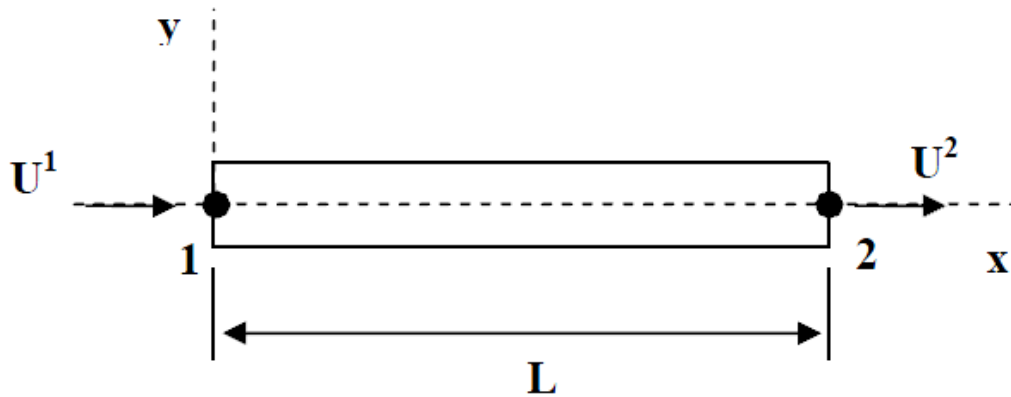


**Figure 4.5 Simple two node element**

The variation of  $U(x)$  can be written as

$$U(x) = \alpha \cdot x + \beta \quad (4.8)$$

In order to find the unknown coefficients  $\alpha$  and  $\beta$ , boundary conditions are applied. The boundary conditions are;

$$U(0) = U^1 = \beta \quad \text{and} \quad U(L) = U^2 = \alpha L + \beta$$

If equations are combined, one can obtain the variation of  $U(x)$  as such

$$U(x) = \left(1 - \frac{x}{L}\right)U^1 + \left(\frac{x}{L}\right)U^2 = N^1.U^1 + N^2.U^2 \quad (4.9)$$

The equation can be written in matrix form.

$$U(x) = [N].\{U\} \quad (4.10)$$

The  $N$  matrix is called the local shape function. Shape functions are used to define the weight of the nodal deformations on the element.

#### 4.3.4 Transformation Matrix

Transformation matrix is used to transform local coordinate system of the element to the global coordinate system. Global and local coordinate systems are shown in the Figure 4.6

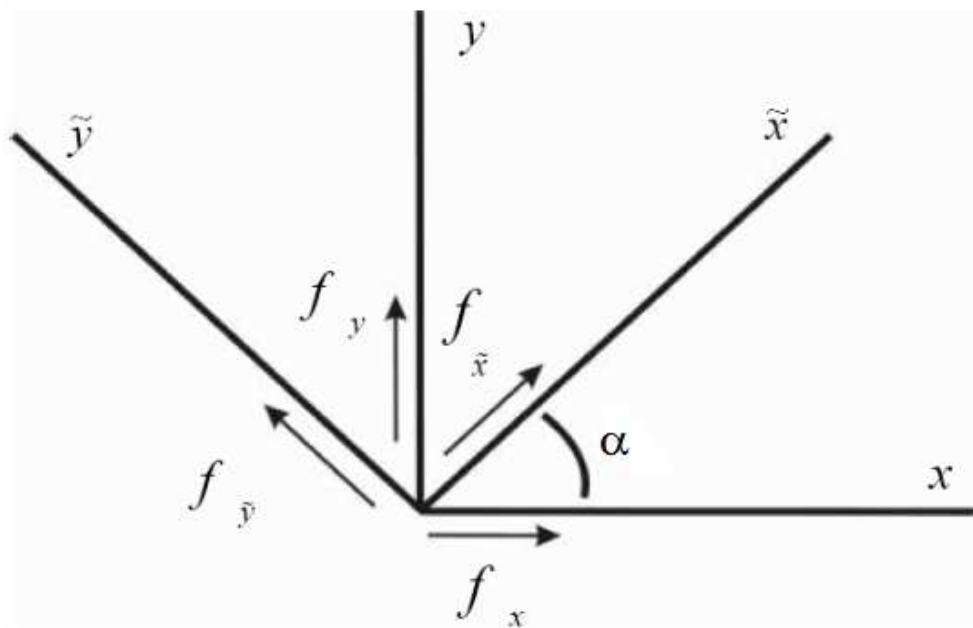


**Figure 4.6 Local and Global Coordinate system of an element**

Figure 4.6 indicates that the rotation  $\alpha$  is the relation between global system and local system. From direction cosines one can obtain displacement relations as such

$$U^1 = \tilde{U}^1 \cdot \cos \alpha + \tilde{V}^1 \cdot \sin \alpha \quad (4.11)$$

$$U^2 = \tilde{U}^2 \cdot \cos \alpha + \tilde{V}^2 \cdot \sin \alpha \quad (4.12)$$

In matrix form;

$$\begin{Bmatrix} U^1 \\ U^2 \end{Bmatrix} = \begin{bmatrix} \cos \alpha & \sin \alpha & 0 & 0 \\ 0 & 0 & \cos \alpha & \sin \alpha \end{bmatrix} \begin{Bmatrix} \tilde{U}^1 \\ \tilde{V}^1 \\ \tilde{U}^2 \\ \tilde{V}^2 \end{Bmatrix} \quad (4.13)$$

In simple form:

$$\{U\} = [T] \cdot \{\tilde{U}\} \quad (4.14)$$

The T matrix is called transformation matrix.

If the simple spring force equation is written for global coordinates using transformation matrix, one can obtain:

$$\{f\} = [k] \cdot \{U\} = [k] \cdot [T] \{\tilde{U}\} \quad (4.15)$$

Multiply both sides by  $[T]^T$ , equation becomes;

$$\underbrace{[T]^T \{f\}}_F = \underbrace{[T]^T [k] [T]}_K \{\tilde{U}\} \quad (4.16)$$

Where global force and global stiffness matrix are obtained as such

$$\{F\} = [T]^T \{f\} \quad (4.17)$$

$$\{K\} = [T]^T [k][T] \quad (4.18)$$

Finally, the equilibrium equation in global coordinates can be written as such;

$$\{F\} = [K]\{\tilde{U}\} \quad (4.19)$$

#### 4.4 Algorithms of Numerical Simulation Solvers

Algorithms used by the solver of numerical simulation, work step-by-step in order to find equilibrium at each step. Two different types of algorithms can be used: explicit and implicit. The main differences are briefly mentioned in the next this section and the mathematical foundations of the dynamic-explicit solver are studied in the next section.

##### 4.4.1 Differences between Implicit and Explicit Approaches

“In the static implicit methods, which were the very first methods used in simulation of metal forming processes, static equilibrium is satisfied in the unknown final configuration of a time increment” [18]. In this method convergence control is used for determining a full static solution to the problems with deformation. Theoretically very large increment sizes can be selected throughout the process, but contact conditions in the problem limit the size of increments, so small enough increments are selected. As the element number increases, computational time increases as well. Required memory for the problem is also high because of matrix inversion step with accurate integration process. The most important disadvantage of implicit method is the divergence problem. In other words, the implicit method may deviate from the solution. Implicit contact algorithms are overloaded due to large number of contact nodes, and this yields to the divergence of the solution. Another problematic point about implicit methods is stiffness matrix singularity at bifurcation points. The instability case of wrinkling initiation is an example of this bifurcation points.

Dynamic explicit method, on the other hand, has many advantages over static implicit method. Robustness of the algorithm is one of the most important advantages of dynamic explicit method. The unbalanced forces are not checked so there is no convergence control in the method. Less memory is required because the matrix inversion is not performed. Also the computational speed is higher compared to the implicit method. The dynamic explicit method is capable of finding of the instabilities, like wrinkling. The formation of wrinkles is initiated by the numerical inaccuracies. The wrinkle region is determined accurately by using this algorithm. The programming can be done easily by using dynamic explicit method. Although the method has some great advantages, there are several disadvantages. The mass matrix must be lumped in order to fulfill the explicit character of numerical algorithm. The computational speed is high as long as there are few element computations. As element computations are increased, the computational speed decreases. In order to increase the computational speed, single quadrature elements can be used, but poor accuracy of stress and strain are achieved. The reduced integration schemes of the elements are used in compensation of the errors caused by the lumped mass matrix. Local stresses and springback calculations cannot be computed accurately because of the reduced integration algorithm. The main differences of implicit and explicit methods are summarized in the Table 4.1.

**Table 4.1 Main Differences in Explicit and Implicit Approaches**

	<b>Explicit</b>	<b>Implicit</b>
<b>Increment</b>	Very small time step	Large
<b>Inversion of matrix</b>	Easy diagonal matrix	Inversion of full stiffness matrix at each increment
<b>Robustness</b>	Result is guaranteed when using small time steps	Sometimes instability in case of: large deformations, large contact surface, non-linear material properties
<b>Needed Memory</b>	Small	Large
<b>CPU Time</b>	May be large	Generally small
<b>Application</b>	Processes with highly non-linear behavior	Static and quasi-static processes

#### 4.4.2 Dynamic- Explicit Finite Element Method

The dynamic-explicit methods are based on the solution of a dynamic problem, even if it is quasi-static as in most applications of metal forming. A simple one dimensional mass-spring-damper system is considered to express the bases of these methods (Figure 4.7).

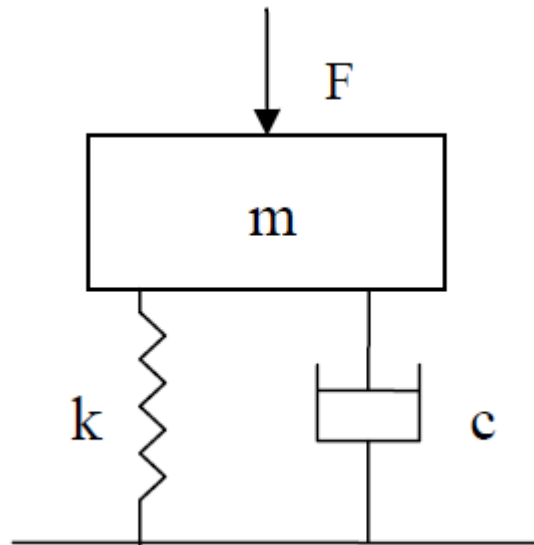


**Figure 4.7 Simple one dimensional mass-spring-damper system**

The equation of motion for the free-body diagram of mass is given as

$$m\ddot{u} + c\dot{u} + ku = F(t) \quad (4.20)$$

where

$m$  is the mass of the body

$c$  is the damping coefficient of the damper

$k$  is the stiffness of spring

$u$  is the displacement of mass measured from its static equilibrium position

$\dot{u}$  is the instantaneous speed of the mass at time  $t$

$\ddot{u}$  is the instantaneous acceleration of the mass at time  $t$

$F(t)$  is the external force as a function of  $t$

Eq. (4.20) can be divided by  $m$  and is rewritten as:

$$\ddot{u} + 2\zeta\omega\dot{u} + \omega^2u = f(t) \quad (4.21)$$

where

$$\omega = \sqrt{k/m} \quad (4.22)$$

$$\zeta = c/(2\sqrt{km}) \quad (4.23)$$

$$f(t) = F(t)/m \quad (4.24)$$

$\omega$  is the eigen-frequency of the system and  $\zeta$  is the viscous damping factor. According to the value of  $\zeta$ , the response of the system alternates. For  $\zeta > 1$  the system is over damped, for  $\zeta < 1$  under damped and for  $\zeta = 1$  critically damped. Critically damped systems tend to reach the equilibrium position the fastest when an external force is applied. For the critically damped system ( $\zeta = 1$ ) from Eq. (4.5) damping coefficient should be equal to

$$c = 2\omega m \quad (4.25)$$

The equation of motion given in Eq. (4.21) can be solved by applying the central difference method:

$$\ddot{u}^t = \frac{1}{\Delta t} (u^{t+\Delta t} - 2u^t + u^{t-\Delta t}) \quad (4.26)$$

$$\dot{u} = \frac{1}{2\Delta t} (u^{t+\Delta t} - u^{t-\Delta t}) \quad (4.27)$$

Substituting Eq. (4.26) into Eq. (4.27) and rearranging yields:

$$\left[ \frac{1}{(\Delta t)^2} m + \frac{1}{2\Delta t} c \right] u^{t+\Delta t} = F(t) - ku^t + \frac{m}{(\Delta t)^2} [2u^t - u^{t-\Delta t}] + \frac{c}{2\Delta t} u^{t-\Delta t} \quad (4.28)$$

The solution of displacement at time  $t + \Delta t$  only depends on the displacement of the known states at times  $t$  and  $t - \Delta t$ , this time discretization scheme is named as

dynamic explicit integration of the equation of motion. In case of the implicit integration methods, the solution depends also on the displacements of the unknown state at time  $t + \Delta t$ , which is usually expressed as dependency of the stiffness term on the unknown displacements [8].

The time step should be smaller than a critical time step  $\Delta t_{cr}$ , which is

$$\Delta t_{cr} = \frac{T}{\pi} = \frac{2}{\omega} = 2\sqrt{\frac{m}{k}} \quad (4.29)$$

where  $T$  is the eigen-period of the system to satisfy the condition for convergence.

Moreover for the 3-D generalization of deformable body, virtual work equation can be modified by adding an inertia term to yield

$$\int_V T_{ij} \delta u_{ij} dV = \int_V t_i \delta u_i dA - \int_V \rho \ddot{u}_i \delta u_i dV \quad (4.30)$$

where

$T_{ij}$  is the Cauchy stress tensor

$u_{ij}$  is the gradient of the displacements

$\ddot{u}_i$  is the acceleration of material

$t_i$  is the traction vector

$\delta$  is the variational operator

$\rho$  is the density

The finite element spatial discretization of this equation yields

$$[M]\{\dot{u}^t\} = \{F^t\} - \{I^t\} \quad (4.31)$$

where

$[M]$  is the consistent mass matrix

$\{F\}$  is the external force at time  $t$

$\{I\}$  is the internal force at time  $t$

An artificial damping term  $[C]$  should be added to Eq. (4.31) in order to provide the stability. This yield to

$$[M]\{\ddot{u}^t\} + [C]\{\dot{u}^t\} = \{F^t\} - \{I^t\} \quad (4.32)$$

Using central difference method given in Eq. (4.26 and 4.27) the above equation can be rewritten as

$$\begin{aligned} \frac{1}{(\Delta t)^2}[M] + \frac{1}{2\Delta t}[C]\{u^{t+\Delta t}\} &= \{F^t\} - \{I^t\} + \frac{1}{(\Delta t)^2}[M](2\{u^t\} - \{u^{t-\Delta t}\}) \\ + \frac{1}{2\Delta t}[C]\{u^{t-\Delta t}\} & \end{aligned} \quad (4.33)$$

The initial conditions for nodal displacements, velocities, internal and external forces at the time  $t = 0$  are given; however the nodal displacements at time  $\Delta t$  are also required at the very first step and it can be obtained from:

$$\{u^{-\Delta t}\} = \{u^0\} - \{\dot{u}^0\}\Delta t - \frac{1}{2}\{\ddot{u}^0\}^2 \quad (4.34)$$

where the initial accelerations  $\{\ddot{u}^0\}$  is given by

$$[M]\{\ddot{u}^0\} = \{F^0\} - \{I^0\} - [C]\{\dot{u}^0\} \quad (4.35)$$

To increase the computational efficiency the consistent mass and damping matrices are approximated by diagonal (lump) matrices: Eq. (4.33) is uncoupled on the left hand side and no factorization is necessary. Furthermore, this approximation

has proven itself quite useful since on one hand the central difference method is known to shorten the vibration period whereas the use of lumped matrices increase this period, thus a balanced total effect is obtained at the end [8].

The lumped damping matrix is assumed as the linear combination of the mass and the stiffness matrix:

$$[C] = c_1 [M] + c_2 [K] \quad (4.36)$$

It is difficult to obtain the damping properties of the structure, so that for  $c_1$  an approximation based on the critical damping condition given in Eq. (4.25) is suggested as

$$c_1 = 2\omega \quad \forall \text{ degree of freedom} \quad (4.37)$$

On the other hand,  $c_2$  is usually taken as zero, but Schweizerhof and Hallquist [19] suggest modifying Eq. (4.33) by using an approximation instead of using Eq. (4.26 and 4.27).

$$\{\dot{u}^t\} \approx \left\{ u^{t-\frac{\Delta t}{2}} \right\} \quad (4.38)$$

yielding

$$\left( \frac{1}{(\Delta t)^2} [M] \right) \{u^{t+\Delta t}\} = \{F^t\} - \{I^t\} + \left( \frac{[M]}{2\Delta t} - [C] \right) \left( \frac{\{u^t\} - \{u^{t-\Delta t}\}}{\Delta t} \right) \quad (4.39)$$

The explicit algorithm integrates through time by using small time increments. The central difference operator is conditionally stable as already pointed out and the stability limit for the operator with including the damping is simplified from Eq.(4.29) to

$$\Delta t \leq \frac{2}{\omega_{\max}} \left( \sqrt{1 + \zeta^2} - \zeta^2 \right) \quad (4.40)$$

where  $\xi$  is the fraction of critical damping in the highest mode. Eq. (4.40) is valid for linear systems but it can be used as an estimate for nonlinear systems such as elasto-plastic metal forming problems. It is estimated that the critical time step for non-linear problems is about 50 - 80 % lower than the one computed for the linear systems [8].

In a finite element simulation the critical time step can be also approximated for each element at each step by

$$\Delta t \leq \frac{L}{c_d} \quad (4.41)$$

where  $c_d$  is the elastic wave speed of material (speed of sound in that material) and  $L$  is the characteristic element dimension. The elastic wave speed is obtained from

$$c_d = \sqrt{\frac{2G(1-\nu)}{(1-2\nu)\rho}} \quad (4.42)$$

Calculation of each increment in dynamic-explicit methods is very robust and less time consuming than implicit methods; however, too small time steps result in unacceptable high number of increments, which make the dynamic-explicit methods infeasible. Two numerical tricks are applied to avoid this.

The total process time is reduced by exaggerating speed of moving tool or increasing the gradient of loading curves. In order to compensate the undesired effects of artificial inertia forces numerical damping is applied. This treatment is not suggested and an additional precaution should be taken for the analysis involving

strain rate sensitive materials. In addition, increase in the density of the material leads a reduction in the total number of increments since it reduces the sound of speed in the material and hence increases the minimum allowable time step. The additional artificial inertia forces cannot be reduced by introducing numerical artificial damping but these forces may be taken over by the rigid dies since in deep drawing most of the workpiece is supported by the dies [8]. Therefore, dynamic-explicit methods can be applied to the sheet metal forming processes successfully from this point of view.

#### 4.4.3 Plastic Work

In the analysis of deep drawing and wrinkling problems, the elastic strains are negligible compared to the plastic strains. Total deformation is equivalent to plastic deformation. Since plastic deformation is experienced, equations of plastic flow rules the deformation. [9]

Von-Mises yield criterion for an isotropic strain-hardening material is used. When expressed in terms of the principal stresses:

$$(\sigma_1 - \sigma_2)^2 + (\sigma_2 - \sigma_3)^2 + (\sigma_3 - \sigma_1)^2 = 2\bar{\sigma}^2 \quad (4.43)$$

where  $\bar{\sigma}$  is the equivalent stress.

Levy-Mises plastic strain increments:

$$d\varepsilon_1 = \frac{2}{3}d\lambda \left[ \sigma_1 - \frac{1}{2}(\sigma_2 + \sigma_3) \right] \quad (4.44)$$

$$d\varepsilon_2 = \frac{2}{3}d\lambda \left[ \sigma_2 - \frac{1}{2}(\sigma_1 + \sigma_3) \right] \quad (4.45)$$

$$d\varepsilon_3 = \frac{2}{3}d\lambda \left[ \sigma_3 - \frac{1}{2}(\sigma_1 + \sigma_2) \right] \quad (4.46)$$

where

$$d\lambda = \frac{3}{2} \frac{d\bar{\varepsilon}}{\bar{\sigma}} \quad (4.47)$$

Volume remains constant during plastic flow and can be expressed as:

$$d\varepsilon_1 + d\varepsilon_2 + d\varepsilon_3 = 0 \quad (4.48)$$

During plastic deformation, the total work done by the stress components is equal to work done by equivalent stress. The work equation is given as:

$$w = \int \sigma_{ij} \cdot d\varepsilon_{ij} = \sum \bar{\sigma} \cdot d\bar{\varepsilon} \quad (4.49)$$

where the integral and summation are taken over the actual strain paths from the initial state of the material. In equation 4.49, the equivalent plastic strain increment is defined as:

$$d\bar{\varepsilon} = \sqrt{\frac{2}{3}} \left[ (d\varepsilon_1)^2 + (d\varepsilon_2)^2 + (d\varepsilon_3)^2 \right]^{\frac{1}{2}} \quad (4.50)$$

#### 4.5 Features of PAM-STAMP 2G

As stated before, PAM-STAMP 2G is the FEA-package that is utilized for the numerical simulations within this thesis study. In this section the properties of the package (modules, specifications, and the user environment) will be overviewed. PAM-STAMP 2G is specifically designed for sheet metal forming operations. The main solver of the package is dynamic-explicit algorithm. However for springback calculations an iterative implicit solver is also present. The program is manipulated via a graphical user interface. Subjectively, the graphical representations of the package is colorful and of good quality. [21]

The package is composed of several modules shown in Figure 4.8.

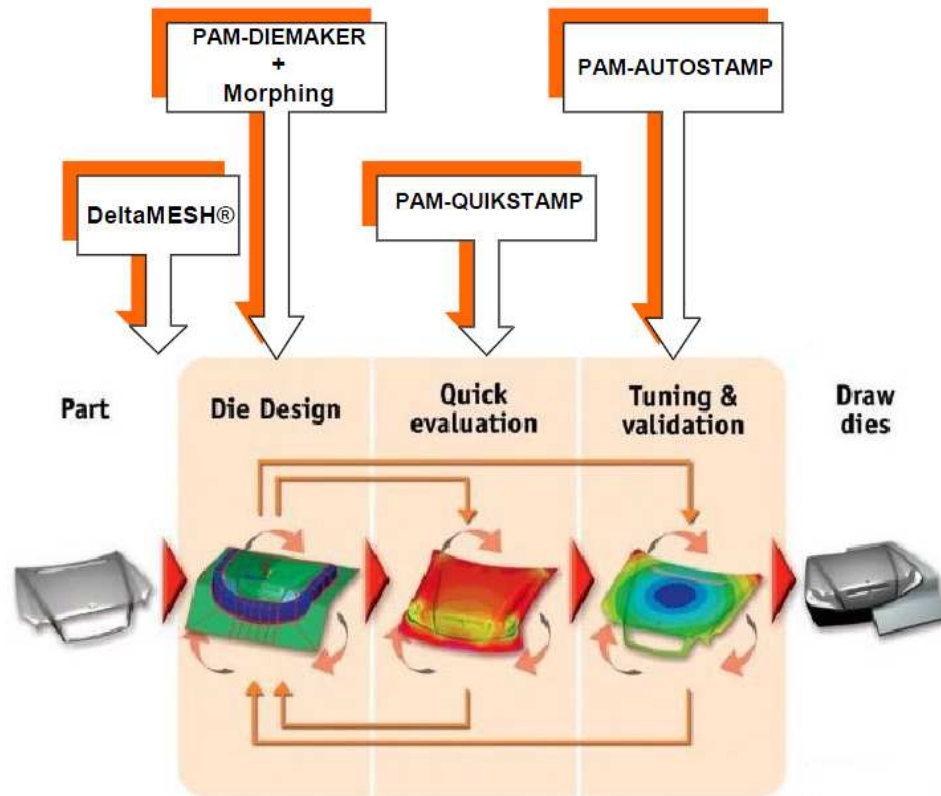


**Figure 4.8 PAM-STAMP 2G Modules [20]**

- **DeltaMESH®** is an automatic meshing tool suited to stamping simulations. It is optimized to generate meshes very quickly, from CAD models of the stamping tools, perfectly adapted to the needs of numerical stamping simulations.
- **PAM-DIEMAKER** is an easy-to-use geometry modeler for the high-speed design of deep-drawing tools. With PAM-DIEMAKER the time taken to develop a tool is, in comparison to a conventional method, substantially reduced.
- The **Morphing** technology enables rapid and direct manipulation of the part geometry, with instantaneous mesh updating, without resorting to time-consuming operations such as modifying the geometry in the CAD application and the ensuing re-meshing. As the iterations progress, the

run-off becomes increasingly realistic and complex. The CAD definition of the part is only updated after the run-off is optimized and validated.

- **PAM-QUIKSTAMP** is a simplified approach where some components of the press tool are deduced from the initial part and where the real kinematics is not completely defined. PAM-QUIKSTAMP allows the die designer to check and evaluate different die geometry parameters issued from PAM-DIEMAKER within minutes.
- **PAM-AUTOSTAMP** enables the user to simulate a real stamping process taking into account industrial conditions such as gravity, binder development, multiple stage forming, trimming, springback, flanging...

## CHAPTER 5

### NUMERICAL AND EXPERIMENTAL RESULTS

#### 5.1 Introduction

In this study, commercial Finite Element program PAM-STAMP is used to simulate the deep drawing process. The study started with a previously solved problem by the participants of NUMISHEET 2002. Both experimental and numerical solutions for the problem are available in NUMISHEET 2002. The results of PAM-STAMP program are compared to the available data from NUMISHEET 2002 in order to determine the reliability and accuracy of the Finite Element code.

After achieving reliable and accurate results from PAM-STAMP program, the effect of blankholder force on wrinkling is discussed. Wrinkling is inspected for both isotropic and anisotropic material models while keeping the model geometry fixed and the results are discussed. A graph of blankholder force versus number of waves formed is illustrated for both two material models. Energy graphs are inspected thoroughly to understand wrinkling formation in the flange region.

Drawbead models are utilized throughout the study to understand and inspect the drawbead effect on wrinkling concept. PAM-STAMP has three different drawbead models available in the Finite Element code. In addition to these pre-defined drawbead models, three different drawbead models are designed and utilized within the Finite Element code. The effects of the designed drawbead models and available drawbead models on the flange wrinkling are compared and results are illustrated.

Another important issue about wrinkling is material thickness. Same material (AL1050) with different thickness values are used in deep drawing experiments. The

material forming parameters are obtained from tension tests. Tension tests are performed for thicknesses of 0.5, 1.0, 1.2 and 2.0 AL1050 materials by using same die and punch set. Material data gathered from tension tests are used in the deep drawing experiments simulated in PAM-STAMP. The experimental results are compared to the simulation results. The effect of thickness on wrinkling problem is inspected through many simulations and experiments.

## 5.2 Benchmark Problem

Axisymmetrical cup drawing is selected as a Benchmark problem. Setup and geometry of tools used in NUMISHEET 2002 are given in Figure 5.1.

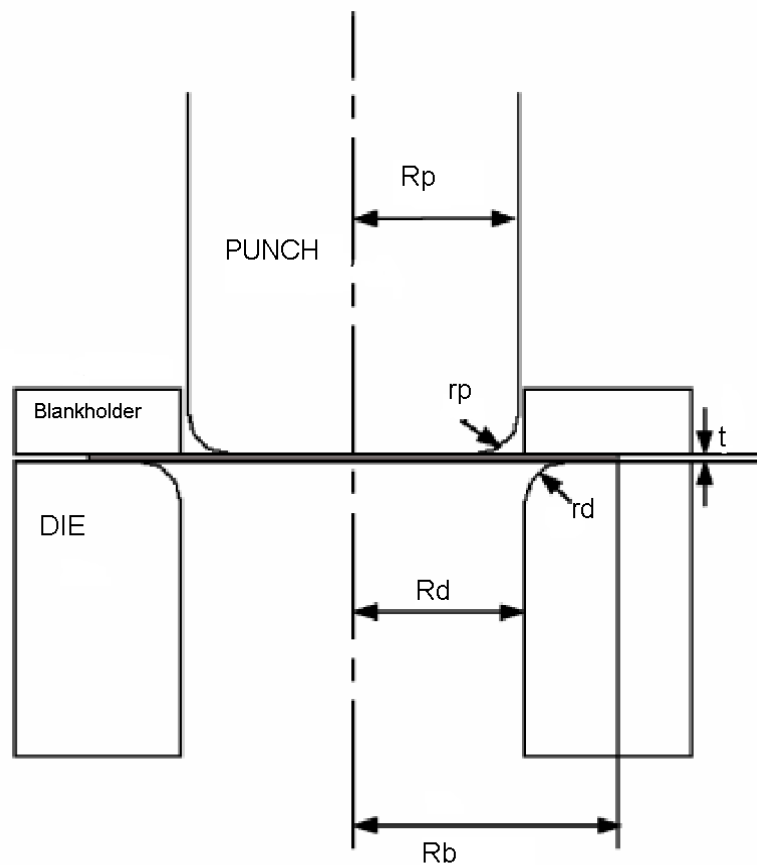


**Figure 5.1 Tool geometry of Benchmark problem**

The punch radius,  $R_p$  is 50.00 mm and die radius,  $R_d$  is 51.25 mm. The fillet radii of die,  $r_d$  and punch,  $r_p$  are 9.5 mm and 7.0 mm, respectively. During the study, 1 mm thickness steel sheet with 105 mm blank radius,  $R_b$  is used. [22]

The blank material is provided by POSCO (Korea), which is mild steel with Deep Drawing Quality (DDQ). The material properties are presented in Table 5.1.

**Table 5.1 Material properties of DDQ mild steel**

Material	E (GPa)	$\rho$ (g/cm <sup>3</sup> )	$\nu$	$\epsilon_0$	K (MPa)	n	R (0°)	R (45°)	R (90°)
DDQ Steel	221,368	7,8	0,3	0,00876	547,3	0,2692	2,160	1,611	2,665

Plastic flow curve of the steel sheet can be illustrated according to the Swift Law.

$$\sigma = K \cdot (\epsilon + \epsilon_0)^n \quad (5.1)$$

Plastic flow curve of the steel material can be seen in Figure 5.2.

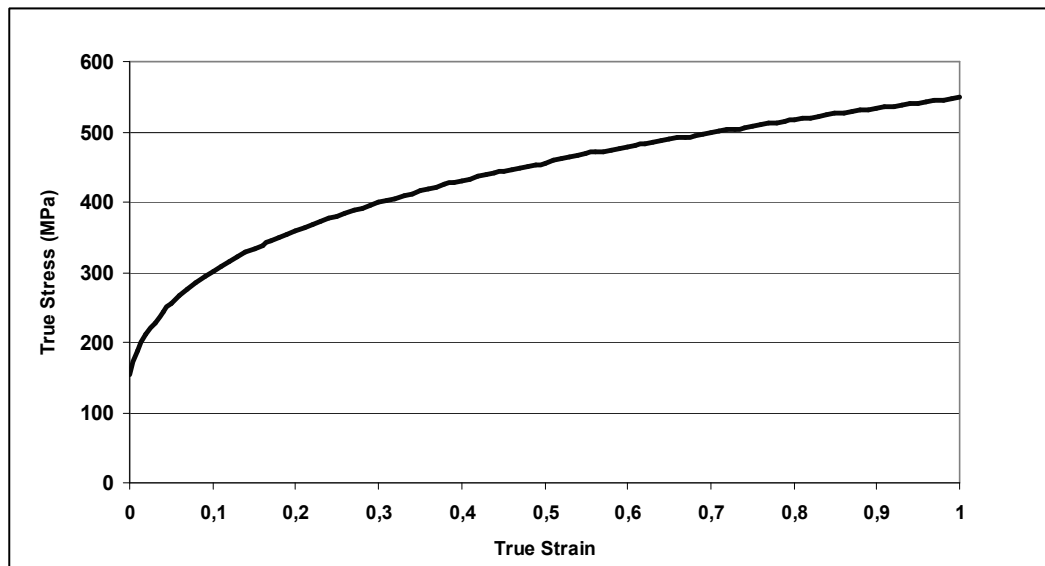


**Figure 5.2 True Stress vs. True Strain curve of DDQ mild steel**

The anisotropy constants of the material can be investigated thoroughly. The normal anisotropy and the planar anisotropy are defined as follows,

$$r_n = \frac{r_0 + 2 \cdot r_{45} + r_{90}}{4} \quad \& \quad \Delta r = \frac{r_0 - 2 \cdot r_{45} + r_{90}}{4} \quad (5.2)$$

$$r_n = 2.012 \quad \& \quad \Delta r = 0.401 \quad (5.3)$$

As mentioned in Chapter 2, a material with a high  $r_n$  value will experience less thinning during a deep drawing operation than a material having a smaller  $r_n$  value, provided that their flow characteristics are identical. Steel materials usually have  $r_n$  values larger than 1, in this particular case this value is 2.012, which is very high. On the other hand, planar anisotropy is directly related to earring. The planar anisotropy value is 0.4 for DDQ mild steel. As expected, planar anisotropy value is positive and it is common for steel to have positive planar anisotropy.

The process specifications and assumptions are given by NUMISHEET. In the deep drawing simulation, punch progression is given as 40 mm. In other words, drawing depth is specified as 40 mm. The friction coefficients are provided by the steel sheet manufacturer PASCO. Average Coulomb Friction Coefficient at all contact surfaces are provided as 0.0426 for steel blank. Two blankholder force values are specified. The high blank holder force is 70 kN and low blank holder force is 10 kN. The processes are assumed to occur at constant room temperature, so heat effects are neglected. Also, strain effects are neglected. In addition, blankholder, punch and die are assumed to be rigid bodies in the simulations.

### ***5.2.1 Process Parameters***

In Figure 5.3, finite element model of cup drawing process is shown. Process parameters, such as punch velocity and element size are investigated for the given material properties. Process specifications are decided throughout the series of simulations and their effects on the results are presented.

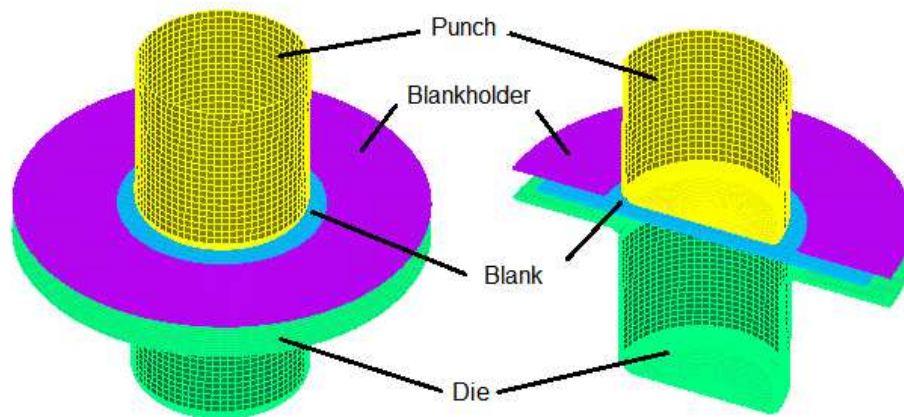


**Figure 5.3 Mesh structures of Half and Full model**

### ***5.2.2 Punch Velocity***

In this section, the effect of punch speed on the analysis accuracy and computation time is inspected. For this purpose, the following punch speeds are used:

50 mm/s, 100 mm/s, 250mm/s, 500 mm/s, 1000 mm/s, 2500 mm/s, 5000 mm/s, 10000 mm/s, 50000 mm/s.

First simulation is done with constant punch velocity of 10 mm/s, which is a relatively low speed. The simulation at this low speed did not provide any solutions before 1 day of computing time. Therefore, it is decided to begin with higher punch velocity values and the first satisfactory result is obtained when the punch velocity is 50 mm/s, which is also the recommended punch speed by NUMISHEET. A series of simulations with different punch velocities for different meshes are performed. For a coarse mesh, punch velocity may change the thickness distribution slightly (Figure 5.4), whereas for a finer mesh, thickness distribution results display insignificant dissimilarities (Figure 5.5). For finer meshes, an accurate range of punch velocity lies between 50 mm/s and 10000 mm/s.

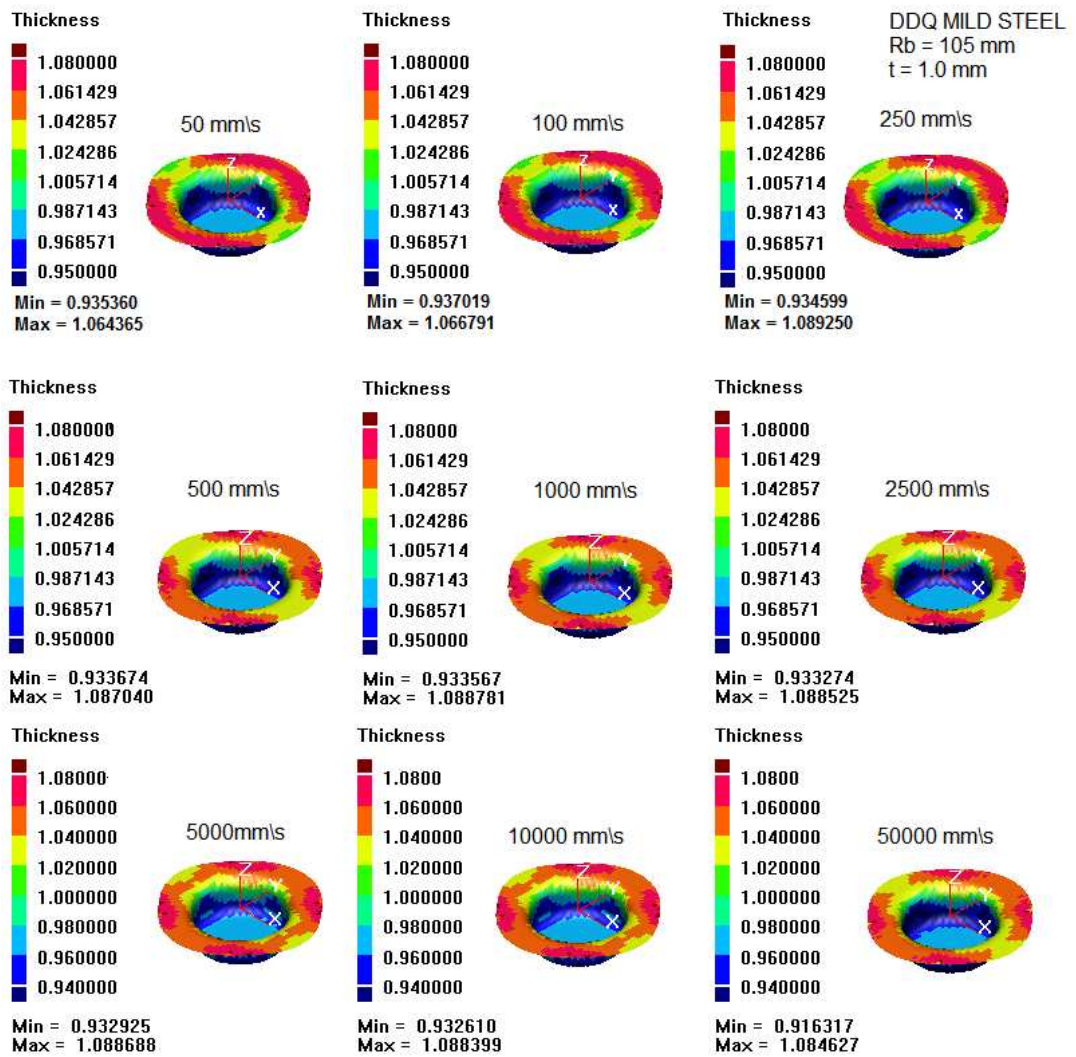
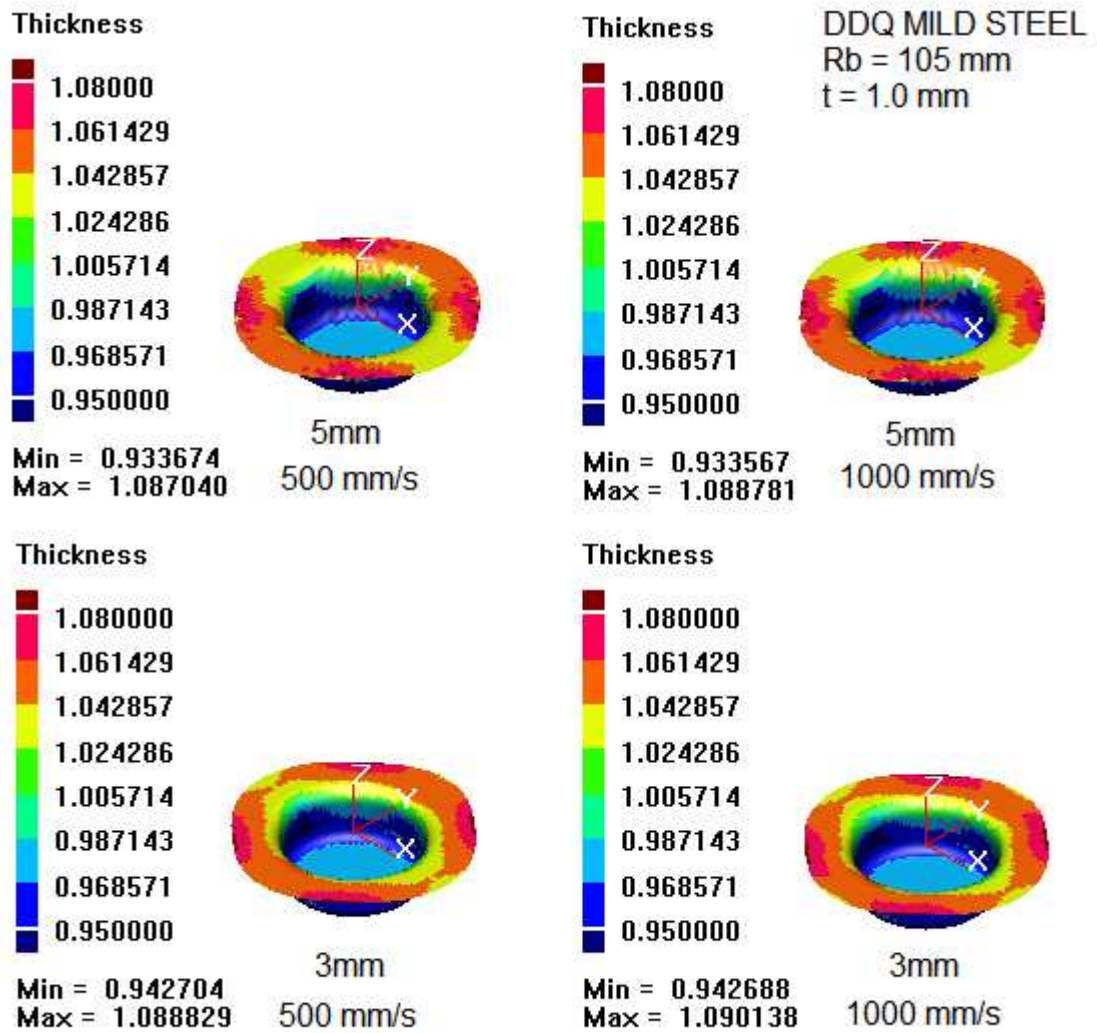
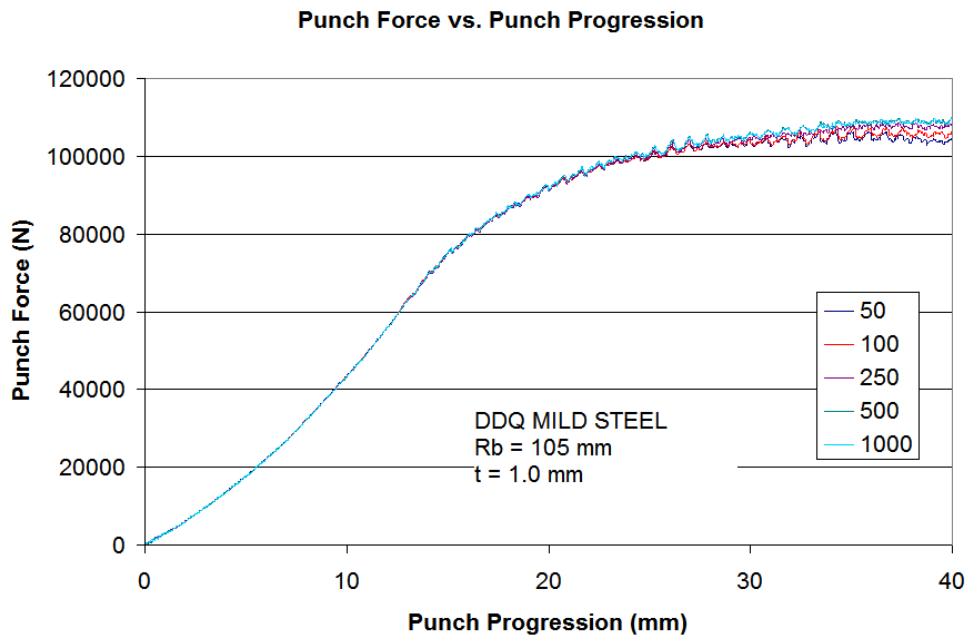


Figure 5.4 Punch speed effect on thickness distribution of a 5mm Element Size



**Figure 5.5 Punch speed effect on thickness distribution of a 3mm Element Size**

As the minimum and maximum thickness values in each simulation are inspected, it could be stated that the maximum variation in thickness values in both materials is less than 2%. The effect of varying punch velocity can also be observed in forming force vs. punch displacement curves. As seen in Figure 5.6, the results obtained by simulations in the optimum range of velocity (50 mm/s to 1000 mm/s) are even more similar to each other than of the thickness contour.



**Figure 5.6 Punch Force vs. Punch Progression curves for different Punch Velocities**

On the other hand, when the punch speed exceeds 10000 mm/s for the workpiece, the presence of large vibrations cause the results to become invalid due to the dynamic effects (Figure 5.7).

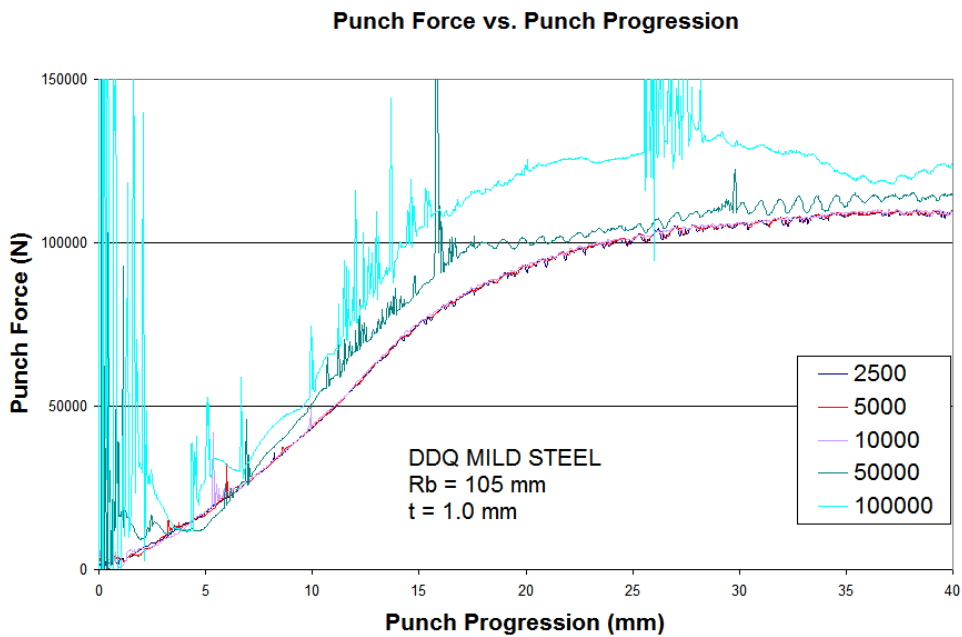


**Figure 5.7 Punch Force vs. Punch Progression curves for unacceptable Punch Velocities**

Computation time is also very important for a simulation. While performing a simulation, accurate results are targeted in reasonable amount of time. Punch speed effect on Computational Time for 5mm element size mesh is illustrated on Figure 5.8.

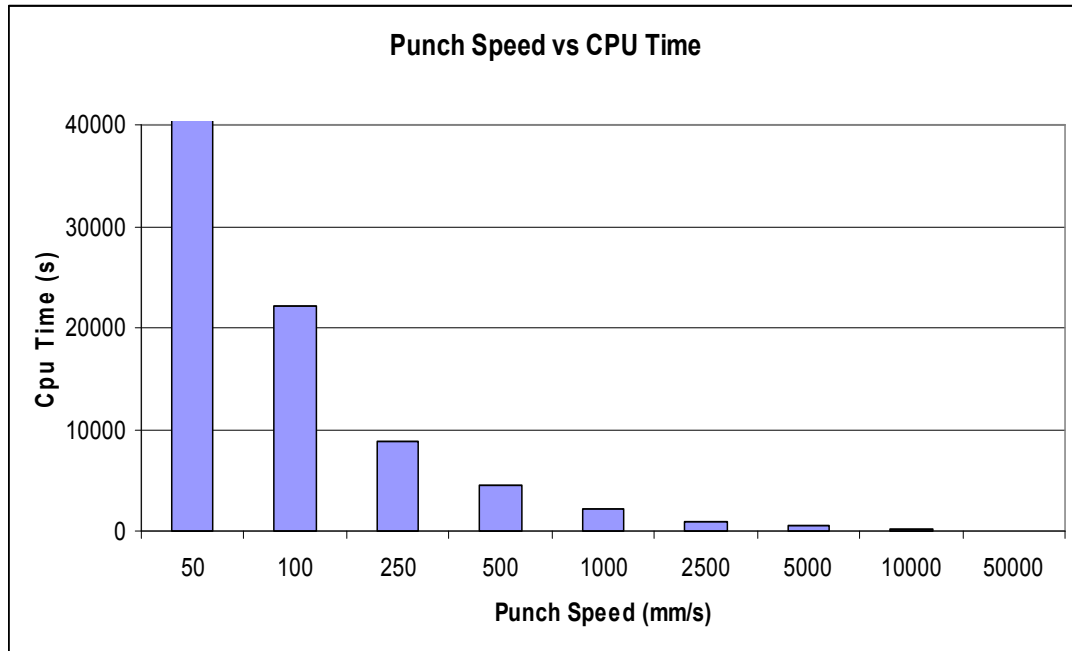


**Figure 5.8 Punch Speed effect on Computational Time for 5mm mesh size**

As it can be observed from Figure 5.8, computation time increases as the punch speed decreases. For 50000 mm/s punch speed, the simulation takes only 80 seconds which is very small compared to the other speeds. However, for 50 mm/s punch speed, the simulation takes 43000 seconds (nearly 12 hours). Punch speeds between 250 mm/s and 1000 mm/s enables both accurate enough and fast simulation results.

In the light of these facts, a compromise revealed that one can use 500 mm/s punch speed for both accurate and fast simulations, according to the thickness distributions, punch force vs. progression graphs and computational time. For faster and accurate simulations, one must avoid using punch speeds below 250 mm/s. In order to achieve good quality results, dynamic effects should be very small. At 2500 mm/s punch speed, blankholder vibrates and can not hold the blank accurately. To avoid dynamic effects, one should not choose tool speeds above 2500 mm/s.

### 5.2.3 Element Size and Refinement

Element size plays an important role throughout a simulation. Element size affects both the computation time and the accuracy of the results. When a tool is meshed coarsely, the results come out unacceptable. The rigid bodies like punch, blankholder and die should be meshed finer enough in order to avoid contact problems. A coarse mesh for punch may result in penetration problems in the simulation. In order to achieve good results, general element sizes of die, punch and blankholder meshes are chosen to be 5 mm. However in fillet regions, finer mesh is selected. The mesh of the die used in the simulation shown in Figure 5.9.

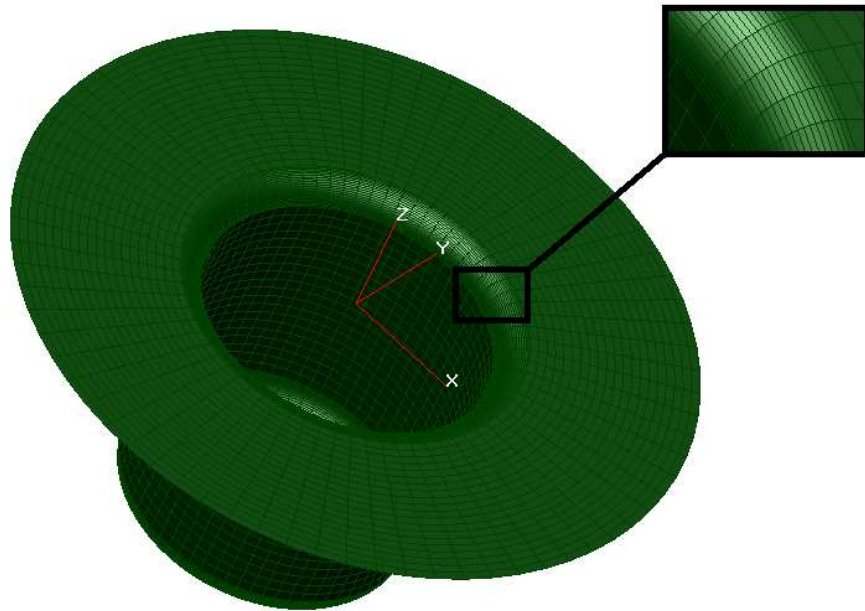


**Figure 5.9 Fillet mesh detail of the Die**

As mentioned before, in order to obtain more precise results, it may be preferred to decrease the deformable body element sizes. However, the increase in number of elements not only results in a drastic increase in Computational time but also may cause an over stiff discretization.

In PAM-STAMP, there is a good solution to overcome problems arise from coarse meshing. This solution is called Refinement, or adaptive meshing. By

utilizing adaptive meshing one can use a coarse mesh to simulate the deep drawing operation.

The adaptive meshing automatically refines mesh of a deformable body where and when certain conditions exist. The program performs a one-level refinement when this element is cut into four other elements (each edge is cut in two). See the Figure 5.10 for 4-level refinement.

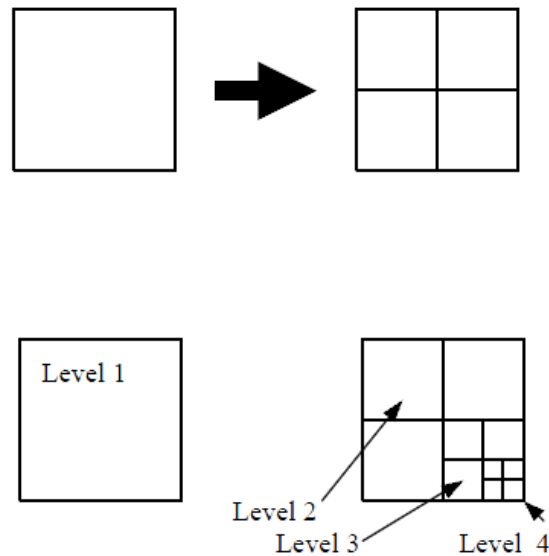


**Figure 5.10 Refinement procedures [20]**

Usually, Finite Element codes for sheet metal forming applications use two criteria to determine whether there should be a refinement: angle criterion and geometrical criterion.

In the angle criterion (Figure 5.11), solver refines an element when the variation of the angle between its normal and that of one of its neighbor elements exceeds a certain limit angle (generally  $10^\circ$ ). This criterion is useful for the determination of wrinkling. [20]

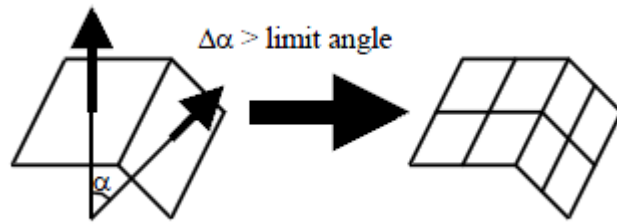


**Figure 5.11 Angle Criteria [20]**

The geometrical criterion adapts the density of the mesh according to the curvature of the tool segments close to the deformable body (Figure 5.12).

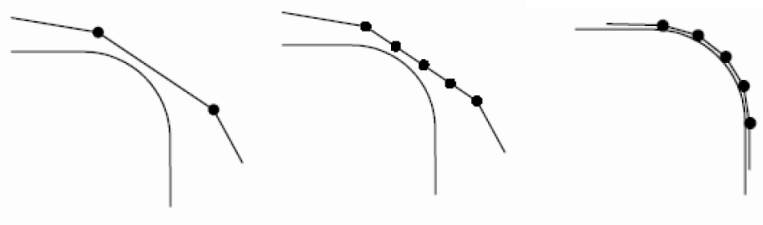


**Figure 5.12 Geometrical Criterion [20]**

In order to comprehend the effects of element size and refinement, several simulations are performed. The simulations include results for 3mm and 5mm element size without refinement, and also 5mm with level 2 refinement and level 3 refinement element sizes. The thickness contour for the simulations is calculated for 500 mm/s punch velocity. The results are illustrated in Figure 5.13.

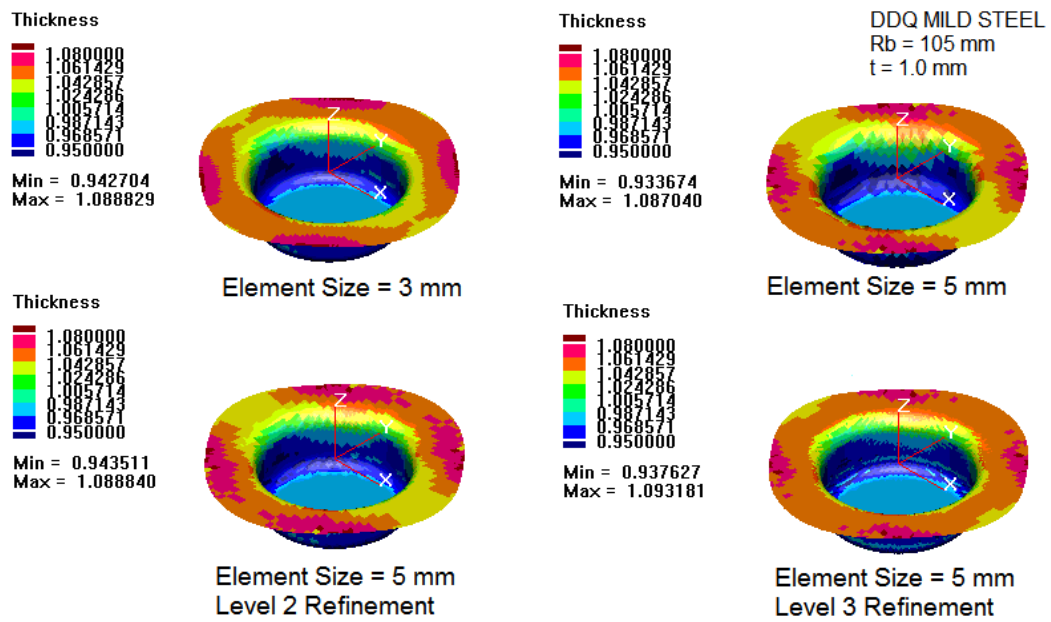


**Figure 5.13 Thickness variations of 3mm, 5mm, 5mm with level 2 Refinement, 5mm with level 3 Refinement Element sizes for 500mm/s Punch Velocity**

The thickness distribution for 3 mm and 5mm with level 2 refinement are very close to each other. Whereas, a relatively coarse mesh, for example, 5 mm element size mesh gives slightly different thickness distribution results. The punch force versus punch progression diagram for 500 mm/s punch speed (Figure 5.14) shows that 5 mm element size results in higher punch forces and 5mm with level 3 Refinement element size results in lower punch forces during the simulation. The difference in 3 mm and 5mm with level 2 refinement is negligible. Refined meshes are defined as mesh size / refinement level. For example; the 5mm with 2 level refinement is defined as “5mm/2Ref”.

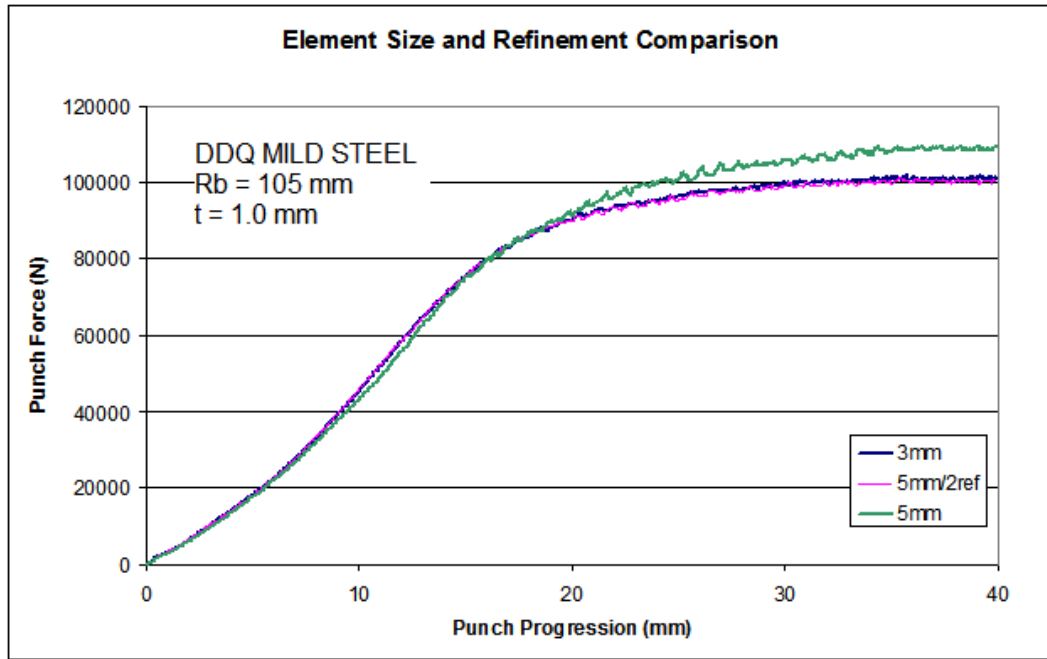


**Figure 5.14 Punch Force vs. Punch Progression curves for different element sizes**

The results for four different element sizes reveal that finer meshes provide similar results as far as thickness distributions and punch force vs. punch progression graphs are concerned. The optimization is about obtaining accurate results in reasonable amount of time. So the comparison of Computational time is investigated and illustrated in Figure 5.15.

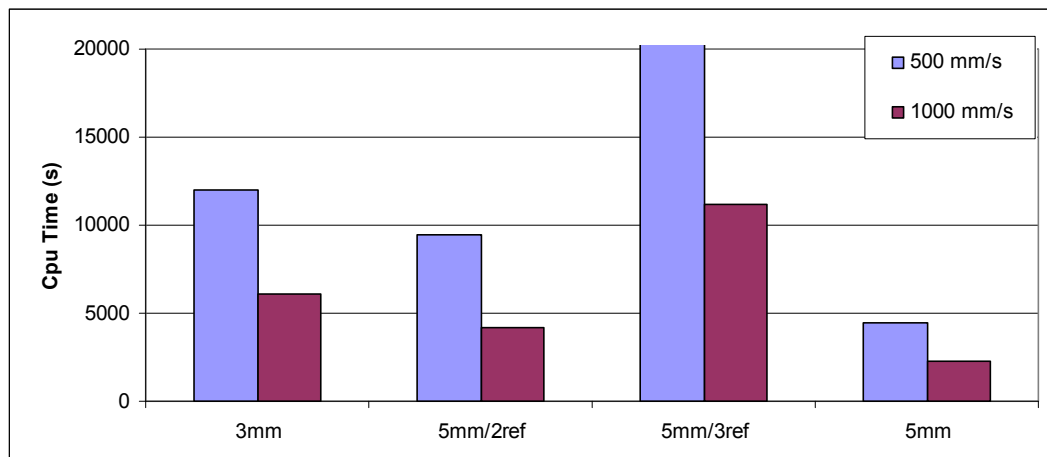


**Figure 5.15 Punch Speed and Element size effect on Computational Time**

As it can be observed from the figure coarse mesh generates results in small amount of time compare to finer meshes. However excessive adaptive meshing, like

5mm/3Ref, increases Computational time. The important point is adding optimum level of adaptive meshing to the simulation, finer results can be obtained in smaller amount of time. 5 mm element sizes are coarse, however by enabling 2 refinement levels to this mesh, accurate and faster results can be obtained.

All these simulations reveal that adaptive meshing is a powerful tool to establish a transition between initial and final elements having different lengths during the simulation, but it should be activated cautiously since unnecessary usage can significantly increase the computational time.

#### **5.2.4 Mesh Topology**

Besides the element size, mesh generation plays a key role in Finite Element Methods. Different applications require different types of meshing. For example, in wrinkling analysis radial meshes are preferred. If radial analysis is performed, then radial mesh is utilized. Tool meshes should be fine in order to avoid penetration problems and obtain accurate results as stated before. Also, in order to avoid contact problems, tool meshing and blank meshing should cover each other.

In PAM-STAMP simulations, quadrilateral element type is utilized. Tool and blank meshing are performed in Marc Mentat and imported to the PAM STAMP. In order to compare mesh topologies, two different meshes are generated and simulations are performed. Radial and uniform meshes are shown in Figure 5.16.

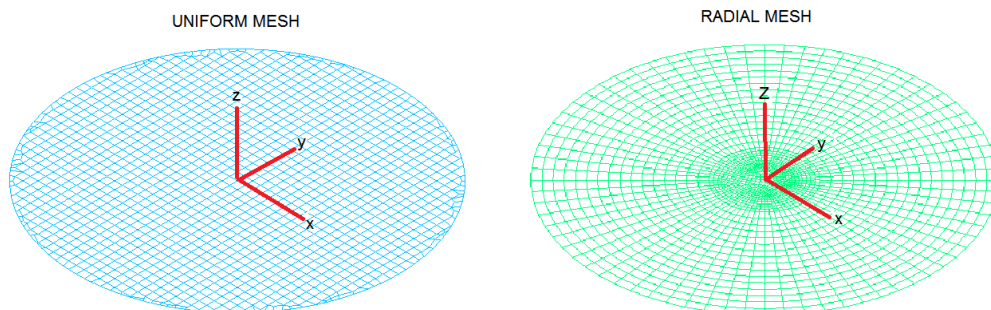


**Figure 5.16 Uniform and Radial Mesh of the blank**

The uniform mesh composes of 1460 elements, 1537 nodes and 3012 edges; however the radial mesh composes of 1945 elements, 1982 nodes and 3926 edges. Comparing these numbers, one easily state that radial mesh is finer.

If the equivalent plastic strains calculated at the mid-plane of the deformable bodies are inspected, it can be concluded that minimum strains and maximum strains are higher for uniform mesh structure compared to radial mesh structure in analysis of NUMISHEET problem (Figure 5.17). Same difference can be obtained when the force - displacement curves are observed (Figure 5.18). Forming force requirements for uniform mesh structure are a little bit higher than for that of radial mesh structure. According to this fact, it can be stated that although the same material properties are used in both simulations, using different mesh topologies may influence the stiffness of the deformable body.

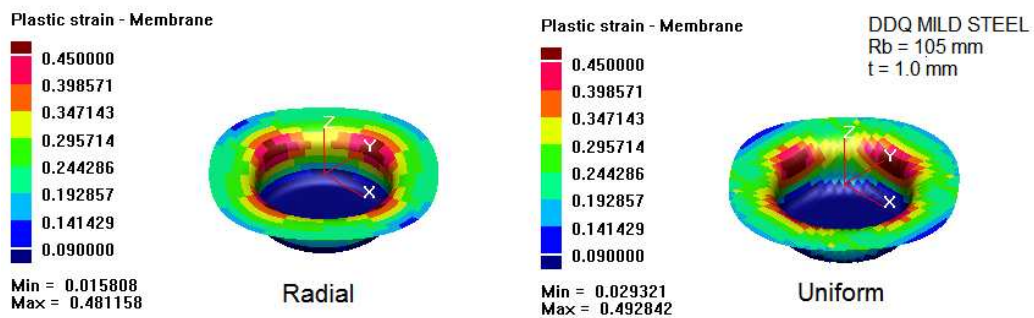


**Figure 5.17 Equivalent plastic strain contours of radial and uniform mesh structures**

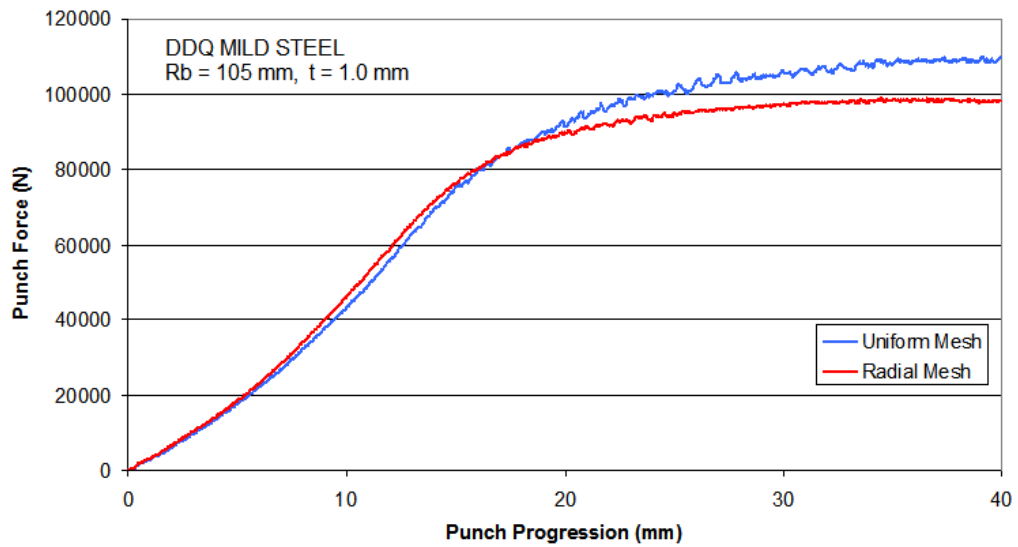


**Figure 5.18 Punch Force vs. Punch Progression curves for Radial and Uniform mesh structures**

For an analysis that targets to investigate the wrinkling phenomenon, radial mesh structure have advantages over uniform mesh structure. The radial mesh enables the user to obtain results in cylindrical coordinate system easily. Also, the blankholder mesh is in radial structure so contact problems are minimized. Another advantage of radial mesh is wrinkling detection and wrinkled part image is better in radial meshes (Figure 5.19).

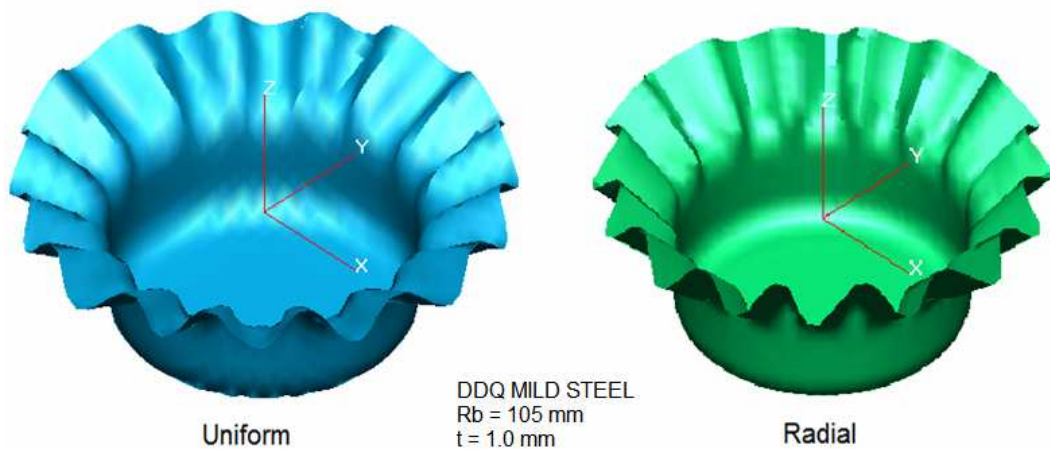


**Figure 5.19 Wrinkled blank with uniform and radial mesh structures**

### ***5.2.5 Comparison with NUMISHEET 2002 Benchmarks***

According to the proposed process parameters at Sections 5.2.2, 5.2.3 and 5.2.4 a cylindrical cup drawing numerical experiment is set up to compare the simulation results with NUMISHEET 2002 Benchmark in order to verify that those parameters are optimum and useful for dynamic-explicit finite element codes.

The process setup and geometry of tools used in the benchmark are already provided in Figure 5.1. In the same setup, steel material with 1 mm thickness is used as the workpiece. The material data for the workpiece is tabulated in Table 5.1 previously. The radius of workpiece is 105 mm. Same geometrical data is used to build the meshes in the simulation. Punch speed is chosen as 500 mm/s and punch stroke is 40 mm. Friction coefficient for all surfaces are stated as 0.0426 by the material supplier. Blank element size is 3 mm and no refinement is applied. The uniform mesh is used.

Twenty-three participants have supplied results to NUMISHEET 2002 benchmark. Seven of them have conducted experiments, (Detailed information about these participants can be found in Appendix A) whereas the rest of them participated with simulation results obtained from different finite element packages.

The comparison between simulation and benchmark is made by inspecting the forming force - displacement curves and outer radii of flange. These comparisons are illustrated in the following figures.

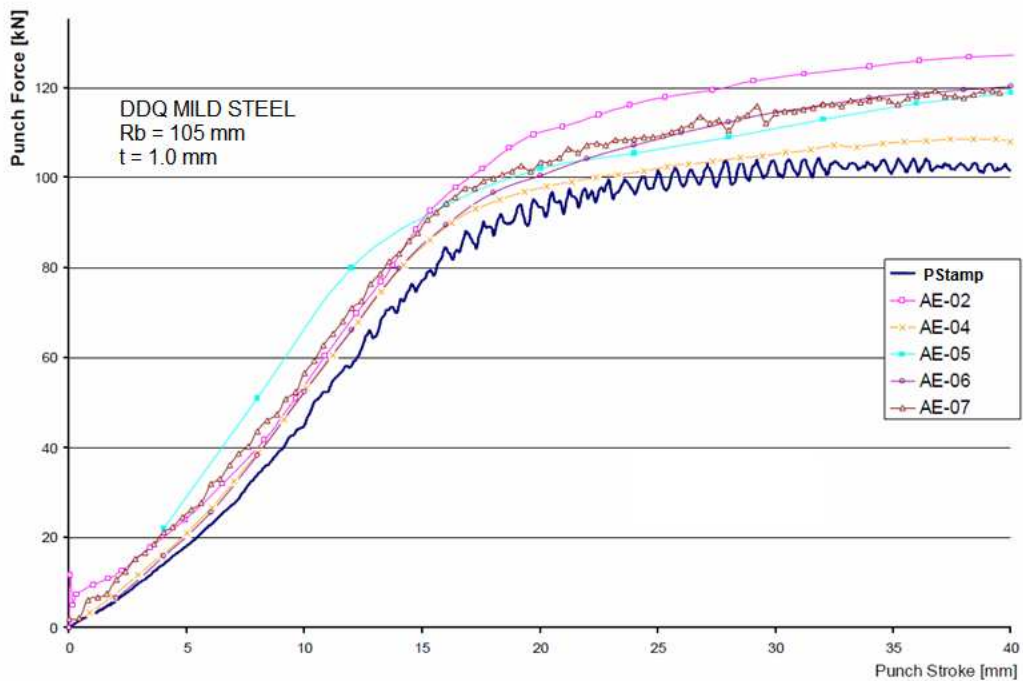


**Figure 5.20 Comparison of Punch Force – Punch Stroke curve of Pam Stamp simulation with Benchmark Experiments**

In Figure 5.20, it can be noticed that the best compliance exists between the simulation result and AE-04. The results supplied by other participants are slightly higher than this agreement; however these differences may exist due to the external influences. For instance, E.H. Atzema (Appendix A) from Corus Research, Development and Technology has stated that the grid applied to the steel blank influenced the friction condition, thus it increased the values in the punch force versus punch displacement graphs by 5 percent. There is a difference of 20 kN in the measured maximum punch forces between the highest and lowest experimental findings in Figure 5.20.

Outer profiles of the flange are compared in Figure 5.21 and 5.22 for steel blank with high blank holder force (HBHF). In Figure 5.21, the outer circumference of flange is plotted in Cartesian coordinates and in Figure 5.22; it is plotted with respect to the  $r$  and  $\theta$  in cylindrical coordinates.

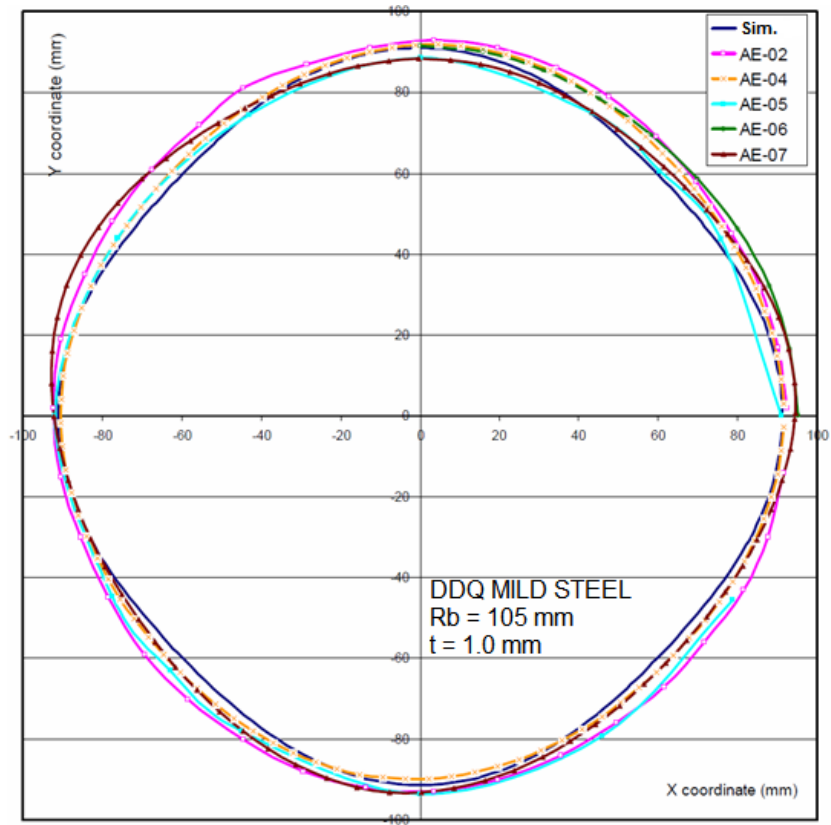


**Figure 5.21 Comparison of outer circumference of steel flanges of Pam Stamp simulation and benchmark experiments**

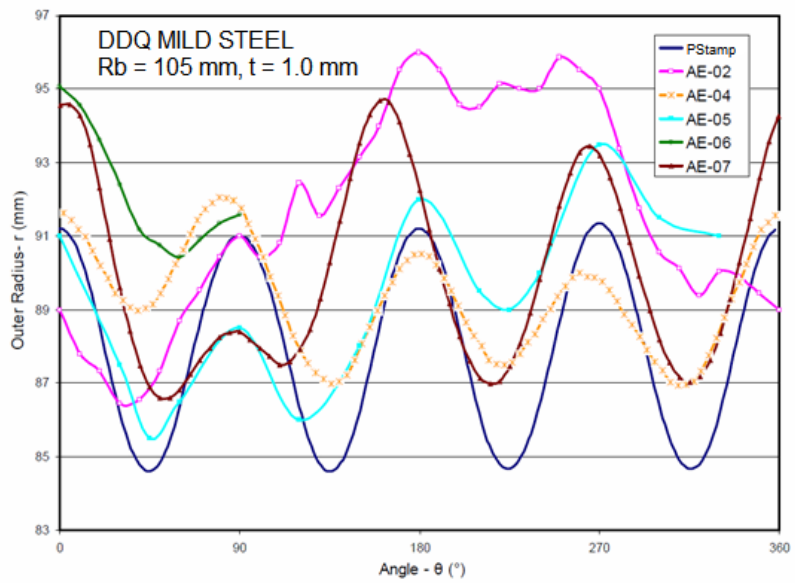


**Figure 5.22 Comparison of outer circumference of steel flanges of Pam Stamp simulation and benchmark experiments**

It is shown that the simulation result only shows some variations from benchmark experiments AE-02 and AE-07 and is compatible with other three experiments. The reason of the variation can be the misalignment of the blank according to the Rolling direction and eccentric placement of blank on the die. In the simulation such incorrect orientations cannot occur since the recent finite element codes have features like “auto-positioning”.

Almost all simulation results of steel material are verified with benchmark experiments. The compliance between the results is not only determined by the general behavior but also satisfied numerically.

### **5.3 Wrinkling Simulations**

This section is dedicated to the wrinkling phenomenon occur during the deep drawing process. Flange wrinkling occurs as a result of compressive forces and it is an undesirable deformation mode. If flange wrinkling occurs during deep drawing process, the flange region plastically buckles into a number of waves and the process fails. However, wrinkling can be prevented by the use of blankholder and drawbead. In the following sections, blankholder and drawbead effects on wrinkling are discussed.

#### ***5.3.1 Blank Holder Simulations***

In this section, PAM STAMP simulations with different blank holder forces are performed and results are discussed. The geometry of the study is again taken from NUMISHEET 2002 Benchmark, see Figure 5.1. The same material (DDQ Steel) is used throughout the wrinkling study. Material properties are listed in Table 5.1. The main objective of this study is to understand the blank holder force effect on wrinkling instability.

As a starting point in wrinkling analysis, zero blank holder force is used. In other words, the simulation is performed without a blank holder. After achieving results

from blank holder free simulations, many simulations are performed with the same process parameters except for the applied blank holder force on the blank is increased.

Throughout the study, in order to comprehend blank holder force effect on wrinkling, different blank holder forces are applied. Figure 5.23 illustrates deep drawn part with zero blank holder force.

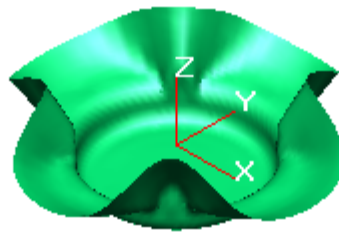


**Figure 5.23 Deep drawn blank without Blank holder**

As it can be seen from the Figure 5.23, four waves are formed on the 20 mm drawn part. In other words, the number of waves formed with zero blank holder force is four. By increasing the BHF, other results than four waves are obtained. The different wave formations for 20 mm punch depth with increased blank holder forces are illustrated in Figure 5.24.

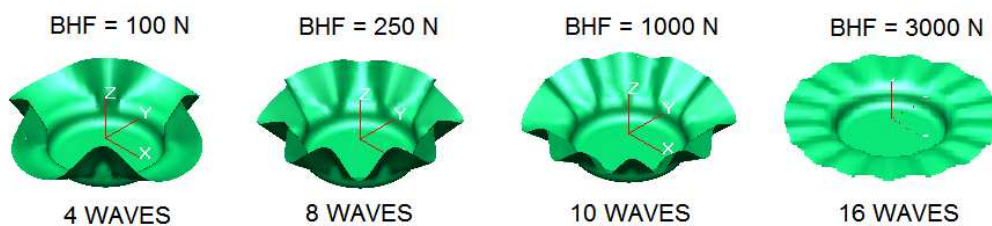


**Figure 5.24 Deep drawn parts with different blank holder forces and corresponding wave formations**

Figure 5.24 reveals that as the blank holder force increases, wave number increases and wave amplitude decreases. The wave amplitude in 100 N BHF case is around 38.3 mm whereas this value is 5.5 mm in 3000 N BHF case. Although the wave amplitude decreases 32.8 mm, the wave number increased to 16 from 4. This effect is

also noted by Kaftanoğlu [9]. In the lights of these simulations, it can be stated that; when a blank holder load is applied to the flange region, wave multiplication occurs because of that constraint. Also, wave peaks are flattened due to the blank holder force. The simulations for 20 mm punch progression are tabulated according to the BHF and corresponding wave number and wave amplitude in Table 5.2.

**Table 5.2 Number and Amplitude of Waves for increasing Blank Holder Forces for 20 mm Draw Depth**

Blank Holder Force	Number of waves	Wave amplitude
1	4	38,387
10	4	38,338
100	4	38,305
250	8	36,701
500	8	36,327
1000	10	30,404
2000	14	9,870
3000	16	5,479
4000	16	2,801

Table 5.2 shows simulation results for 20 mm punch depth. For blank holder forces smaller than 5 kN, severe wrinkling occurs as it can be observed from Figures 5.23-24. These wave amplitudes are getting larger and larger as the punch progress in to the die. In other words, punch depth affects the flange region wrinkle contour. In most cases, wave number does not change and wave amplitude increases with the increasing punch progression.

The punch progression effect on wrinkling is also studied in many simulations. This study also reveals the wave formation during the process. The blank is viewed at 1 mm, 5 mm, 10 mm, 15 mm and 20 mm punch depths. The wrinkling wave formations with the punch progression for different blank holder forces are illustrated in the Figure 5.25.

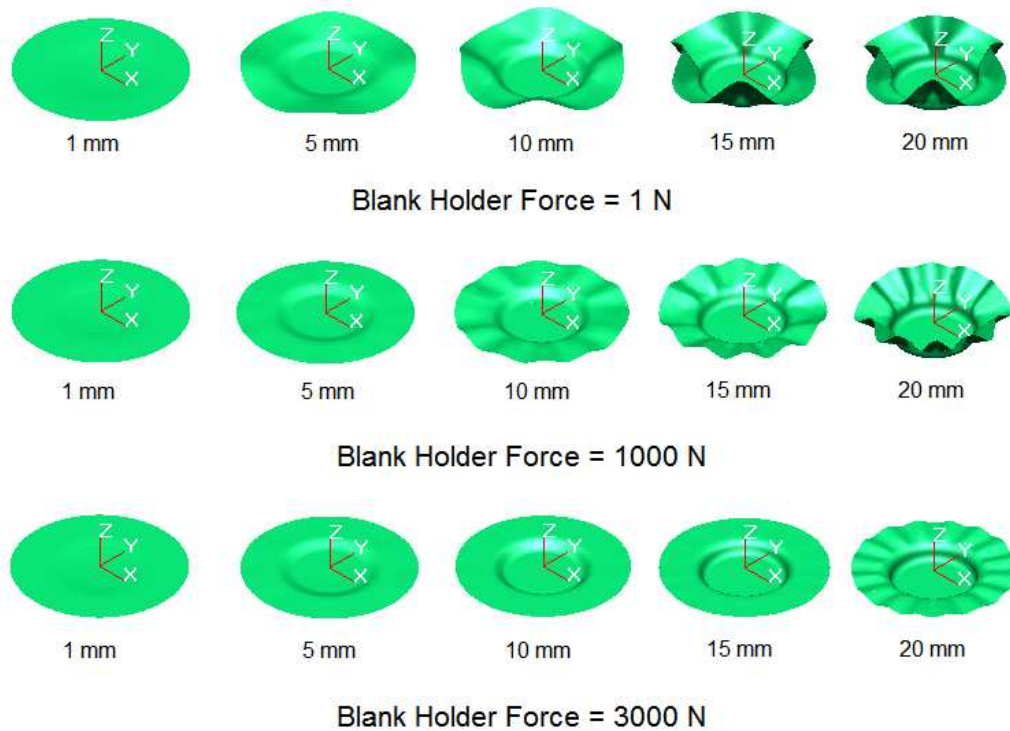


**Figure 5.25 Wave Formations for 1 mm, 5 mm, 10 mm, 15 mm and 20 mm Punch Depths with simulations of 1 N , 1000 N and 3000N Blank Holder Forces**

As it can be seen from Figure 5.25, in 1 N blank holder case, the blank starts wrinkling before 5 mm punch depth and the wave amplitude grows bigger as the punch progress to 20 mm depth. Wrinkling starts around 10 mm for the 1000 N BHF case, in other words, the blank does not wrinkle until 10 mm depth is achieved. The last case shows that 3000 N force applied to the blank hinders the blank from wrinkling up to 15 mm draw depth.

Since, excessive wrinkling and tearing of waves is observed in flange region for higher draw depths, the draw depth is kept at 20 mm for low blank holder forces. In NUMISHEET 2002 Benchmark problem, the draw depth is given as 40 mm. In wrinkling analysis for blank holder forces higher than 3000 N draw depth is set to 40 mm. Simulations are performed for relatively higher blank holder forces. The main objective is to achieve the required blankholder force to avoid wrinkling. Blank holder force is increased up to a point where no waves are seen visually. The simulation results are tabulated in Table 5.3.

**Table 5.3 Number and Amplitude of Waves for increasing Blank Holder Forces for 40 mm Draw Depth**

Blank Holder Force	Number of waves	Wave amplitude
4000	16	22,668
5000	16	20,1956
6000	20	4,991
7000	none	-

Table 5.3 indicates that with 7000 N blank holder force, the flange region does not wrinkle. In order to find the exact blank holder force that is required to avoid wrinkling, further simulations are performed. During these simulations, in order to find the required blankholder force, binary search algorithm is utilized. In this algorithm, the next candidate is selected from the arithmetic average of the maximum and minimum values. So, the first candidate is selected as 6500 N according to the algorithm. The analysis is performed for 6500 N and flange wrinkling is seen. The next candidate is selected as 6750 N and flange is wrinkled again. Flange wrinkling has stopped at 6875 N blank holder force. The study findings are stated in Table 5.4.

**Table 5.4 Number and Amplitude of Waves for finding the required Blank Holder Force for 40 mm Draw Depth**

Blank Holder Force	Number of waves	Wave amplitude
6500	24	3,33499
6750	24	2,44956
6875	none	-

This study aims to find the required blank holder force in order to avoid wrinkling. During the study, a relation between the blank holder force and number of waves formed is discussed. As stated before, the number of waves in the flange region decreases with the increasing blank holder force. The number of waves reaches infinity where there is no wrinkling observed. The required blank holder force restricts these waves to have very little wave amplitudes and as the wave amplitudes decrease, the flange region remains flat, wrinkle free. Figure 5.26 shows

the wave formation for 6500 N, 6750 N and 6875 N blank holder forces. It is noted that no wrinkling is observed for 6875 N blank holder force.

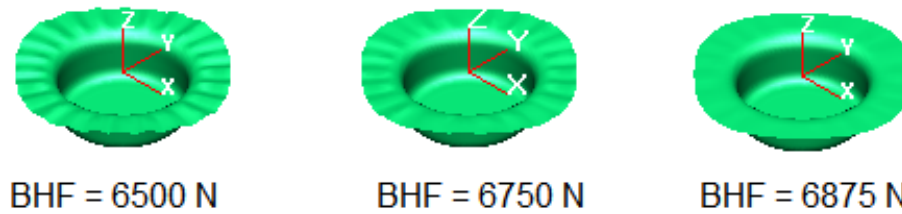


**Figure 5.26 Further analysis images for finding required blankholder force**

Figure 5.26 shows that blank holder force restricts the wave formation and at certain values wave formation in the flange region stops. With 6875 N blank holder force, flange wrinkling is not observed. While concluding this study, the energy graphs of these simulations are searched.

If one investigates the wrinkling problem in case of energy graphs of the process, these graphs show the reason why wrinkling stated as an instability problem in deep drawing. The energy graphs for different blank holder forces, reveal a very important issue about wrinkling. As stated before, the material tends to deform in a mode requiring least energy. In other words, the material tends to wrinkle if the wrinkling energy is lower than the drawing energy. With the increasing blank holder force, wrinkling energy also increases so drawing takes place in the blank. The Figure 5.27 shows energy versus punch progression graph for 5000 N blank holder force.

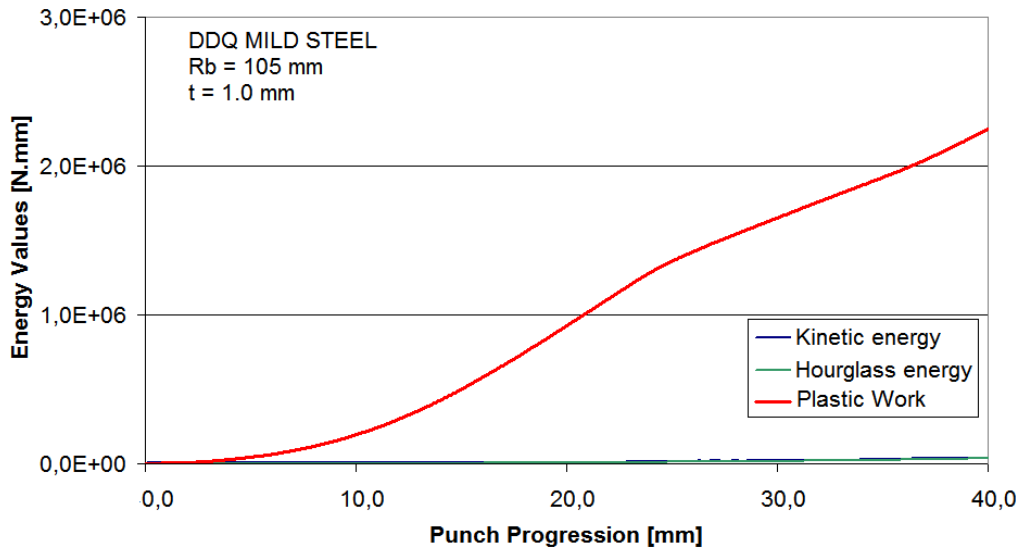


**Figure 5.27 Energy Graphs for 5000 N Blank Holder Force**

In the graph, Kinetic energy and hourglass energy must be small compared to the external work energy. If these values are high, then this means that the numerical error of the simulation is high. But in this analysis, both kinetic energy and the hourglass energy are negligible compared to the external work energy. So the simulation is safe and correct.

The graph in Figure 5.28 reveals an important point about the wrinkling instability. In the previous findings, the blank experiences wrinkling in the flange region for 5000 N blank holder force and the first wave formation for this case takes place around 25 mm punch progression. The external work graph shows exponential behavior up to this point and after 25 mm punch progression, the graph looks like a linear line. This pattern change in the graph suggests that the material deforms in wrinkling mode. This instability point reveals that wrinkling energy is smaller than drawing energy and the blank deforms in a mode that requires least energy. The external energy graph for other blank holder forces are illustrated in Figure 5.28.

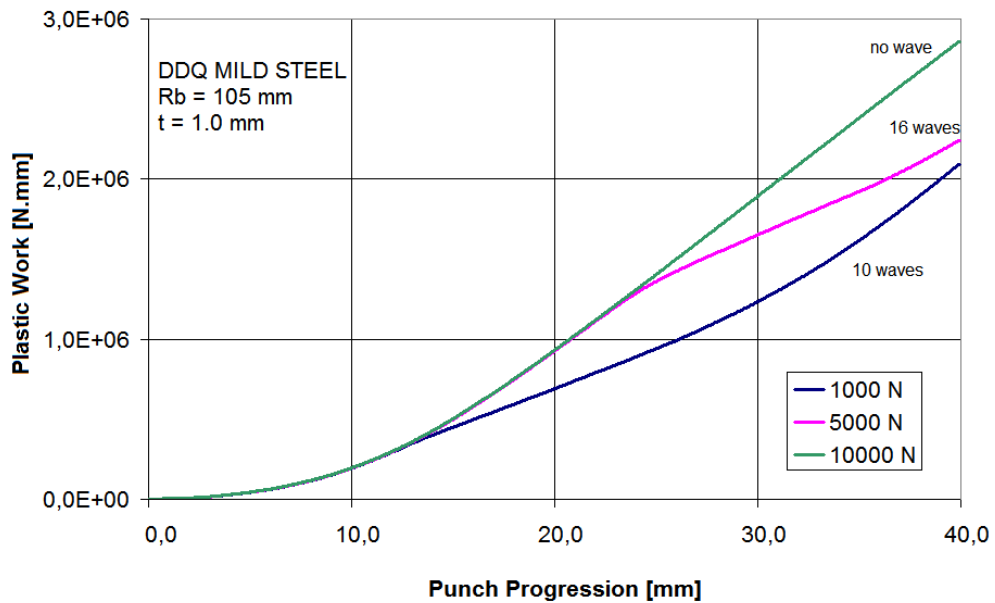


**Figure 5.28 External Energy Graphs versus Punch Progression for 1000 N, 5000 N and 10000 N Blank Holder Forces**

As it can be seen from Figure 5.28, the external energies for the three different blank holder forces are equal up to 12 mm punch progression and then the external energy for the 1000 N BHF case drops. This is the point when the wrinkling energy is smaller than the drawing energy and the first waves are formed in the flange region. The same event can be observed for the 5000 N BHF at around 25 mm punch progression. However the external energy value for the 10000 N BHF case does not drop or experience instability. This means, the 10000 BHF is able to avoid wrinkling in this particular case.

Another important point in wrinkling is the effect of anisotropy. The material is chosen from NUMISHEET 2002 benchmark as stated before. In order to study the effect of anisotropy in wave formation in flange region, these analyses are performed for isotropic material also. All other material properties are taken from the Table 5.1 but material is chosen as isotropic. Figure 5.29 illustrates the effect of anisotropy in wave formation. The simulations are performed for 1000 N blank holder force with 20 mm punch progression.

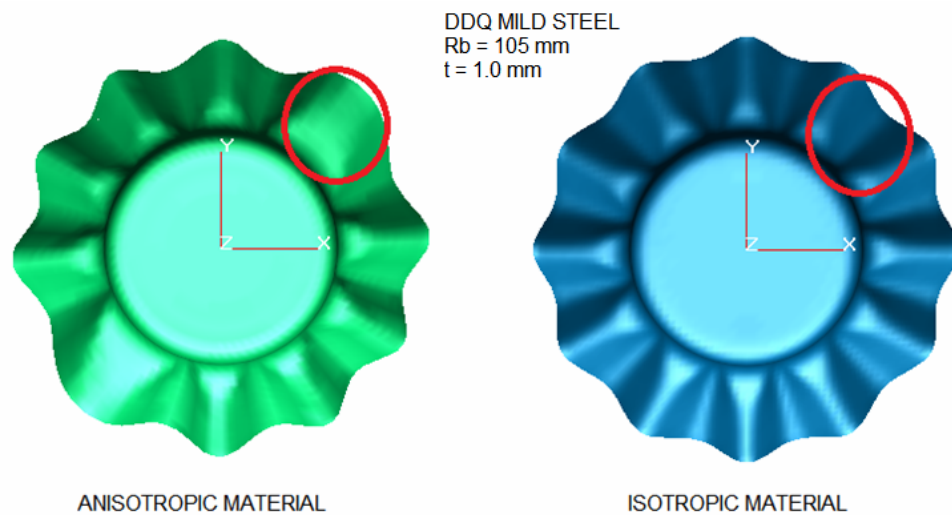


**Figure 5.29 Anisotropic and Isotropic Material wave formations**

Although the applied blank holder forces are the same, the anisotropic material experiences 10 waves, whereas the isotropic has 12 waves as it can be seen from Figure 5.29. Another important point about the wave formation is wave amplitudes and wave shapes which are exactly the same in isotropic material case. Also these waves are symmetric to X and Y planes. On the other hand, the waves formed in the anisotropic material case show differences and they are not symmetrical. In the light of these findings, one can state that quarter or half model finite element tools cannot be used in case of anisotropic material is used. The isotropic model can be solved for quarter or half model. The number of waves for anisotropic and isotropic material is illustrated in the Table 5.5.

Anisotropy effect on wave formations is illustrated in Table 5.5. The isotropic material experiences wave formations that illustrate same amplitude and same shape. This behavior is expected since the isotropic material does not have any change in material properties with the direction. The anisotropic material experiences different wave formations than the isotropic material, can be seen in Table 5.5. In 5000 N blank holder force case, 16 waves are formed for anisotropic material and 20 waves are formed for isotropic material.

**Table 5.5 Number of Waves for Anisotropic and Isotropic Materials**

Blank Holder Force	Number of waves for Anisotropic Material	Number of waves for Isotropic Material
1	4	4
100	4	4
500	8	8
1000	10	12
2000	14	16
3000	16	16
5000	16	20
6000	20	20
6500	24	24

### ***5.3.2 Drawbead Simulations***

In this section, PAM STAMP simulations with different drawbead types are performed and results are discussed. The geometry of the study is again supplied by NUMISHEET 2002 Benchmark but drawbead models are added to the drawing process. Same material (DDQ Steel) is used throughout the drawbead study. Material properties are stated in Table 5.1. The main objective of this study is to understand the drawbead effect on wrinkling instability. Two types of drawbead are used in this study, one is the drawbead module available in PAM STAMP program and the other one is physically designed and utilized drawbead model in the simulations.

There are different drawbead models available in the Pam Stamp program. These models are taken from Stoughton according to the Reference Manual [20] of the program. The suitable drawbead models for the Benchmark problem are illustrated in Figure 5.30.

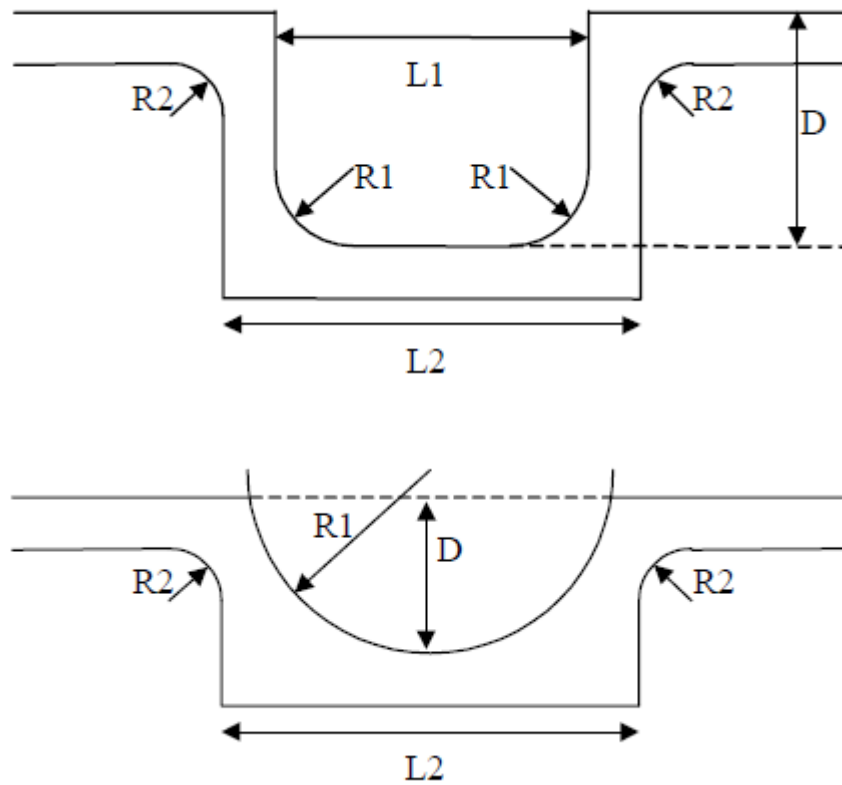


**Figure 5.30 Drawbead models of Pam Stamp [20]**

Among these drawbead models, the spherical model is not suitable for physical modeling due to single point contact so the first one is chosen throughout the drawbead simulations. Although these models represent physical geometries, the program generates two forces from these models and inputs them to the simulation as a restraining and opening force (refer to Figure 5.31). Pam Stamp drawbead module calculates the restraining and the opening forces from the drawbead geometry and the material properties. The drawbead model is replaced by these forces and in the real simulation equivalent drawbead are shown in the Figure 5.32. The drawbead geometry is tabulated in Table 5.6.

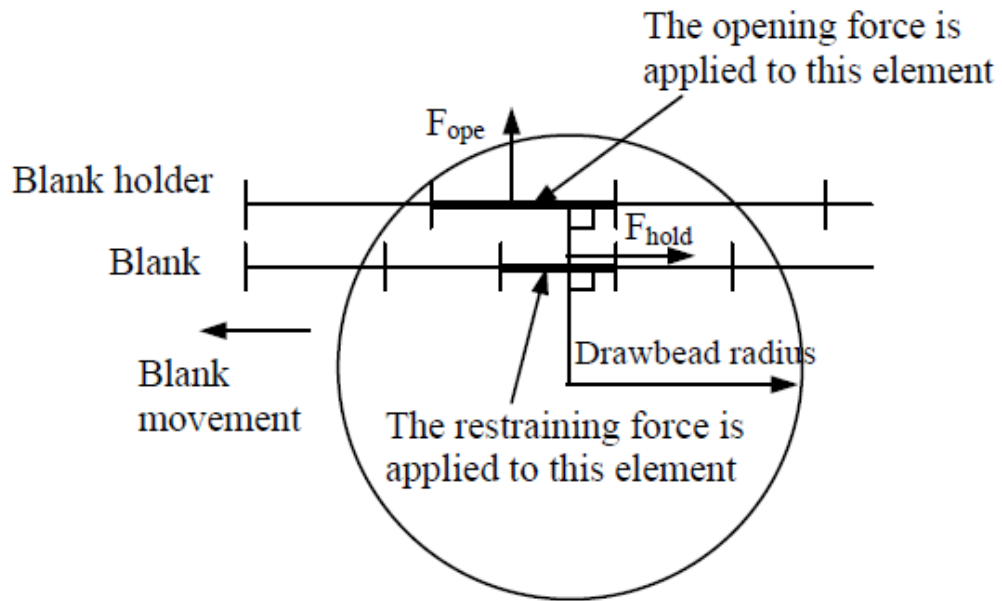


Figure 5.31 Restraining and Opening Force of the Equivalent Drawbead model

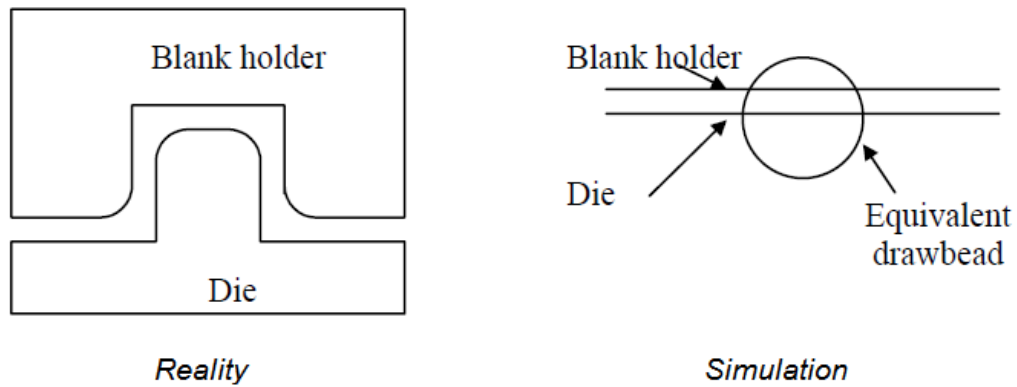


Figure 5.32 Drawbead model in reality and in simulation [20]

Table 5.6 Drawbead geometry parameters

L1	R1	D	L2	R2
4	1.5	1.5	6.5	2

The mesh structure of the blank holder and die is not changed by applying this transformation. This is the main advantage of this drawbead model. Also, this equivalent drawbead is easier to use. The computation time does not change as the

mesh structure remains the same, so as the time step. In addition, the equivalent drawbead model enables fast responses for drawbead geometry changes, since the geometry changes do not affect the mesh structure. Also, different drawbead geometries can be easily implemented to the system and simulated.

The groove depth,  $D$  (refer to Figure 5.30), effect on the deep drawing process is investigated for different depth values. All the other dimensions are kept constant except for groove depth. Figure 5.33 shows thickness distribution for 1.5 mm, 2.0 mm and 2.5 mm groove depths.

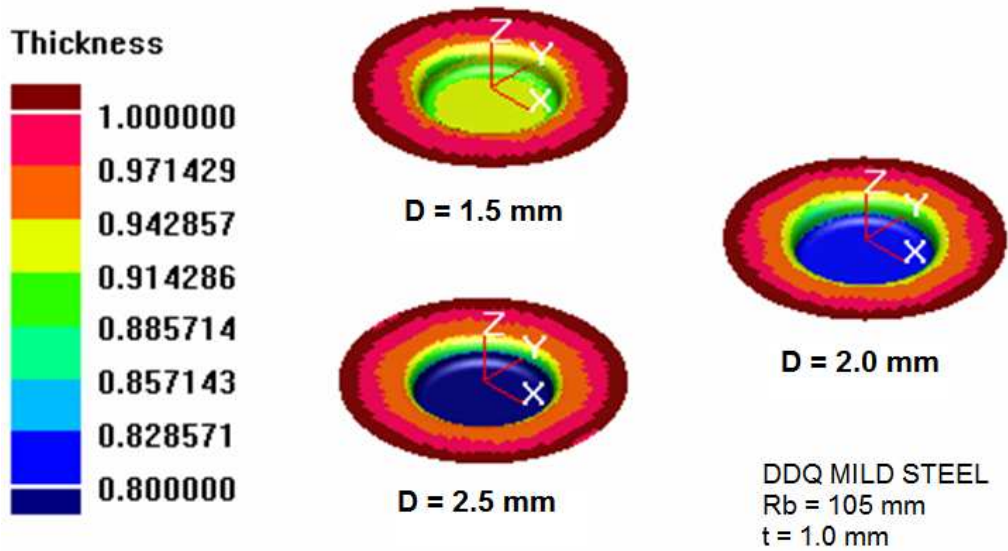


**Figure 5.33 Thickness distributions for 1.5 mm, 2.0 mm and 2.5 mm groove depths at 20 mm punch depth**

The groove depth is very effective in material flow as it can be seen from Figure 5.33. 2.0 mm and 2.5 mm groove depths result in excessive thinning at the bottom of the cup. Thickness of the blank reduces 20 percent for 2.0 mm groove and 40 percent for 2.5 mm groove. The thickness distribution in the flange region is similar for all different groove values. Also, wrinkling is avoided for all these cases.

In order to understand drawbead effect on wrinkling many simulations are performed. Simulations aim to locate the most effective drawbead in avoiding the wrinkling. Three different drawbead radii are studied; the radii of these models are 70mm, 80 mm and 90 mm. The drawbead radii and their positions on the die

blankholder set are shown in Figure 5.34. The drawbead models are represented as purple circles in the simulation. Thickness contours for these drawbead models with 1.5 mm groove depth for 20 mm punch depth is illustrated in Figure 5.35.

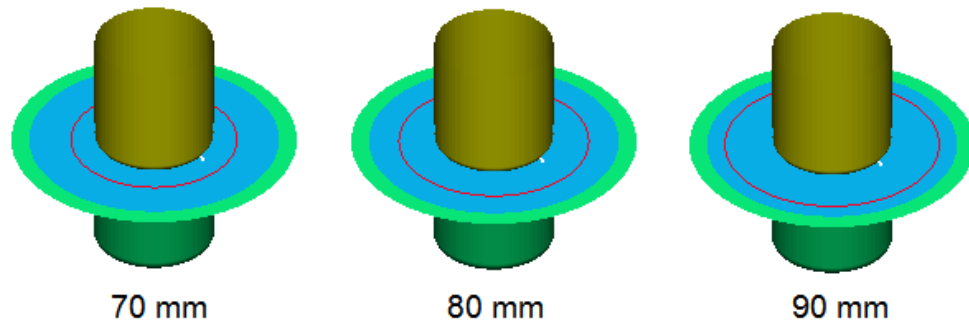


**Figure 5.34 Drawbead models for 70 mm, 80 mm and 90 mm**

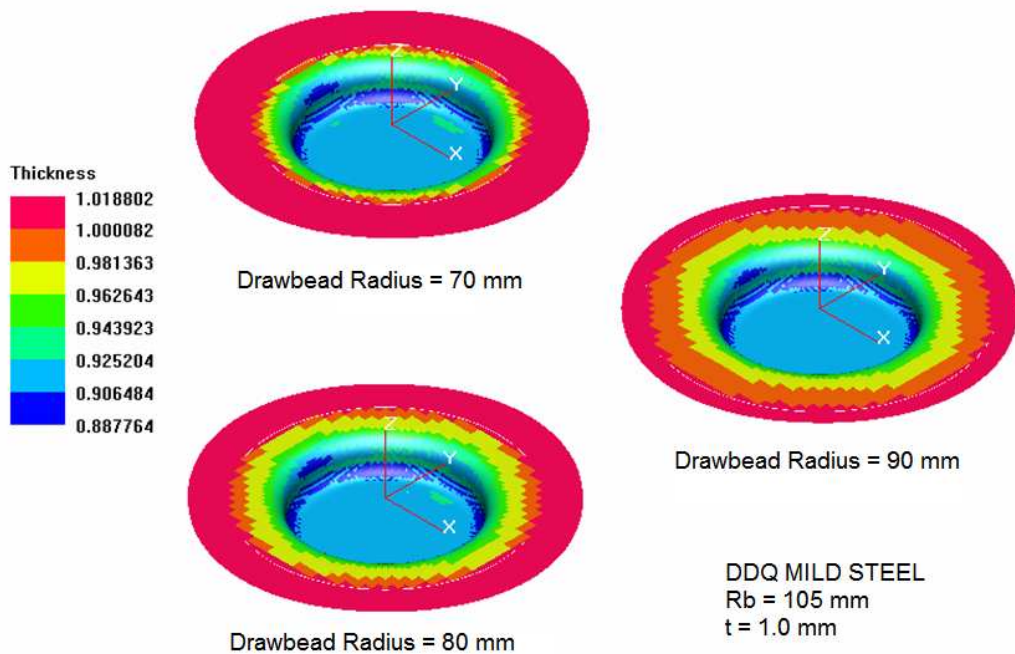


**Figure 5.35 Thickness contours for 70 mm, 80 mm and 90 mm radii drawbeads**

Thickness contours of these different drawbead analyses are very close to each other as it can be derived from Figure 5.35. The thickness values at the bottom of the cups are very similar in magnitude. However, the thickness distribution in the flange region experiences some difference with drawbead size. Flange thickness of the 70 mm radius drawbead model seems to have a uniform distribution. The other

drawbeads do not show this uniform thickness in the flange region. In all drawbead analyses, the flange region between drawbead location and the outer diameter of the blank experiences uniform thickness distribution as it can be seen from Figure 5.35. In order to obtain uniform distribution drawbeads, one shall use 70 mm radius drawbead model, nearest possible drawbead model to the center.

Same drawbead geometries are used in the simulations for these three different drawbead radii. After the further simulations 90 mm model seems to be the least effective, because the drawbead do not cover the blank as it flows into the die. Anisotropy of the material is the main reason that the drawn part deviates from its circular shape as it can be seen from the Figure 5.36.

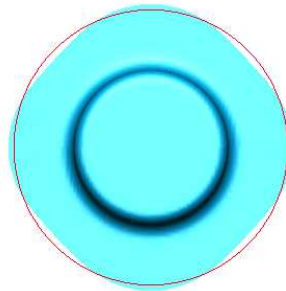


**Figure 5.36 Fully drawn part with 90 mm drawbead**

In simulations, same blank holder forces are used for both drawbead models. While using same blank holder forces, the most important point is to comprehend the effect of opening force, because when the opening force is higher than the blank holder, the wrinkling analysis will be meaningless physically. Opening force increases as the groove depth increases, so the needed blank holder force increases. Figure 5.37 shows that the blank experiences severe wrinkling when opening force beats blank holder force.

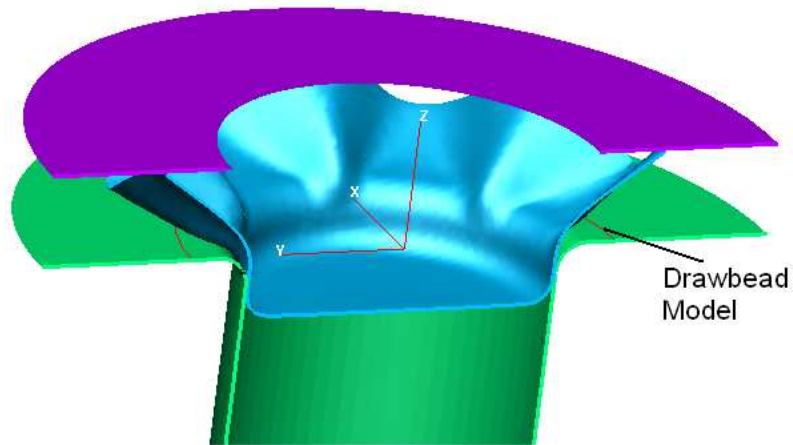


**Figure 5.37 Wrinkled blank due to insufficient blank holder force**

The drawbead study is continued with the physical modeling of the drawbead in the simulation. The meshing of this study is also performed by using Marc Mentat. The blank holder and the die geometries are meshed again with the physical drawbead geometries. The geometry of the drawbead is illustrated in Figure 5.38.

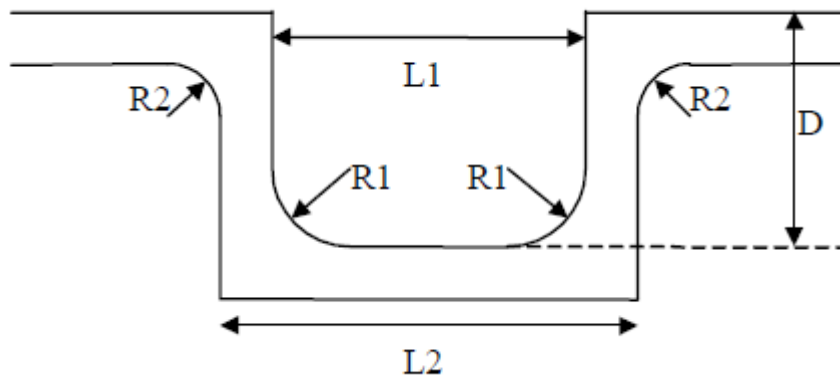


**Figure 5.38 Drawbead Geometry for small and large groove [20]**

Two different geometries are used for small and large grooves. Geometrical properties of both small and large grooves are tabulated in Table 5.7 and all dimensions are given in millimeters. Figure 5.39 illustrates simulation models with these drawbead models.

**Table 5.7 Drawbead Dimensions in millimeters**

Drawbead	L1	R1	D	L2	R2
Small	4	1.5	2.5	6,25	2
Large	8	3	6	10,25	3

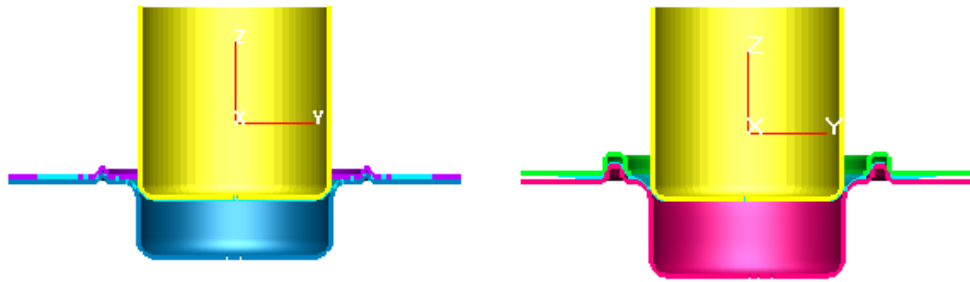


**Figure 5.39 Drawbead added simulation models**

The simulation is divided into two different stages. In the first stage, both blank holder and punch penetrates through the die. The blank holder plate stops at the position when the distance between blank holder and die reaches blank thickness value. After this point only punch penetrates into the die and deep drawing process continues. The simulation results for small and large groove drawbeads for 10 kN BHF case are illustrated in Figure 5.40 and Figure 5.41.

DDQ MILD STEEL  
 $R_b = 105 \text{ mm}$ ,  $t = 1.0 \text{ mm}$

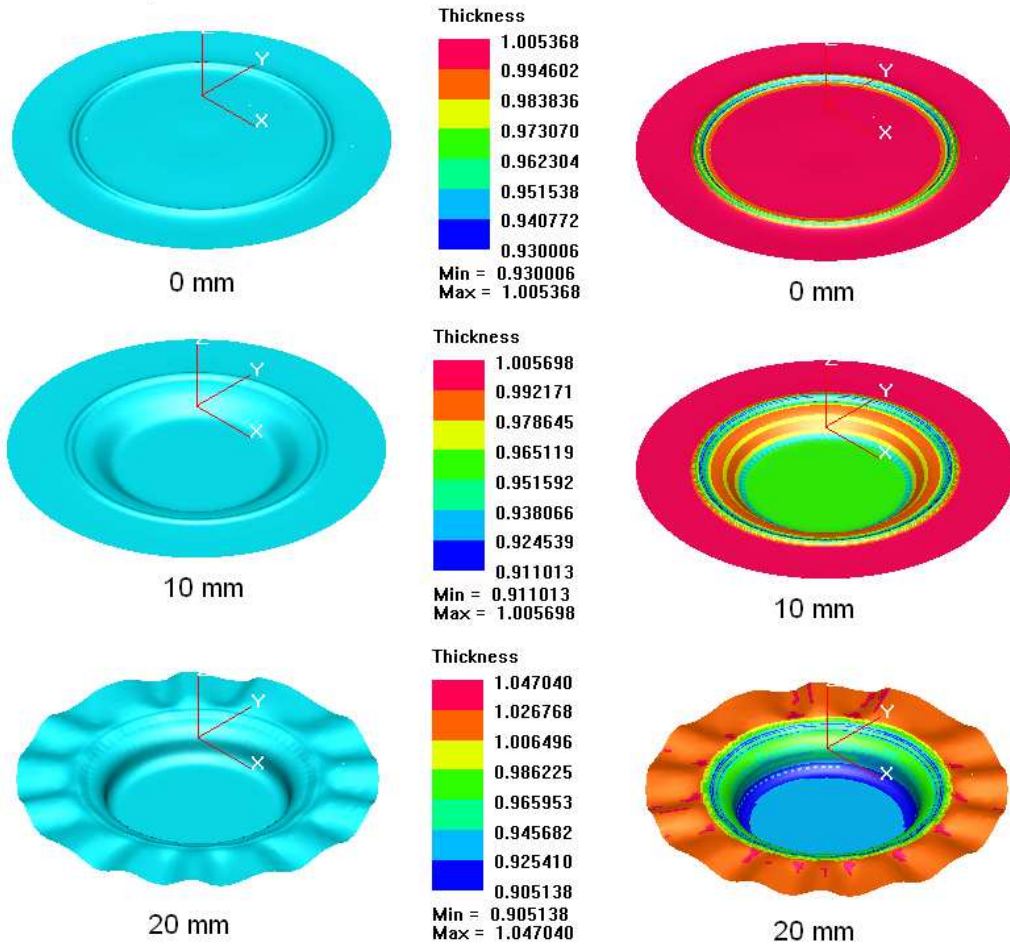


**Figure 5.40 Small drawbead analyses for 10 kN BHF**

In Figure 5.40, the flange region experiences wrinkling at 20 mm punch progression. The applied blank holder load does not prevent wrinkling, so a higher blank holder force should be used. Thickness values at 0 mm indicate that the material is thinned as it is shaped by drawbead model. As the punch progresses into the die, thickness at the bottom of the blank experiences more and more thinning. The thickness values near punch fillet radius are lowest and there may be a possible tearing if punch progresses more. The minimum thickness value is around 0.9 mm and the maximum is around 1.05 mm.

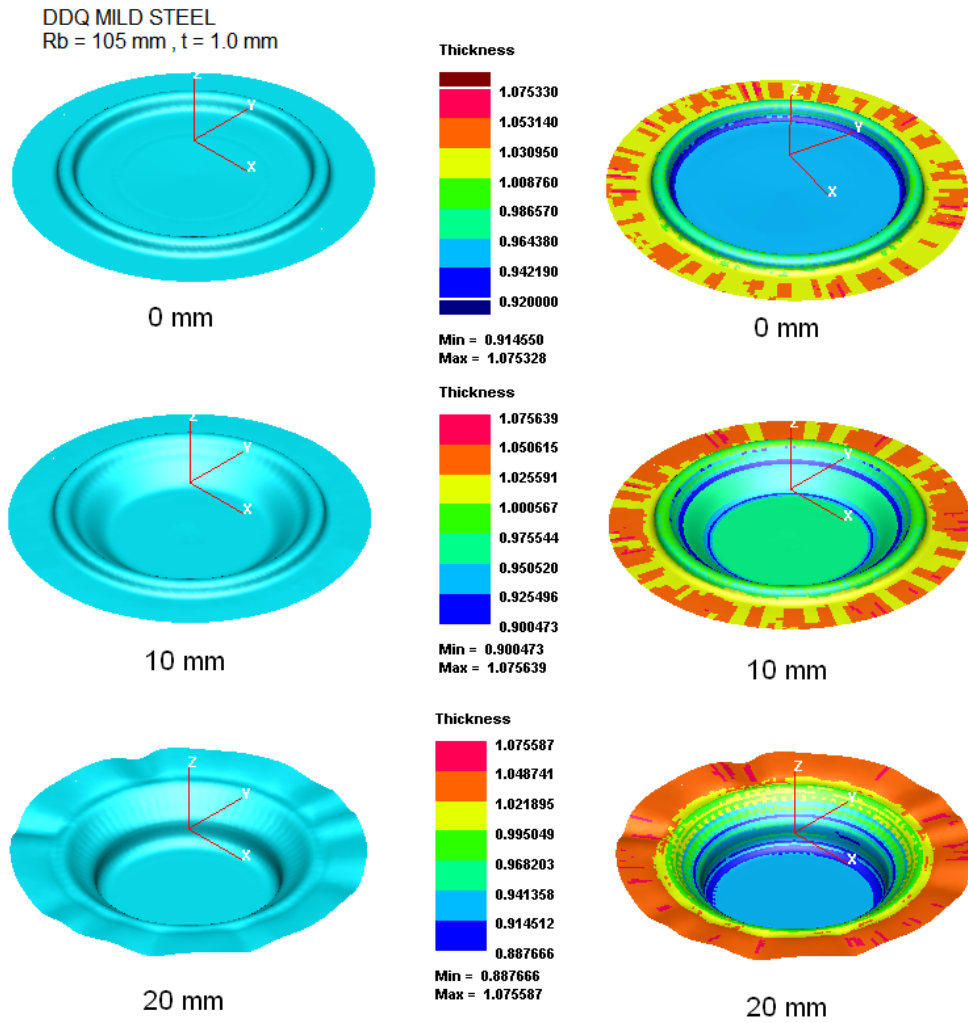


**Figure 5.41 Large drawbead analyses for 10 kN BHF**

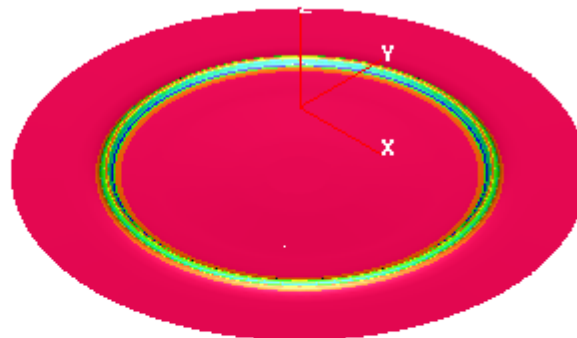
Figure 5.41 shows that the blank experiences wrinkling just similar to small drawbead model. The BHF is not enough to hinder wrinkling. The thickness values at 0 mm punch progression are lower than small drawbead case, which is expected as the groove depth is larger when larger drawbeads are used. The minimum thickness values are around 0.93 mm in small drawbead case whereas it is around 0.91 mm for large drawbead case. The minimum thickness value at 20 mm punch progression is around 0.89 mm, which is lower than the thickness value of small drawbead case. As both small and large drawbead simulations experience wrinkling, higher BHF is used. The simulation results for small and large groove drawbeads for 100 kN BHF case are illustrated in Figure 5.42 and Figure 5.43.

DDQ MILD STEEL  
 $R_b = 105 \text{ mm}$   
 $t = 1.0 \text{ mm}$

Thickness



Min = 0.922428  
 Max = 1.005305

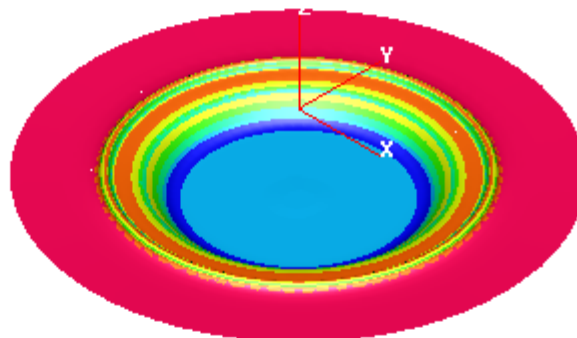


0 mm

Thickness



Min = 0.890161  
 Max = 1.005319

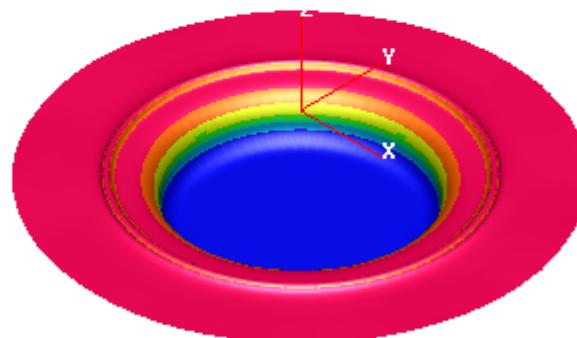


10 mm

Thickness



Min = 0.663865  
 Max = 1.005493



20 mm

Figure 5.42 Small drawbead analyses for 100 kN BHF

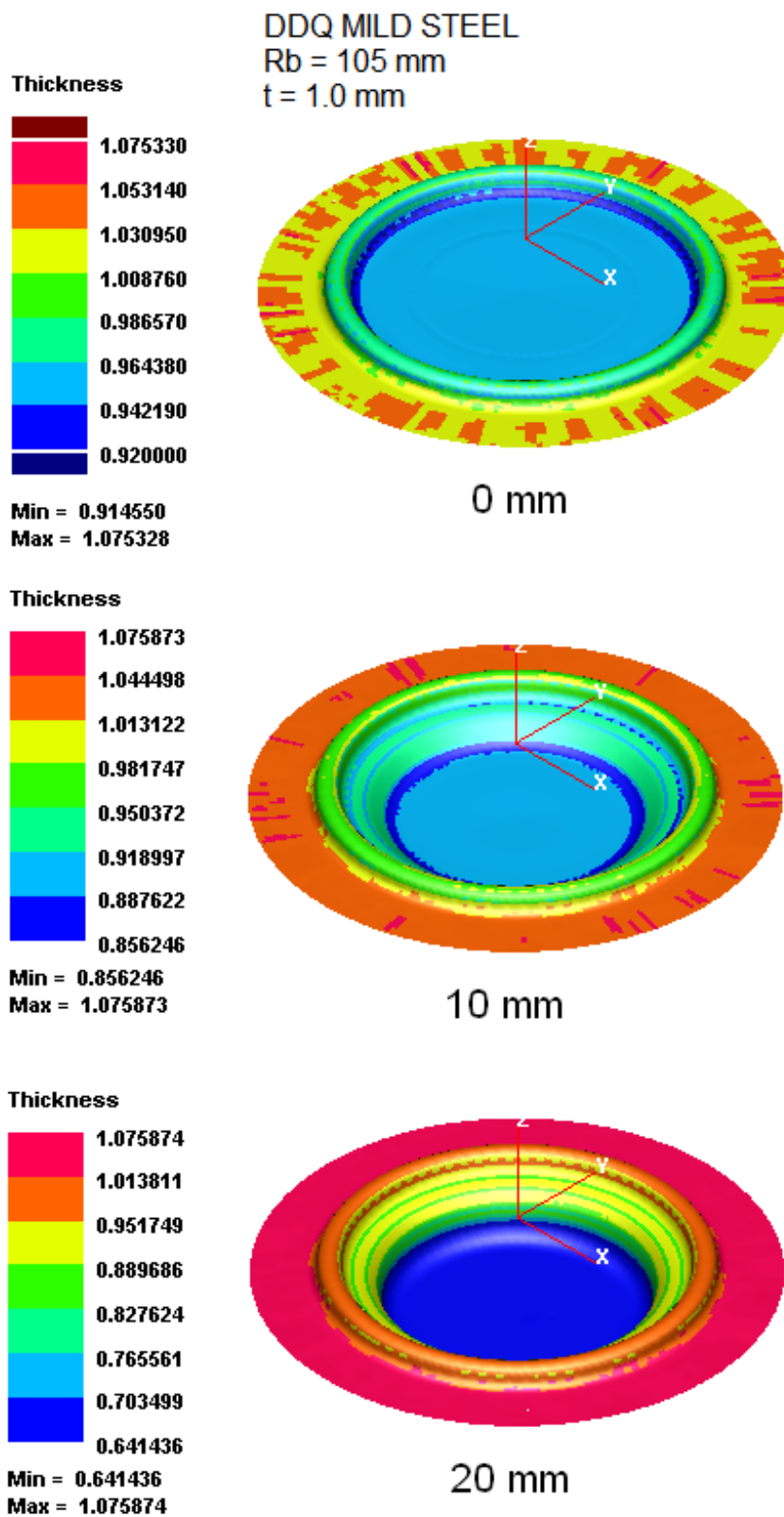
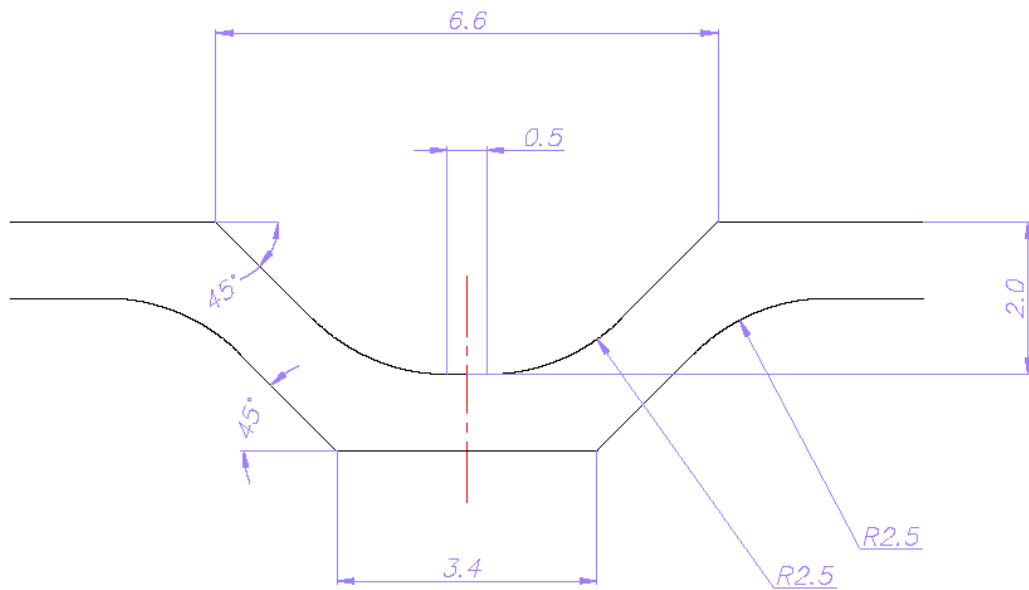


Figure 5.43 Large drawbead analyses for 100 kN BHF

Figure 5.42 and 5.43 indicate that higher blank holder force (100 kN) eliminates the wrinkling problem, however the blank experiences excessive thinning. The blank thickness decreases to 0.66 mm for small drawbead and to 0.64 mm for large drawbead. Wrinkling problem is eliminated, however tearing problem is observed. As the material flow in to the die decreases, more and more thinning is observed. In order to obtain wrinkle and necking free final part, more smooth material flow is utilized by using inclined drawbead model.

The inclined model is designed in order to enable more material flow into the die. The inclined drawbead model dimensions are given in Figure 5.44. In the small and large groove models, the material flow into the die is poor and this yields to tearing at the bottom of the drawn part. The inclined drawbead model aims to achieve good material flow and less thinning in the blank, the results are satisfactory as can be seen from Figure 5.45.



**Figure 5.44 Inclined drawbead dimensions**

DDQ MILD STEEL

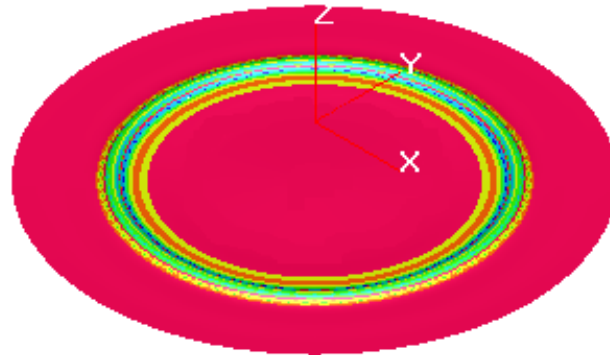
Rb = 105 mm

t = 1.0 mm

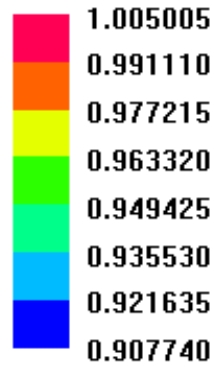
Thickness



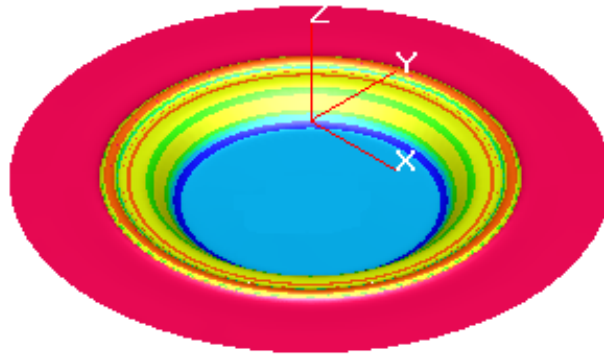
Min = 0.976513  
Max = 1.002155



Thickness



Min = 0.907740  
Max = 1.005005



Thickness



Min = 0.786985  
Max = 1.013420

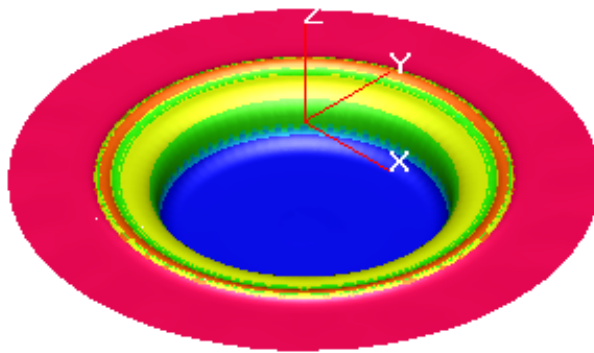
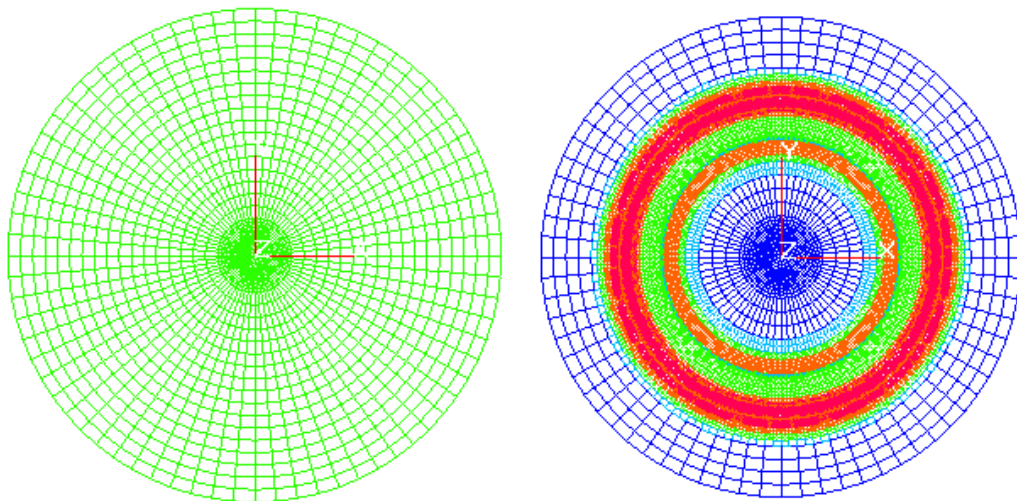


Figure 5.45 Thickness contours for inclined drawbead model with 100 kN BHF

Figure 5.45 shows that the blank does not wrinkle in the flange region, similar to previous drawbead models. The blank thickness at the bottom region is around 0.79 mm that indicates the blank experiences less thinning than the other drawbead models. The material flow for inclined model is smoother and easier as expected.

The physical modeling of the drawbead is very difficult and time consuming. The first problem is encountered in meshing. The drawbead size is very small compared to the blank size. Small size drawbead results in small sized elements in contact region of the blank and drawbead model. So, in order to obtain good contact region; level 5 (highest level available in the program) adaptive meshing is used in simulations. This excessive refinement results in a very sharp increase in computation time. The mesh structure before and after the simulation is illustrated in Figure 5.46.



**Figure 5.46 Mesh structure before and after the simulation**

Energy graphs of the drawbead simulations are illustrated in Figure 5.47. Small, large and inclined drawbead models result in different punch progression vs. external work diagrams. The inclined model energy is higher than the other two drawbead models.

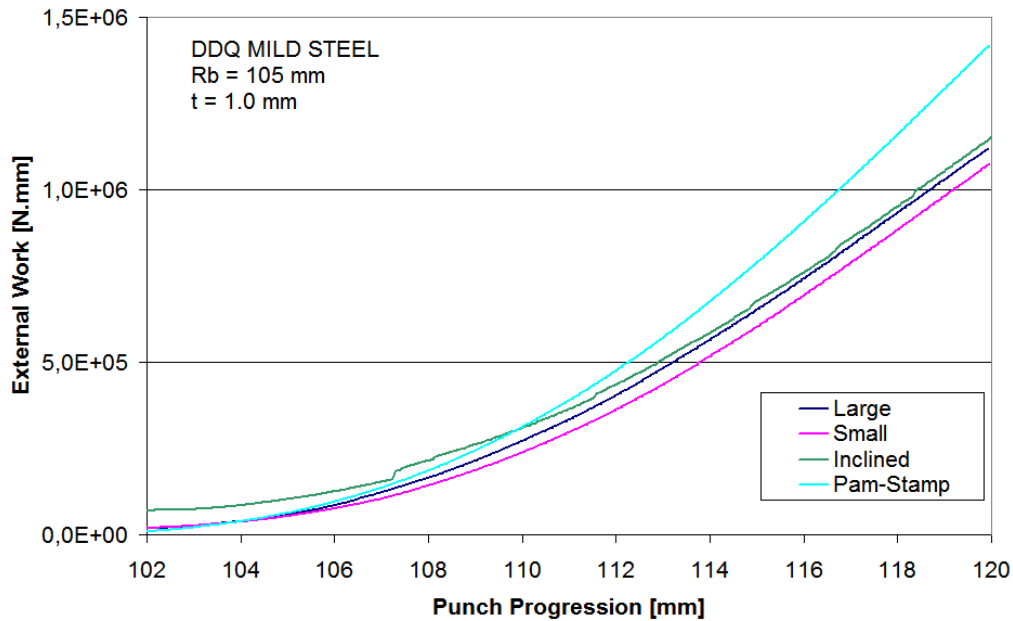


**Figure 5.47 External energy diagrams for different drawbead models**

## 5.4 Experimental Study

This section is dedicated to the experimental study performed. The aim of this study is to understand the effect of thickness in wrinkling problem. In order to study thickness effect, four different sheets with the same material, AL 1050, are used. The thickness values for this experiment are chosen as 0.5 mm, 1.0 mm, 1.2 mm and 2.0 mm. In order to obtain the material properties for these four set of materials, tension test is performed. After obtaining the material properties, deep drawing experiment is conducted. The wrinkling behavior for different thicknesses is studied and the finite element modeling of the experiment is performed. The simulation and the experimental findings are compared.

### 5.4.1 Tension Test

There are four sheet blanks used in this study. In order to find the material properties, tension tests are conducted. The required material properties are found by conducting tension tests at Metal Forming Centre of Excellence in Atılım University.

The experiment specimens are prepared and the test is conducted for four different thicknesses of Al 1050. For one set of tests, 9 specimens are prepared, a total of 36 specimens are used in the experiment. In order to find anisotropy constants, the specimens are cut according to the rolling directions of the sheet material. For one test in 0, 45 and 90 degrees according to the rolling direction, 3 specimens are subjected to tension and the results are obtained. These results are processed by the software available in the test setup and the material properties are calculated accordingly. The test setup is illustrated in Figure 5.48. The test specimens before and after the tension test are shown in Figure 5.49.

During the tension test, all data are obtained and processed in the available software program of the Zwick Test setup. The tension test is performed according to the ISO 10113,05/1991 and ISO 10275,02/1993. These standards cover tensile tests on metals with determination of the vertical anisotropy and the hardening exponents. The tension test results are illustrated in Table 5.8.

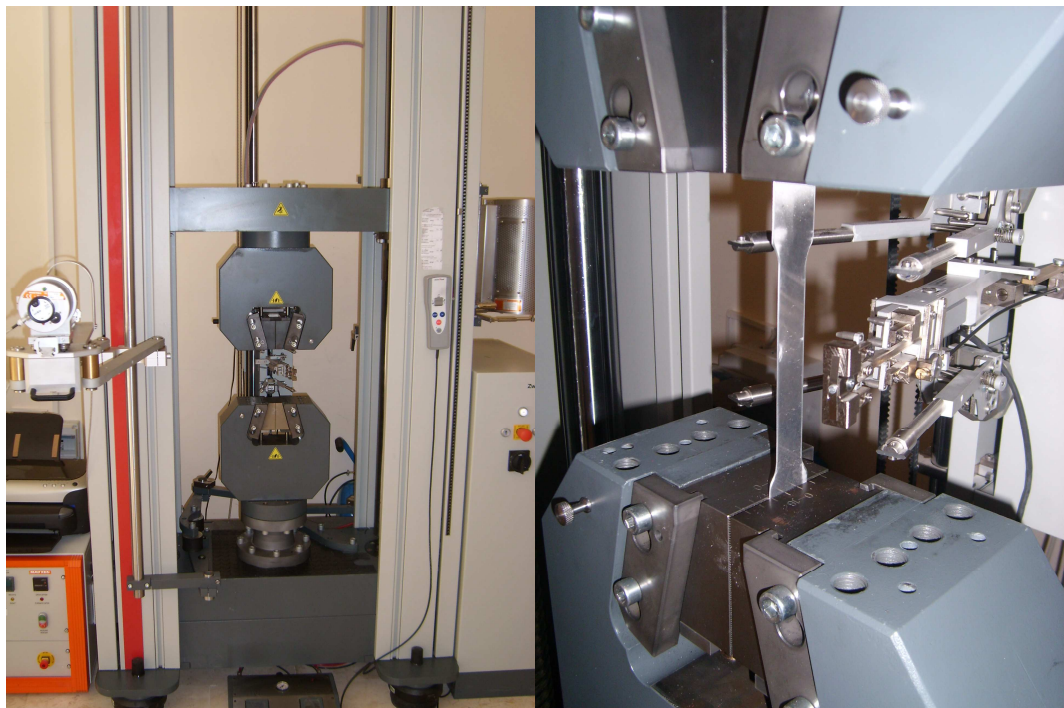


**Figure 5.48 Universal Tensile Testing Machine with 30 ton force capacity (Zwick)**



**Figure 5.49 Tension Test specimens, 2 mm thickness, before and after the test**

**Table 5.8 Material Properties of AL 1050 Material for four thickness values**

Material	E (GPa)	$\rho$ (g/cm <sup>3</sup> )	$\nu$	K (MPa)	n	R (0°)	R (45°)	R (90°)
Al 1050 0.5 mm	59,133	2,7	0,33	99,847	0,1196	0,637	0,496	0,578
Al 1050 1.0 mm	59,766	2,7	0,33	140,86	0,0872	0,896	0,611	0,660
Al 1050 1.2 mm	58,888	2,7	0,33	162,33	0,0963	0,652	0,751	0,684
Al 1050 2.0 mm	57,944	2,7	0,33	286,28	0,0976	0,681	0,833	0,803

### ***5.4.2 Conventional Deep Drawing Experiment***

There are three different sizes of sheet blanks with four different thicknesses are used in this study. The diameters of the blanks are 80mm, 90mm and 100mm. In order to understand the thickness effect on wrinkling, conventional deep drawing experiments are conducted. These experiments are conducted at Metal Forming Laboratory of METU. In the experiments Tinius Olsen Testing Machine is used. This testing setup has lots of deep drawing tools available. From these tools, the most applicable punch and die set is selected. The punch diameter is chosen as 50 mm and the die diameter is 54 mm. The fillet radii of punch and die are 5 mm. During the experiment, 0.5 mm, 1.0 mm, 1.2 mm and 2.0 mm thickness sheets are used. Grease is used as a lubricant throughout the experiment. Average coulomb friction coefficient at all contact surfaces are assumed as 0.08. The friction coefficient value is taken from the previous work of Kaftanoğlu [9]. In order to obtain zero blank

holder force, four nuts are placed around the blank between the die and blank holder. Without blankholder force, the wrinkling in the flange region takes place freely. At first steps, free wrinkling is observed but when the wave amplitudes become higher than the nut height due to increased punch depth, blank holder force is applied to the blank. Tinius Olsen testing machine is illustrated in Figure 5.50. The specifications of the testing machine are given in Appendix B.



**Figure 5.50 Tinius Olsen Tesing Machine**

The deep drawn parts with different thickness values and different diameter sizes are illustrated in Figure 5.51.

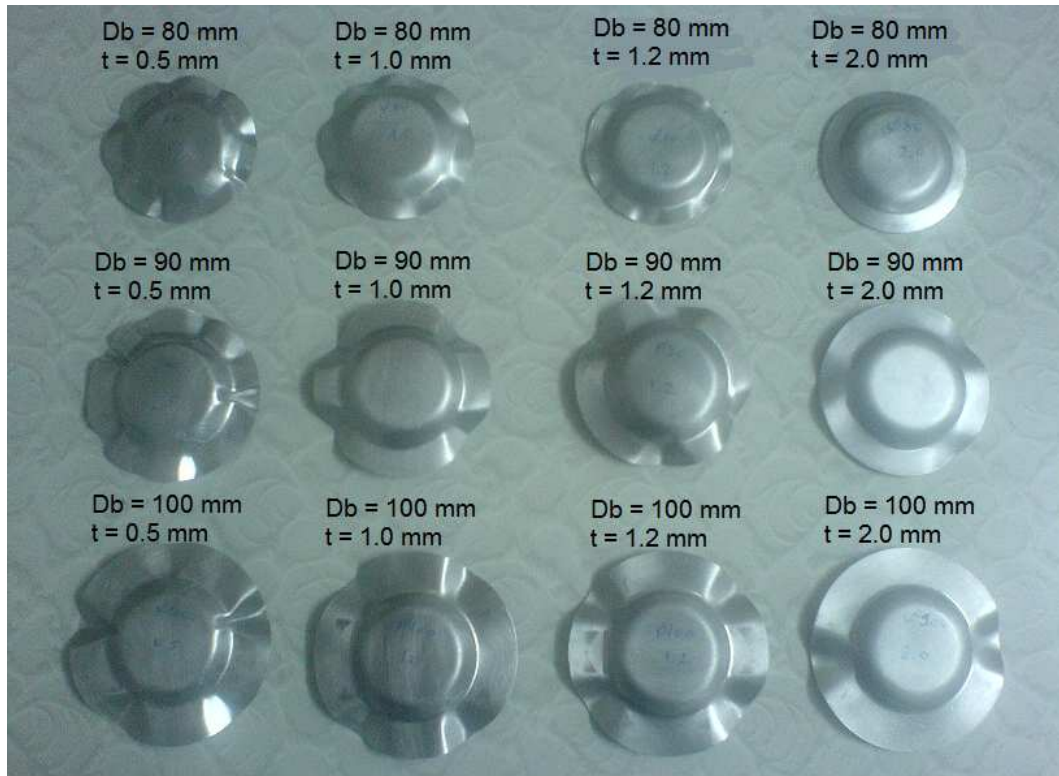


**Figure 5.51 Deep Drawn parts with different thickness and different diameters**

In Figure 5.51, all of the test specimens are illustrated. The wrinkle wave formations show significant differences for different thickness values. The diameter for the first specimen set is chosen as 80 mm. The thickness effect on the wrinkle formation for 80 mm diameter set can be seen in Figure 5.52.



**Figure 5.52 Wrinkling formations for 80 mm diameter blanks**

It can be seen clearly from Figure 5.52 that, the wave number decreases as the thickness of the blank increases. 0.5 mm thick part experiences 8 waves with high wave amplitudes but the 2.0 mm thick part does not wrinkle. Figure 5.53 shows the wrinkling formations for 100 mm diameter blanks.



**Figure 5.53 Wrinkling formations for 100 mm diameter blanks**

Similarly for the 100 mm blank, the wave number decreases as the thickness of the blank increases. 0.5 mm thick part experiences 5 waves with high wave amplitudes but the 2.0 mm thick part have 2 shallow waves.

In order to verify the simulation results of PAM STAMP program, this experiment is simulated and the results are compared. The simulations are performed according to the material properties obtained in Tension tests. The experimental setup is modeled and the blanks with different sizes and thicknesses are meshed. The process parameters are obtained from the conventional deep drawing experiment. The punch progression values for each diameter sets are different in the experiment. Therefore, in the simulation highest value is selected and the process is divided into many steps. By doing this kind of regulations in the simulations, one can obtain the wave formation progress with respect to the punch progression. The experimental setup, modeled in PAM STAMP, is illustrated in Figure 5.54 and the deep drawn part in experiment and simulation is shown in Figure 5.55.

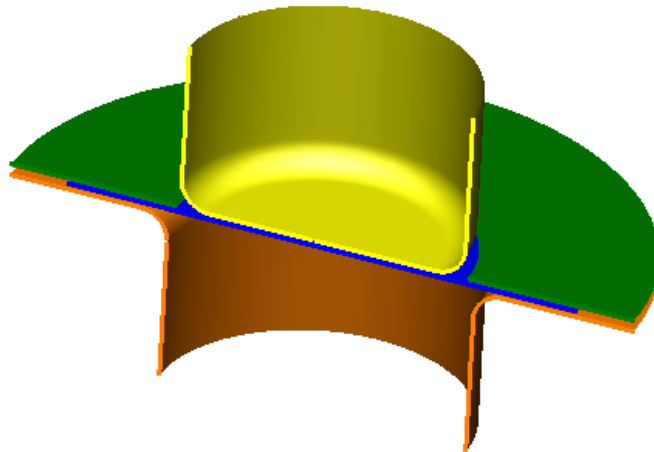


**Figure 5.54 Finite Element Model of the experiment tools**

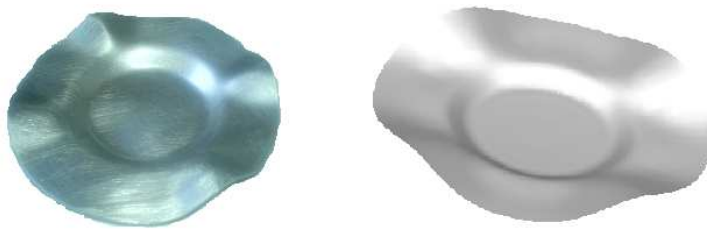


**Figure 5.55 Experimented and Simulated deep drawn part**

Simulation results for 80 mm, 90 mm and 100 mm diameter blanks are illustrated in Figure 5.56, 5.57 and 5.58, respectively. In these simulations, blank holder force is set to 0 N. Table 5.9 summarizes experiment and simulation results.

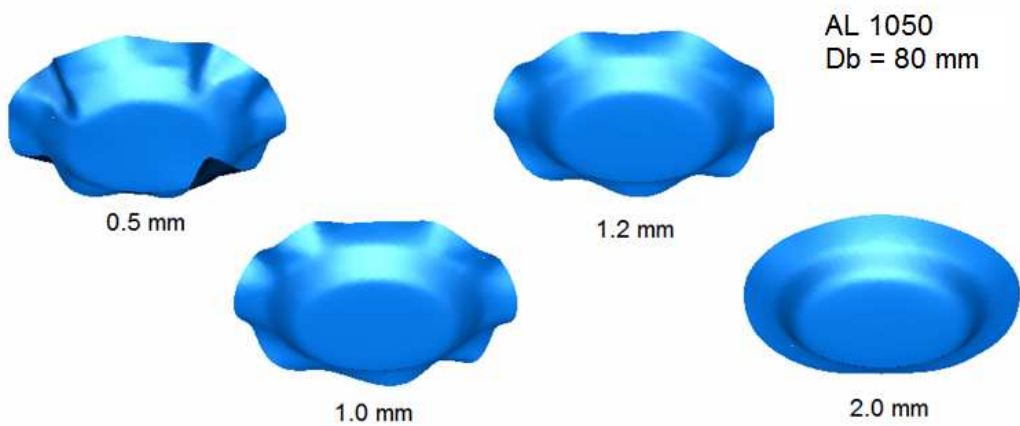


**Figure 5.56 Wrinkling formations for 80 mm diameter blanks**

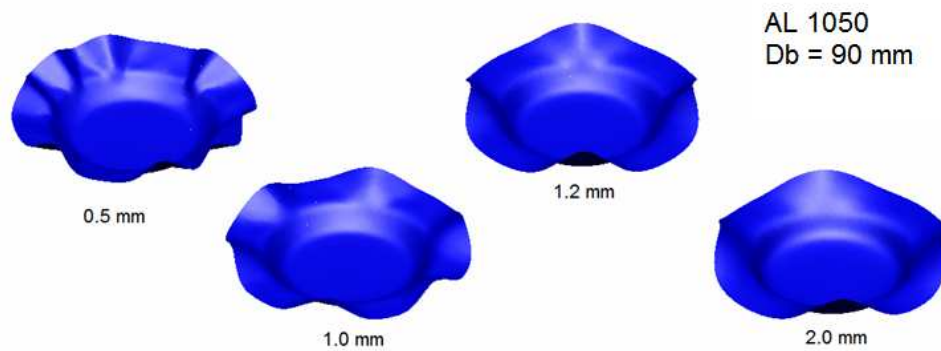


**Figure 5.57 Wrinkling formations for 90 mm diameter blanks**

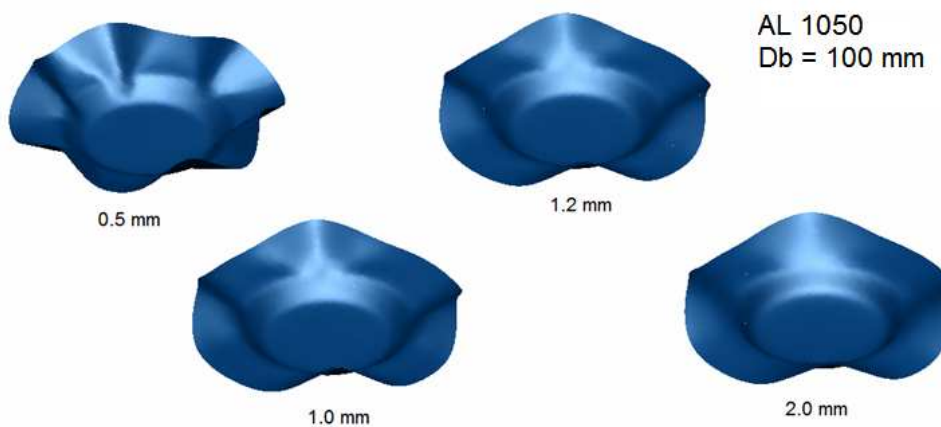


**Figure 5.58 Wrinkling formations for 100 mm diameter blanks**

**Table 5.9 Experiment and Simulation results for specified blank diameters with different thicknesses**

Blank Diameter	Experiment Results				Simulation Results			
	Number of Wave				Number of Wave			
	0.5	1.0	1.2	2.0	0.5	1.0	1.2	2.0
80 mm	10	8	8	-	8-10	8	8	-
90 mm	8	4	4	4	8	6	4	4
100 mm	5-7	4	4	2	6	4	4	4

Experiment and simulation results are in good correlation with each other. Results also indicate that wrinkling is a more serious problem for thinner materials. Thinner materials have higher tendencies to plastic wrinkling.

## CHAPTER 6

### DISCUSSION

In this study, a commercial dynamic – explicit finite element program PAM STAMP is used in order to analyze the wrinkling behavior in deep drawing processes. The NUMISHEET 2002 benchmark problem is selected to verify the finite element program reliability. The process parameters of the program are inspected thoroughly in order to complete an optimization analysis.

The effect of punch velocity on simulation is inspected by trying various punch velocities, a wide range from 50 mm/s to 50000 mm/s. These effects are compared according to the accuracy of the results and the computational time. According to these analyses, computational time increases so much for punch speeds lower than 250 mm/s and the accuracy of the results are not satisfying for punch speeds higher than 10000 mm/s, see Figure 5.6 and Figure 5.7. The other process parameters are element size and refinement. From these analyses, the mesh must be fine in order to obtain reliable results. The refinement is a powerful tool that enables the mesh to be finer wherever necessary and optimum refinement enhances the mesh quality without increasing computational time. Thickness distribution graph (Figure 5.13) indicates that thickness variations, maximum and minimum thicknesses are very close, almost same, for 3 mm element size and 5 mm element size with 2 refinement levels. Simulations for 500 mm/s punch velocity (Figure 5.15) indicates that computational time for 3 mm element size is around 3 hours and for 5 mm element size with 2 refinement level is around 2.5 hours. Another important parameter is mesh topology. Figure 5.17 illustrates that, minimum strains are obtained as 0.0158 for radial mesh and 0.0293 for uniform mesh and maximum strains are obtained as 0.481 for radial mesh and 0.493 for uniform mesh. Figure 5.18 illustrates that forming force requirements for uniform mesh structure are nearly %10 higher than for that of radial

mesh structure. It can be stated that although the same material properties are used in both simulations, using different mesh topologies may influence the stiffness of the deformable body. The radial mesh topology seems to give more reliable results for wrinkling analysis. Also, radial mesh is more suitable to wrinkling analysis.

The simulation results of NUMISHEET 2002 benchmark problem are compared with experimental data given from the participants. Throughout this study, 500 mm/s punch velocity, uniform mesh with 3 mm element size and no mesh refinement are selected as process parameters. Punch force vs. Punch progression graph (Figure 5.20) shows that the simulation results are very close to experimental data, AE-04. The results supplied by other participants are slightly higher (around %15) than this agreement. There is a difference of 20 kN in the measured maximum punch forces between the highest and lowest experimental findings in Figure 5.20. However these differences may exist due to the external influences. For instance, E.H. Atzema (Table A.7) from Corus Research, Development and Technology has stated that the grid applied to blank influenced the friction condition, thus it increased the values in the punch force versus punch displacement graphs by 5 percent. The general trend line for the simulation and experimental findings are in good correlation. The analysis in cylindrical coordinates shows that outer flange contours of the simulation are very close to the experimental findings (Figure 5.21). However the analysis shows that some of the experimental data are not reliable and suitable because they supply low number of data points. Also, the experiment data shows that there is a wide variation in the experimental results. This variation can be related with the quality of the tools used and the precision of the experiment and measurement. The specified lubrication conditions may not be satisfied from the participants so the experiment results show some differences. The misalignment of the blank into the punch die set may be another reason for this unreliable experiment results.

The blank holder simulations are performed for the same geometry of benchmark problem. Blank holder forces from 0 N to 10000 N are simulated. The simulations show that the blank experiences 4 waves in the flange region for zero blank holder force. The blank holder force analysis reveals that as the blank holder force

increases, the wave number increases and the wave amplitude decreases. Table 5.2 illustrates results for 20 mm draw depth from 1 N to 4000 N blank holder forces. Wave amplitude for 1 N blank holder force is around 38.4 mm, and this value decreases to 2.8 mm for 4000 N. This expected behavior continues up to a point where wrinkling of the flange stops. In other words, the amplitude of the waves decreases to zero. The results show that 6875 N blank holder force is required to eliminate wrinkling for isotropic material case. In this study, wave numbers at the flange region starts from 4 and increases up to 24 waves for 6500 N and 6750 N blank holder forces. The punch progression effect on wrinkling (Figure 5.25) also observed. In the free wrinkling case the blank starts wrinkling before 5 mm punch depth and the wrinkling starts around 10 mm for 1000 N blank holder force case. The last case shows that 3000 N force applied to the blank hinders the blank from wrinkling up to 15 mm draw depth. It can be stated that, 7000 N blank holder force avoids wrinkling in flange region for only 40 mm punch progression.

Deep drawing energies for 1000 N, 5000 N and 10000 N blank holder forces (Figure 5.28) equal up to 12 mm punch progression and then the deep drawing energy for the 1000 N BHF case drops. This is the point where the wrinkling energy is smaller than the drawing energy and waves are formed in the flange region. The same event can be observed for the 5000 N BHF at around 25 mm punch progression. These instability points reveal that wrinkling energy is smaller than drawing energy for 1000 N and 5000 N blank holder forces. The material deforms in wrinkling mode, because the blank deforms in a mode that requires least energy in deep drawing processes. However the deep drawing energy for the 10000 N BHF case does not drop or experience instability. This means, the 10000 BHF is able to avoid wrinkling in this particular case. Also, the anisotropy effect on wrinkling is discussed. Although the applied blank holder forces (1000 N) are the same, the anisotropic material experiences 10 waves, whereas the isotropic has 12 waves, refer to Figure 5.29. The flange region for isotropic case experiences 4, 8, 12, 16, 20 and 24 waves for a range of 1 N – 6500 N blank holder forces. The wave numbers are multiples of four and wave amplitudes are same for all waves of isotropic material case.

Drawbead analysis starts with implementing available drawbead models of PAM STAMP. The groove depth is very effective in material flow, refer to Figure 5.33. 2.0 mm and 2.5 mm groove depths result in excessive thinning at the bottom of the cup. Thickness of the blank reduces 20 percent for 2.0 mm groove and 40 percent for 2.5 mm groove. 70 mm, 80 mm and 90 mm radii drawbead locations are used to locate the most effective drawbead position. The drawbead radius of 90 mm is not used after first simulations because the drawbead does not cover the blank as it flows into the die. After comparing wrinkling behaviors (Figure 5.35) for available drawbead locations, the 70 mm radius drawbead model gives better wrinkling prevention and uniform thickness distribution in the flange region. Drawbead module of PAM STAMP is easy to implement, enables fast responses for drawbead geometry changes and is very suitable for pre-design studies of drawbead design.

Physical models of the drawbeads are meshed into the blank holder and die. For 10 kN blank holder forces, both small and large drawbead model experiences wrinkling at the flange region. In order to obtain wrinkle free final product higher blank holder force (100 kN) is applied in the process. The analyses for small and large drawbead models for 100 kN blank holder force show that wrinkling is prevented but, drawbead contour does not enable material flow into the die and behaves like a lock bead (Figure 5.42 and Figure 5.43). The blank thickness contour shows that excessive thinning is experienced in the bottom part of the blank. Minimum thickness is 0.663 mm for small drawbead and 0.641 mm for large drawbead models. Possible tearing may take place for 100 kN blank holder force. In order to improve material flow into the die, inclined model is designed and simulations are performed. The results (refer to Figure 5.45) show that inclined model enables better material flow into the die, which results in less thinning in the blank. The minimum thickness of the blank is improved to 0.79 mm; this indicates %20 improvement in material flow. Wrinkling and necking for blank is prevented for 100 kN blank holder force with inclined drawbead model.

Experimental findings of the conventional deep drawing reveal that the wrinkling is an important problem for thinner blanks. The wrinkling behavior increases as the

thickness of the blank decreases, this is expected. Both experiment and simulation results indicates that, 80 mm diameter blank with 0.5 mm thickness experiences 10 wrinkle waves but no waves are formed for 2.0 mm blank thickness case. 100 mm diameter blank with 0.5 mm thickness experiences 5 - 7 waves in the experiment and the simulation indicates 6 waves for this case. The simulations and experiments show that as the thickness decreases the material is more likely to experience wrinkling. Also, Table 5.9 indicates that blank diameter affects the number of waves formed. As the blank diameter is increased, number of waves formed at the flange region decreases. With 0.5 mm blank thickness; 10 waves are formed for 100 mm diameter blank, 8 waves are formed for 90 mm diameter and 5-7 waves are formed for 100 mm diameter blank. More waves are formed at the flange for the smallest diameter blank (80 mm) case. To conclude, experiment results are in good correlation with the simulation results.

## CHAPTER 7

### CONCLUSION

In this study, the commercial finite element program PAM STAMP is utilized for modeling of plastic wrinkling in deep drawing. Tool geometries and material properties are supplied from NUMISHEET 2002 Benchmark. FE program parameters and their effects on the results are discussed and the optimization study is performed. The parameter effects on accuracy of the results and computational time are compared and the optimum parameters are selected accordingly. FE results are compared with experimental findings (Figure 5.20-5.22) of the benchmark, and the reliability of the dynamic – explicit finite element code is verified.

The effect of blank holder force on wrinkling is inspected for deep drawing quality steel material. Plastic work diagrams for 1000 N, 5000 N and 10000 N blank holder forces are illustrated (Figure 5.28) and wrinkling instability concept is discussed. Moreover, drawbead models are implemented to the problem and results are illustrated. Drawbead effect on wrinkling prevention is discussed. Finally, blank thickness effect on wrinkling is studied both experimentally and numerically. The material properties for 0.5 mm, 1.0 mm, 1.2 mm and 2.0 mm thicknesses of hard aluminum are found by conducting tension tests. Conventional deep drawing experiments for 80 mm, 90 mm and 100 mm diameter blanks of 0.5 mm, 1.0 mm, 1.2 mm and 2.0 mm thicknesses are performed. The experiment data and simulation data are compared and discussed. In conclusion, following general results have been obtained with respect to finite element simulations and experiments:

- Blank holder forces from 0 N to 10000 N are simulated for 1 mm thickness quality steel material. For 0 N blank holder force 4 waves are observed in the flange region (Table 5.2). After performing simulations, it

is found that in order to prevent wrinkling 6875 N blank holder force is required.

- The blank holder force analysis reveals that as the blank holder force increases, the wave number increases and the wave amplitude decreases. Table 5.2 illustrates results for 20 mm draw depth from 1 N to 4000 N blank holder forces. Wave amplitude for 1 N blank holder force is around 38.4 mm, and this value decreases to 2.8 mm for 4000 N.
- In this study, wave numbers at the flange region starts from 4 and increases up to a maximum of 24 waves for 6500 N and 6750 N blank holder forces.
- Deep drawing energies for 1000 N, 5000 N and 10000 N blank holder forces (Figure 5.28) equal up to 12 mm punch progression and then the plastic work for the 1000 N BHF case drops. Plastic wrinkling is observed at the flange region. This instability point reveals that wrinkling energy is smaller than drawing energy.
- Instability point for the 5000 N BHF can be observed at around 25 mm punch progression. Again wrinkling energy is smaller than drawing energy and blank deforms in a mode that requires least energy, as it is also stated by Kaftanoğlu [9].
- It is observed that the energy of wrinkling increases as blank holder force increases. After applying required blank holder force, wrinkling does not occur since it requires a greater energy than drawing. Deep drawing energy trend line is illustrated as 10000 N Blank holder force case in Figure 5.28.
- Drawbead module of PAM STAMP is utilized in pre-designing of drawbead models. Different groove depths and drawbead locations are compared. It is found that FE drawbead module is easy to implement and enables fast responses for drawbead geometry changes.
- Simulations for small and large drawbead models for 10 kN and 100 kN blank holder force reveals that these drawbead models are not suitable for preventing wrinkling and necking (Figure 5.40-5.43).

- In order to improve material flow into the die, inclined model is designed and simulations are performed. The results (refer to Figure 5.45) show that inclined model improves material flow by %20. Wrinkling and necking for blank is prevented for 100 kN blank holder force with inclined drawbead model.
- Experimental findings of the conventional deep drawing reveal that the wrinkling is an important problem for thinner blanks. Both experiment and simulation results indicates that, 80 mm diameter blank with 0.5 mm thickness experiences 10 wrinkle waves but no waves are formed for 2.0 mm blank thickness case (Table 5.9). The simulations and experiments show that as the thickness decreases the material is more likely to experience wrinkling.
- Both experiment and simulation results indicate that, as the blank diameter is increased, number of waves formed at the flange region decreases. With 0.5 mm blank thickness; 10 waves are formed for 100 mm diameter blank, 8 waves are formed for 90 mm diameter and 5-7 waves are formed for 100 mm diameter blank.
- It can be concluded from Table 5.9 that, experiment results are in good correlation with the simulation results.

As a conclusion, this study is expected to be valuable for understanding deep drawing process and plastic wrinkling problem. The simulations performed and the experiments conducted enlighten nearly every aspect in understanding wrinkling and its prevention.

## REFERENCES

1. Johnson W., Mellor P.B., “Engineering Plasticity”, Ellis Horwood Ltd., 1983.
2. Grote K.-H., Antonsson E.K., “Springer Handbook of Mechanical Engineering”, 2008.
3. <http://www.custompartnet.com/wu/sheet-metal-forming>, last accessed; 15<sup>th</sup> August 2010.
4. Metal Forming Handbook, Schuler, Springer-Verlag, Berlin Heidelberg, 1998.
5. M. Colgan, John M.: Deep Drawing Process, Journal of Material Processing Technology, 2003.
6. K. Siegert, S. Wagner, “TALAT Lecture Deep Drawing”, 1994.
7. Serope K., Steven R.S., “Manufacturing Engineering & Technology”, 2006.
8. Banabic, D.; Bunge, H.-J; Pöhlandt, K.; Tekkaya, A. E.: Formability of Metallic Materials, Springer-Verlag: Berlin/Heidelberg/New York/Tokyo, 2000.
9. Kaftanoğlu B., “Plastic Analysis of Flange Wrinkling in Axisymmetrical Deep Drawing”. Proceedings of the 21<sup>st</sup> International Machine Tool Design and Research Conference, 1980, pp.21–28.
10. Ramaekers J.A.H, de Winter A., Kessels M.W.H., “Deepdrawability of a Round Cylindrical Cup”, IDDRG’94, 1994, pp.403–412.

11. Cao J., Boyce M.C., “A Predictive Tool for Delaying Wrinkling and Tearing Failures in Sheet Metal Forming”, Transactions of the ASME, Vol.119, October 1997, pp.354–365.
12. Cao J.,”Prediction of Plastic Wrinkling Using the Energy Method”, Journal of Applied Mechanics, Vol.66, September 1999, pp.646–652.
13. Alves J.L., Oliveira M.C., Menezes L.F., “Study of the Influence of the Refinement of a 3–D Finite Element Mesh in Draw–In Ears and Wrinkles of a Deep Drawn Cylindrical Cup”, Proceedings of the 5<sup>th</sup> International Conference and Workshop on Numerical Simulation of 3D Sheet Forming Processes, Vol.1, 2002, pp.301–306.
14. Nakamura Y., Ohata T., Nakamachi E., Katayama T., Ueda T., “Study of Optimum Drawbead Design in Sheet Metal Forming”, Proceedings of the 5<sup>th</sup> International Conference and Workshop on Numerical Simulation of 3D Sheet Forming Processes, Vol.1, 2002, pp.585–590.
15. Zeng X.M., Mahdavian S.M., “Critical Conditions of Wrinkling in Deep Drawing at Elevated Temperature”, Journal of Materials Processing Technology, Vol.84, 1998, pp.38–46.
16. Önder İ.E., “Assessment of sheet metal forming processes by numerical experiments”, Ph.D Thesis, Middle East Technical University, Mechanical Engineering Department, Ankara, May 2005.
17. Sönmez Ç., “Investigation of the deep drawability of steel and aluminum sheets by finite element simulation”, Ph.D Thesis, Middle East Technical University, Mechanical Engineering Department, Ankara, April 2005.

18. A. E. Tekkaya: Finite Element Analysis in Solid Mechanics, Lecture Notes, Middle East Technical University, Ankara, 2002
19. K. Schewizerhof, J.O. Hallquist: Explicit Integration Scheme and Contact Formulation for Thin Sheet Metal Forming In: FE-Simulation of 3D sheet metal forming processes in automotive industry. VDI-Ber. 894 (1991), 405 – 439.
20. PAM-STAMP 2G Reference Manual, ESI-Software, France, October, 2002.
21. PAM-STAMP 2G User's Guide, ESI-Software, France, October, 2002.
22. NUMISHEET 2002 Benchmark A: Deep Drawing of Cylindrical Cup, NUMISHEET 2002, Proceedings of the Fifth International Conference and Workshop on Numerical Simulation of 3D Sheet Forming Processes, Jeju Island, Korea, October 21-25, 2002.

## APPENDIX A

### NUNMISHEET 2002 BENCHMARK PARTICIPANTS

**Table A.1 Participant information of AE-01**

<b>Experiment</b>	AE-01
<b>Benchmark participant:</b>	Haruyuki Konishi (Kobe Steel), Robert E Dick(ALCOA)
<b>Address:</b>	5-5 Takatsukadai 1, Nishi-ku, Kobe, 651-2271 JAPAN
<b>Email:</b>	konishi@afrs.kobelco.co.jp, Robert.Dick@alcoa.com
<b>Phone Number:</b>	81-78-992-5515
<b>Fax Number:</b>	81-78-992-5517

**Table A.2 Participant information of AE-02**

<b>Experiment</b>	AE-02
<b>Benchmark participant:</b>	No data is provided for this participant and benchmark experiment
<b>Address:</b>	
<b>Email:</b>	
<b>Phone Number:</b>	
<b>Fax Number:</b>	

**Table A.3 Participant information of AE-03**

<b>Experiment</b>	AE-03
<b>Benchmark participant:</b>	L. Filice
<b>Affiliation:</b>	University of Calabria
<b>Address:</b>	Dep. of Mech. Eng. , 87036 RENDE (CS) - Italy
<b>Email:</b>	l.filice@unical.it
<b>Phone Number:</b>	+39 0984 494608
<b>Fax Number:</b>	+39 0984 494673

**Table A.4 Participant information of AE-04**

<b>Experiment</b>	AE-04
<b>Benchmark participant:</b>	Joachim Danckert
<b>Affiliation:</b>	Department of Production, Aalborg University
<b>Address:</b>	Fibigerstraede 16, DK-9220 Aalborg, Denmark
<b>Email:</b>	i9joach@iprod.auc.dk
<b>Phone number:</b>	45 9635 8959
<b>Fax number:</b>	45 98 15 30 30

**Table A.5 Participant information of AE-05**

<b>Experiment</b>	AE-05
<b>Benchmark participant:</b>	P.P. Date, Amit. M. Joshi, V. Anil Kumar. Sammeta
<b>Affiliation:</b>	Indian Institute of Technology, Bombay
<b>Address:</b>	Mech. Eng. Dept. IIT. Bombay, Powai, Mumbai- India
<b>Email:</b>	ppdate@me.iitb.ac.in, amitmechindia@yahoo.com
<b>Phone number:</b>	91 22 576 7511
<b>Fax number:</b>	91 22 572 6875

**Table A.6 Participant information of AE-06**

<b>Experiment</b>	AE-06
<b>Benchmark participant:</b>	Jonathan White*, Seung-Geun Lee*, Y.Choi*, J.K.Lee*, R.H. Wagoner**
<b>Affiliation:</b>	The Ohio State University, *Dept. Mech. Eng., **Dept. Mat. Sci. and Eng.
<b>Address:</b>	*209 West 18th Avenue. Columbus Ohio 43210 **2041 College Drive, Columbus Ohio 43210
<b>Email:</b>	choi.43@osu.edu, Lee.71@osu.edu
<b>Phone number:</b>	(614)292-7371
<b>Fax number:</b>	(614)292-7369
<b>Remarks:</b>	All measurements are numerical averaged values of three experiments

**Table A.7 Participant information of AE-07**

<b>Experiment</b>	AE-07
<b>Benchmark participant:</b>	E.H. Atzema
<b>Affiliation:</b>	Corus Research, development & Technology
<b>Address:</b>	IJTC-PRA-AUT-STP
<b>Email:</b>	3H36 / 1-18; P.O. Box 10.000; 1970 CA IJmuiden; Netherlands
<b>Phone number:</b>	+31 2514 98524'
<b>Fax number:</b>	+31 2514 70432'
<b>Remarks:</b>	Thickness was obtained from optical surface strain measurements (PHAST tm) on the outside surface of the cup. This means the strains will be over estimated and consequently the thickness underestimated at the punch radius. The other way around at the die radius. Moreover the grid applied may influence the friction. On the aluminum the grid showed no influence on force displacement diagram, on steel a 5% increase in force was seen.

## APPENDIX B

### TINIUS OLSEN TESTING MACHINE

**Table B.1 Specifications of Tinius Olsen A-40 Testing Machine**

<b>Model</b>	<b>A-40</b>
Maximum Capacity	70000 Ibs.
Low Range Capacity	30000 Ibs.
Maximum Diameter Cup	75 mm
Clamping Pressure	0-20000 Ibs.
Testing Speed	0-12 inch/min
Stroke	0-3 inch
Motor Horsepower	3
Width	28 inch
Depth	27 inch
Height	72 inch
Net Weight	1480 Ibs.
Gross Weight	1820 Ibs.